PNC TN8410 94−194

公開資料

核燃料技術開発部紀要

−第3号−

1994年5月

動力炉・核燃料開発事業団
東海事業所

複製又はこの資料の入手については、下記にお問い合わせ下さい。
〒319-11　茨城県那珂郡東海村大字村松４－33
動力炉・核燃料開発事業団　東海事業所
技術開発推進部　技術管理室

Inquiries about copyright and reproduction should be addressed to:
Technology Management Section, Tokai Works, Power Reactor and Nuclear Fuel Development Corporation 4-33, Muramatsu, Tokai-mura, Naka-gun, Ibaraki, 319-11, Japan)

公　開　資　料
PNC TN8410 94－194
1994年　5月

核燃料技術開発部紀要

－第3号－

高橋　武士*　他

要　旨

本報告書は、1992年度、1993年度に核燃料技術開発部で実施した研究開発の中で、ある程度のまとまりをみたテーマに関する論文集であり、核燃料，レーザ，材料等の広い分野にわたる研究開発が述べられている。

なお、各々のテーマについては、それぞれ単独の報告書が作成されているが、ここにそれらをダイジェスト版的にまとめたものである。

---

*核燃料技術開発部長

目　次

まえがき

ま え が き

核燃料技術開発部は、動燃事業団がこれまでに培ってきた技術の更なる高度化に向けた技術開発に加え、新しい原子力技術を創出し得る基礎基盤技術、および革新的技術の開発を目的として、平成元年に設立されてから、５年余りが経過しました。

この間、旧ソ連の崩壊が起こり、これを契機として世界情勢は急速な変化を続けております。このような国際状況にあって、原子力を取り巻く環境も大きな影響を受けております。米国においては、様々な危険物質や放射性物質によって汚染された軍需関連施設およびその周辺の環境回復に、多大な資金および労力の投入が、長期に渡って必要とされています。一方、ロシアにおいても同様の問題が顕在化してきています。さらに、米国およびロシアの保有する核兵器の解体により回収される高濃縮ウランおよびプルトニウムの処理が、これら二ヵ国のみならず国際的な課題となっています。このような原子力を取り巻く諸般の事情により、多くの国において原子力開発の停滞が余儀無くされています。

我が国は、幸いにも、平和利用に限り原子力開発を行ってきたために、比較的順調に進展してきましたが、今後を考えると、その影響は小さいとは言えません。したがって、更なる原子力の発展には、今後とも徹底した“平和利用のための原子燃料サイクル”を目指すことが必要でしょう。なお、米露を始め他の核保有国においても、原子力の利用は、軍需から民需へ大きく転換して行くものと思われます。この過程において、民需に限った開発を進めてきた、我が国の果たすべき役割は非常に大きいものになるでしょう。

さて、原子燃料サイクルの常なる目標は、核燃料資源であるウランの有効利用にあります。しかし、核燃料は、化石燃料とは異なり、その利用には高度の利用技術が必要となります。今年４月５日に初臨界を達成した高速増殖原型炉「もんじゅ」は、ウラン資源利用の高度化としてのプルトニウムの利用技術を達成するものに他なりません。これにより、ウラン２３５のみを利用した場合に比べ６０～１００倍程度利用効率を向上させることが可能となりますが、燃料サイクル全体を見れば、まだ多くの技術開発課題があり、継続した技術開発が必要です。

また、現在検討が進められているアクチニド・リサイクルは、更なるウランの資源利用の向上を目指すと同時に環境負荷の低減や核拡散抵抗性の向上等、これからの社会のニーズにも応えるものと言えます。しかし、社会のニーズは、不変ではなく時代とともに変わっていきます。したがって、その変化に充分対応をしていくためには、柔軟性のある技術が必要となります。このためには、基礎基盤技術の充実が不可欠です。

今後とも、核燃料技術開発部は、核燃料サイクル技術の更なる高度化とともに、核燃料資源の利用効率の向上を目指して、着実に技術開発を進めてまいります。本紀要も、これが３報目です。この紀要の歩みが、原子力の発展に寄与することを期待します。

１９９４年　５月
核燃料技術開発部長
高橋　武士

1. 『もんじゅ』初装荷炉心燃料の製造技術開発 (※)

―脱脂・焼結雰囲気のペレット中不純物に及ぼす影響―

森平正之*，遠藤秀男*，成田大祐*，上村勝一郎*
山口俊弘**，長井修一朗***，羽成章****，吉田真之****
*プルトニウム燃料開発室　Plutonium Fuel Technology Development Section
**現プルトニウム燃料工場製造課　Pellet Fabrication Section
***現大洗工学センタ燃料材料技術開発部　Fuels and Materials Division, O-arai Engineering Center
****検査開発㈱　Inspection Development Co.,Ltd.

The Effect of Dewaxing and Sintering Atomosphere on Carbon and Nitrogen Contents of Low Density MOX Fuel Pellets for "MONJU"

M.Morihira*, H.Endo*, D.Narita*, K.Kamimura*, T.Yamaguchi**,
S.Nagai***, A.Hanari****, M.Yoshida****

The Effect of dewaxing and sintering atmosphere on carbon and nitrogen contents of low density MOX fuel pellets for "MONJU" was invesitigated. The pellets contained a large amount of nitrogen impurity by sintering under $N_2-5\%H_2$ gas flow, but such a phenomenon was not observed under $Ar-5\%H_2$ atmosphere.

Pellets which contained the lowest amount of carbon and nitrogen impurities could be obtained by dewaxing under CO_2gas flow. It was therefore presumed that the nitrogen impurity exists as nitride in pellets and the cause of nitrogen increase under $N_2-5\%H_2$ sintering atomosphere is the occourrence of carbothermic reduction among MOX, residual carbon and N_2 in sintering atmosphere.

1. 緒　言

プルトニウム燃料工場における「もんじゅ」初装荷燃料製造を技術的に支援することを目的として、核燃料技術開発部で燃料ペレット製造試験を行った。本報告は、ペレット焼成工程における脱ガス回数の低減化を目的とした試験に関するものである。

ペレットの焼成工程は、脱脂，焼結，真空熱処理の3段階から構成される。このうち脱脂は粉末成形時に添加した有機物の熱分解除去を、真空熱処理は焼結ペレット中の蒸発性不純物の除去を目的として行う。

動燃事業団では、従来より、ペレット焼成時の雰囲気ガスとして$N_2-5\%H_2$ガスを使用してきたが、このガスを低密度ペレットの焼成に使用した場合、図1に示すように脱脂から焼結に際して、炭素及び窒素の不純物量が特徴的に変化する。即ち、脱脂ペレットに4000ppm前後含まれる炭素不純物が焼結によって数10ppm以下に低減するのに対し、窒素不純物は、逆に脱脂ペレット中の200ppm程度から3000ppm前後まで増加している。

そこで、ペレット中の窒素不純物に関する予備的な試験，検討を行ったところ、次のことがわかった。

(1) 窒素不純物量の多い焼結ペレットの金相には白斑の存在が観察され、この白斑をEPMAで定性分析したところ、U，Puと共にN，Cの存在が認められたことから、N，CがU，Puと化合している可能性があること。

(2) 焼結ペレット中の吸着窒素は2500℃の真空加熱によって抽出することができるが、今回、同じ試料に助燃剤を加えて更に2700～2800℃まで加熱したところ、新たに窒素が検出された。即ち、このペレットは、吸着窒素以外の化学的に結合した窒素を含んでいると考えられ、その化合物は、遊離温度から考えて窒化物である可能性があること。

これらの点から、焼結ペレット中の窒素が窒化物状態で存在していることが予想され、それは脱脂・焼結雰囲気と関係していることが考えられた。

そこで、脱脂・焼結雰囲気がペレット中の不純物、特に炭素と窒素量に及ぼす影響について試験を行った。

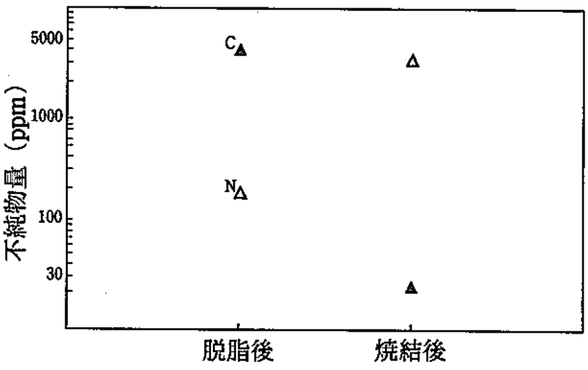

※脱脂・焼結雰囲気：$N_2-5\%H_2$

図1　焼成工程における窒素及び炭素不純物量の変化

2. 試験方法

(1) 試験ペレット調整

試験ペレットの原料粉末には、マイクロ波直接脱硝法によるMOX粉末（Pu:U=1:1）とADU法によって得られたUO_2（劣化ウラン）粉末を使用した。これらの粉末をPu富化度が約20wt%になるように秤量した後、ボールミルで4時間混合した。得られた均一化混合粉には、造粒前にバインダとして0.5wt%のステアリン酸亜鉛を、造粒後に約2.0wt%のグリセリン系ポアフォーマと、ルブリカントとしての0.2wt%のステアリン酸亜鉛を添化した。ペレットの成形圧は3～4ton/cm²に設定した。試験ペレットの調整条件を図2に示す。

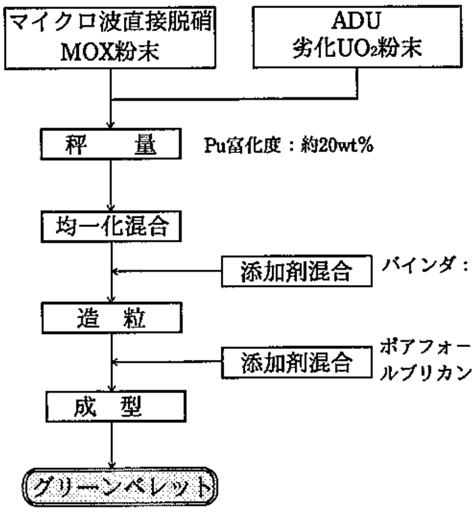

図２　試験ペレット調製条件

(2) 焼成条件

脱脂雰囲気には、$N_2-5\%H_2$, CO_2, $Ar-5\%H_2$の3種類を用いた。脱脂温度は900℃×2時間としたが、CO_2については、モリブデン製焼結皿の酸化による蒸発損失を抑える目的から800℃×2時間に設定した。脱脂ガス流量はいずれも1 ℓ/分とした。

焼結は1650℃×2時間としたが、$N_2-5\%H_2$で脱脂したペレットは焼結も$N_2-5\%H_2$で、$Ar-5\%H_2$及びCO_2脱脂ペレットは$Ar-5\%H_2$で焼結した。焼結ガス流量はいずれも5 ℓ/分とした。脱脂及び焼結条件を表1に示す。

表１　試験パラメータ

No.	脱脂条件		焼結条件	
	雰囲気	温度×時間	雰囲気	温度×時間
①	$N_2-5\%H_2$	900℃×2hr	$N_2-5\%H_2$	1650℃×2hr
②	CO_2	800℃×2hr	$Ar-5\%H_2$	
③	$Ar-5\%H_2$	900℃×2hr	$Ar-5\%H_2$	

3. 試験結果

$N_2-5\%H_2$で脱脂した場合と$Ar-5\%H_2$の場合とでは、脱脂ペレット中の不純物量はN=170～190ppm, C=3800～4100ppmと同程度であった。これに対し、焼結ペレットは、N=3300ppm（$N_2-5\%H_2$で脱脂・焼結）、N=240ppm（$Ar-5\%H_2$で脱脂・焼結）と、$Ar-5\%H_2$で焼結した方が窒素不純物量が減少した。炭素不純物については双方とも、30ppm未満であった。（図3参照）

また、CO_2脱脂後の炭素量は70ppmであり、焼結ペレット中の窒素量は50ppm未満となった。（図4参照）

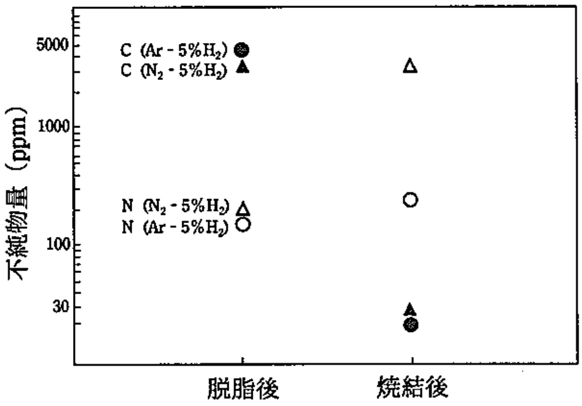

図３　Ar—5%H_2　脱脂・焼結の結果

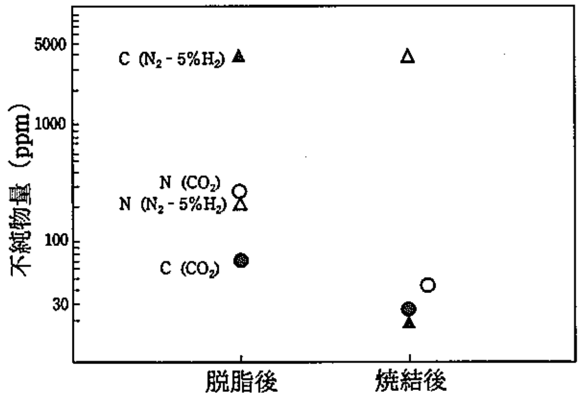

図４　CO_2脱脂・Ar—5%H_2焼結の結果

4. 考　察

試験結果を整理すると次のようになる。

脱脂 ($N_2-5\%H_2$) ┐
　　　　　　　　　 ├→ 脱脂ペレット中の炭素不純物，窒素不純物量は同程度
脱脂 ($Ar-5\%H_2$) ┘
脱脂 (CO_2) → 脱脂ペレット中の炭素不純物は少，窒素不純物量は$N_2-5\%H_2$，$Ar-5\%H_2$と同程度

①脱脂ペレット中の不純物量
②焼結ペレット中の不純物量
脱脂･焼結 (N_2−5%H_2)→焼結ペレット中の窒素不純物量は大
脱脂･焼結 (Ar−5%H_2)→焼結ペレット中の窒素不純物量は少
脱脂 (CO_2)･焼結 (Ar_2−5%H_2)→焼結ペレット中の窒素不純物量は少

すなわち、N_2−5%H_2もAr−5%H_2も脱脂段階では窒素・炭素不純物量にほとんど影響しないが、焼結することによってその差が現れる。これに対しCO_2は脱脂時の脱炭効果が高く、その脱脂ペレットをAr−5%H_2で焼結して得た焼結ペレットもまた窒素不純物量が少ないものであった。これらの点から、以下の考察を行った。

高密度ペレットと比べて低密度ペレット中の炭素・窒素不純物量が増加する原因として、ポアフォーマを添加することにより有機物量が多くなることが考えられる。バインダ、ポアフォーマ等の有機物を熱分解・除去するために脱脂を行うが、これらの有機物の添加量が増加すると、その残渣が炭素として脱脂ペレット中に残留すると考えられる。このような炭素を含むMOXペレットを焼結工程において、窒素雰囲気中の1650℃という高温で加熱することにより、ペレット内で炭素熱還元反応が生じ窒化物が生成しているのではないかと考えられる。窒化物は酸化物に炭素を添加して窒素雰囲気中で1300～1400℃以上に加熱すると次式により生成することが知られている(1)。

$$(U, Pu)\,O_2 + 2C + 1/2N_2 \rightarrow (U, Pu)\,N + 2CO$$

前述した窒素分析における特徴についても、助燃剤なしの2500℃以下で抽出できる窒素が吸着窒素もしくはU_2N_3の熱分解（1350℃以上でUNに分解する。）に伴う窒素であり、助燃剤を加えて2700～2800℃まで加熱した場合に遊離する窒素が窒化物窒素であるとすれば説明できる。

他方、窒素不純物量の多い焼結ペレットであっても、真空熱処理を繰り返すことによって窒素不純物量が減少することが経験的に知られている。これは、真空中といえども若干の酸素ポテンシアルがあり、焼結中に生成した窒化物が酸化されるためと考えられる。窒化物のペレットは空気中で400～450℃以上に加熱すると酸化する(2)ので、800～900℃の真空熱処理によって十分に酸化され得る。

Ar−5%H_2で脱脂・焼結を行った場合、脱脂ペレットに多量の炭素が含まれていても焼結ペレット中の窒素不純物量は低減されたことは、焼結雰囲気が窒素フリーであるため、炭素熱還元反応よる窒化物生成を抑制することができるためと考えられる。

CO_2脱脂の際の脱炭は、

$$CO_2 + C \rightarrow 2CO$$

の反応によって生じると考えられる。本試験ではCO_2脱脂後の焼結雰囲気としてAr−5%H_2を使用したが、脱脂ペレット中の炭素量が十分少ないため、仮にN_2−5%H_2中で焼結したとしても、窒素不純物量が増加することはないと予想される。

5. 結　論

(1) 窒素フリーであるAr−5%H_2雰囲気下における焼結は、N_2−5%H_2の場合に比べて焼結ペレット中の窒素不純物量低減に有効である。
(2) 低密度ペレット製造における焼結ペレット中の窒素不純物が、脱脂ペレット中の炭素不純物と焼結雰囲気中の窒素による炭素熱還元が原因であるとすると、結果が説明できる。
(3) 脱脂ペレット中の炭素不純物量低減には、800℃のCO_2脱脂がより有効である。

6. 参考文献

(※) 森平正之，遠藤秀男，他：“「もんじゅ」初装荷燃料の製造技術開発（Ⅲ）一脱脂・焼結雰囲気のペレット中不純物に及ぼす影響一”，日本原子力学会1993年春の年会K23 (1993).
(1) C. Ganguly et al.: J. Nucl. Mater.,178,234 (1991).
(2) K. Richter et al.; Transaction ANS (1979).

2. 酸化破砕による乾式回収試験（Ｉ）

川瀬啓一*，遠藤秀男*，山本純太*，上村勝一郎*，羽成章**，　吉田真之**
*プルトニウム燃料開発室　Plutonium Fuel Technology Development Section
**検査開発㈱　Inspection Development Co.,Ltd.

Experiment on Dry Recovery of MOX Fuel Pellets Using Phase Transformation by Oxidation（Ｉ）

K.Kawase*, H.Endo*, J.Yamamoto*, K.Kamimura*, A.Hanari**, M.Yoshida**

Pellets of uranium-plutonium mixed oxide with Pu/(Pu+U) ratios with 0.22 have been oxidized in an sir atmosphere at temperatures between 300℃ and 1000℃ for 3hr. The disintegration of pellet took place at 500℃. The result of X-ray diffraction analysis of disintegrated pellet showed two phases. These are M_3O_{8-Z} (orthorhombic) phase and the MO_{2+X} (f.c.c) phase.

Ceramographic and X-ray diffraction analysis were performed with pellets which did not disintegrate. From the results of X-ray diffraction analyses, two phases could be found with pellets which were oxidixed at temperature of 500℃, 600℃ and 1000℃ as well. The results of ceramographic analyses revealed the difference of phase separation behavior by oxidation temperature. From microstructure of two phases at 600℃, it was difficult to point out M_3O_{8-Z} phase. On the otherhand microstructure of two phase at 1000℃ showed that M_3O_{8-Z}phase segregated at the grain boundaries of the MO_{2+X} matrix.

It was therefore presumed that the disintegration of pellet took place by precipitation of M_3O_{8-Z} phase in MO_{2+X} matrix without diffusion of Pu and U at 500℃.

1. 概　要

FBR用混合酸化物燃料（以下MOX燃料と呼ぶ）製造において、焼結したペレットのうち、密度，外観等の検査において仕様を満たしていないペレットは、製品としての使用ができないためにスクラップとして回収され、核燃料物質の再利用のために処理される。この再利用のためのスクラップ処理法としては、大きく分類して乾式法と湿式法の二つの方法がある。湿式法は、ペレットを硝酸等で溶解させて溶液としてから処理を行うために作業員の被ばくを抑えるために設備が大がかりになること、また、溶液から粉末にするための工程等が必要になり工程が複雑になる等の問題点がある。一方乾式法では、酸化による相変化を利用する方法と機械的な手法（ハンマー・ミル，ジェット・ミル等）を利用する方法、及びこれらを組み合わせて行う、の3つの方法が考えられる。乾式法の中でも、酸化による破砕法は、酸化を行って結晶構造を変化させ、それによって生じる結晶系の歪によって破砕がおこることを利用している。このため①大量のペレットを処理できる、②操作が簡単であるため工程が単純であり、かつ被ばくを少なくできる、③不純物の混入が少ない等の長所がありスクラップ・ペレットの回収方法としては最も有効な手段と考えられる。

これまで、動燃事業団でも「常陽」燃料製造で酸化破砕による乾式回収が行われ、実績を積んでいる。これまでの経験から、酸化破砕による乾式回収のための最適条件は概ね把握していたが、「もんじゅ」燃料製造に当たり再確認を行うことを目的として、「もんじゅ」内側炉心燃料ペレット（Pu富化度約22%）を用いて試験を行った。また、合わせて今回の試験で得られたデータを基に酸化破砕のメカニズムについても一部評価を行った。

2. 試験内容

本試験では、プルトニウム燃料工場において製造された「もんじゅ」内側炉心燃料ペレット（以下単にペレットと呼ぶ）を試験試料として用いた。使用したペレットの製造履歴を表2に示す。

表２　試験に使用したペレットの製造履歴

ロットNo.	L1C104
Pu富化度	21.5wt%
乾式回収紛添加率	40wt%
ポアフォーマ添加率	1.7wt%
焼結条件	1680℃　2時間 Ar−5%H_2　雰囲気
焼結密度	83.48（σ=0.78）%TD
再焼結温度・時間	1685℃　1時間
再焼結後密度	83.94（σ=0.77）%TD

試験は管状電気炉を用い、空気中で300, 400, 500, 600, 700, 800, 1000℃の各設定温度においてペレットを酸化させた。使用した管状電気炉の概略を図2に示す。

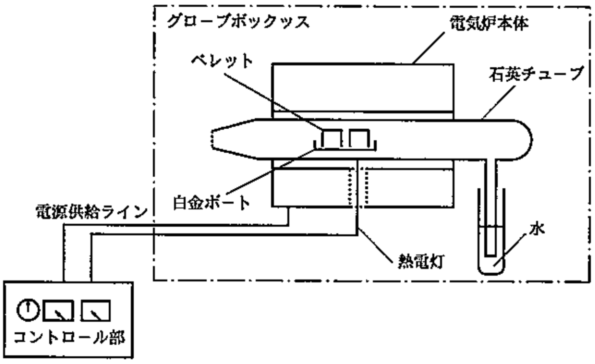

図2　試験装置概略図

ペレットは、予め所定の温度にまで加熱された炉内（石英ガラス管中）に白金ボードにのせて挿入され、3時間の酸化を行う。酸化終了後は、白金ボードを炉より取り出し、空気中で室温まで冷却した。

酸化後のペレットは、炉から取り出した時に破砕が生じているかどうかの外観観察を行った後、金相観察，X線回折装置による分析を行い、結晶構造の変化，格子定数の測定を行った。また、ペレットの酸化前後の重量変化を測定し、次式を用いて酸化後の酸素／金属比（O／M値）の簡便な方法での分析を行った。

$$\text{酸化後O/M値}=\text{酸化前O/M値}+\frac{\text{M}}{16}\times\frac{\Delta\text{W}}{100}$$

M　：平均分子量
ΔW　：重量変化率（%）

3.　試験結果

各温度でのペレット酸化試験を実施した後、外観観察を行った。その結果、500℃で酸化されたペレットにおいて破砕が生じていた。その他の酸化温度のペレットでは、外観上の変化は見られなかった。図3−1に酸化前のペレットの、図3−2に酸化によって破砕の生じた500℃のペレットと破砕の生じなかった1000℃のペレットの外観写真を示す。また、酸化前後のペレットの重量変化から求めた酸化後のO／M値を表3に示す。酸化破砕の生じた500℃のペレットについては、正確な重量変化は求められなかったが、試験前のO／M値1.99から最終的なO／M値は2.5程度まで上昇していた。600, 1000℃で酸化したペレットでは、最終的なO／M値は2.4程度、それ以外のペレットでは2.3程度であり、600, 1000℃で酸化したペレットが破砕の生じていなかったペレットの中では比較的酸化が進行していた。

次に、図3−3酸化試験前後の金相写真（エッチング後）を示す。酸化後の写真については、破砕の生じたペレットの金相観察は行えなかったため比較的酸化の進行していた酸化温度600, 1000℃の写真を示す。酸化温度600℃の写真では、結晶粒界が非常に不明瞭となっており、エッチング効果の異なる別の相が析出していた。また、1000℃で酸化したペレットでは、酸化前に比べ粒界が明瞭になっていた⑴。

さらに、図3−4に酸化試験後ペレットのX線回析データを示す。X線回析データでは500℃, 1000℃で酸化したペレットにおいてMO$_{2+x}$相の他に、M$_3$O$_{8-z}$（斜方晶）相によると考えられる明瞭なピークが観察された。また、600℃, 800℃においても非常に小さいがM$_3$O$_{8-z}$（斜方晶）相によると推定されるピークが確認された。また、酸化温度700℃のペレットではMO$_{2+X}$（面心立方晶）相のほかに、M$_3$O$_7$（正方晶）と考えられるピークがX線回析データで確認された［MO$_{2+x}$の（200）面、（311）面の回析ピークの近傍にピークが認められ、これがM$_3$O$_7$(正方晶）相によるものである］。

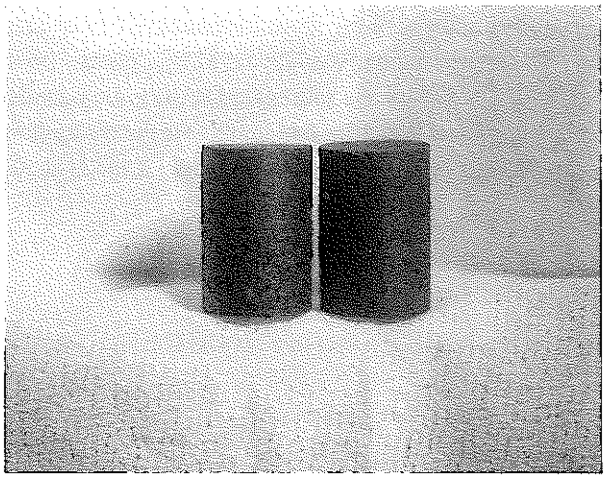

図3−1　外観写真（酸化前）

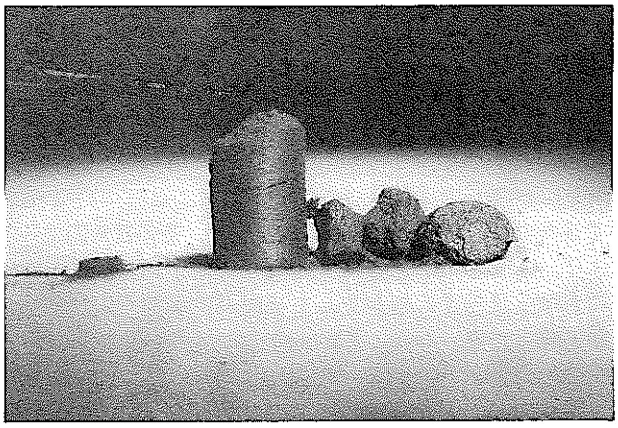

500℃3時間酸化後

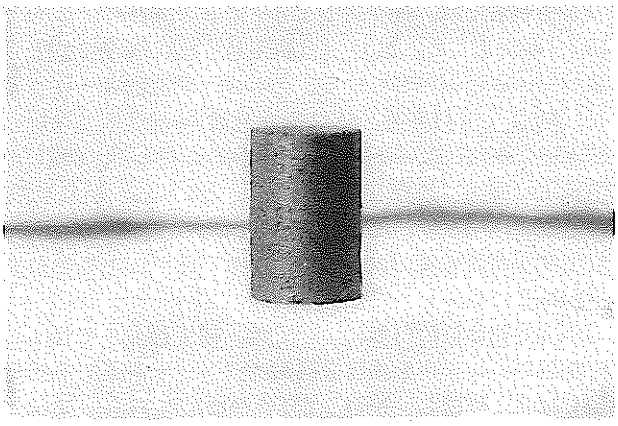

1000℃3時間酸化後

図３－２　外観写真（酸化後）

表３　酸化試験前後のO／M値

	O／M値
酸化前	1.99
300℃	2.33
400℃	2.35
500℃	2.49
600℃	2.39
700℃	2.33
800℃	2.34
1000℃	2.39

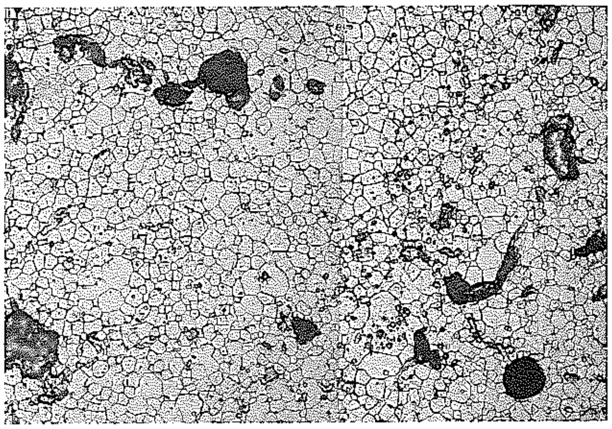

1000℃3時間酸化後

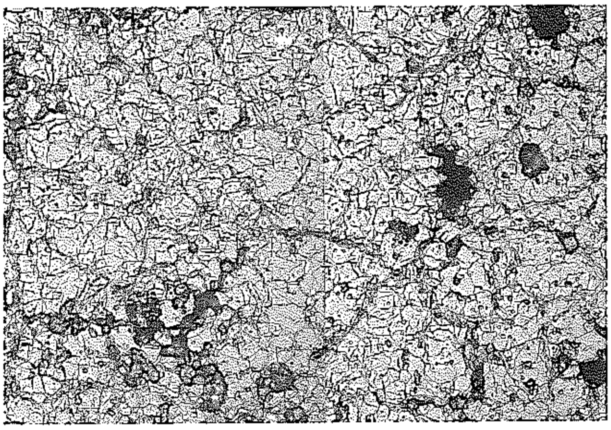

600℃3時間酸化後

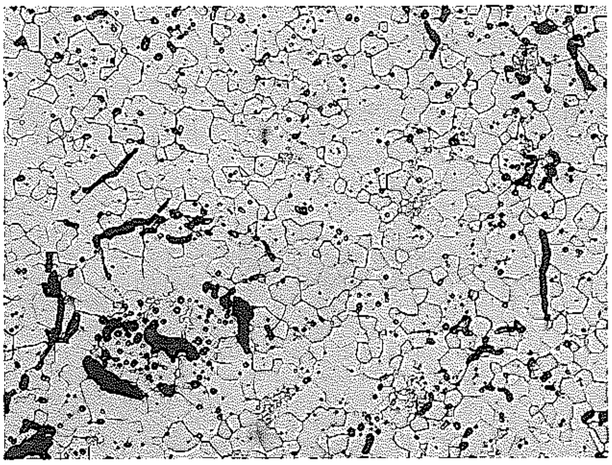

酸化前

図３－３　金相写真（エッチング後）

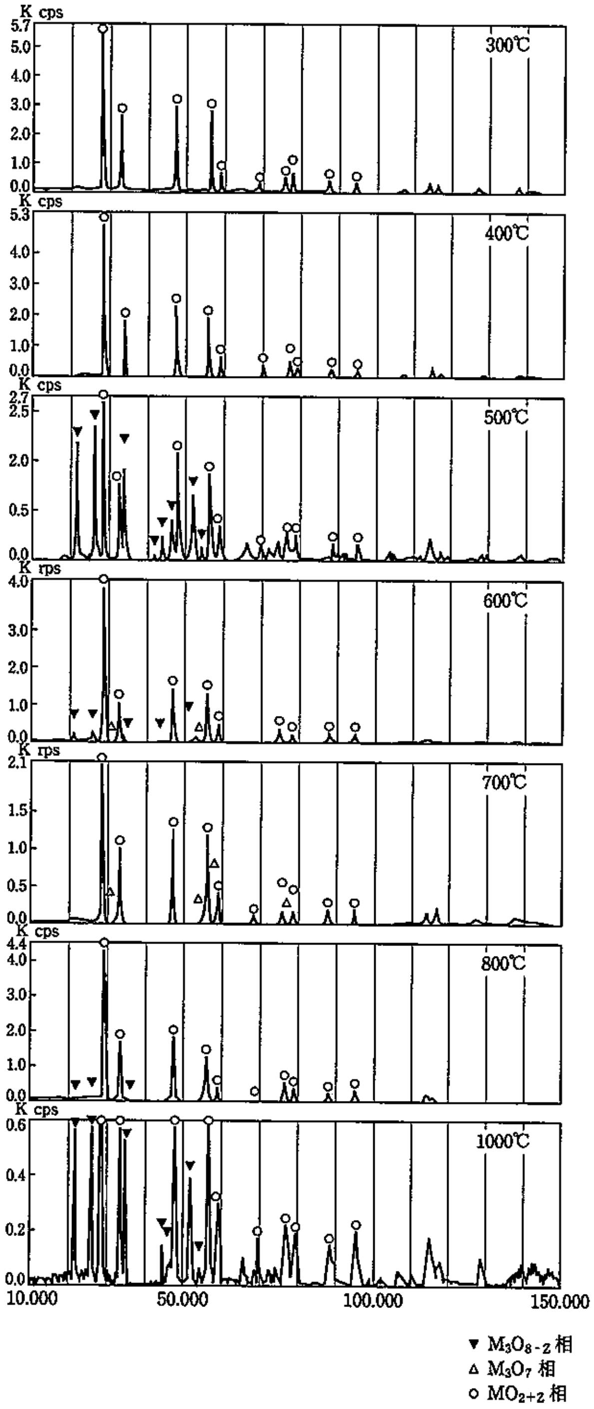

図３－４　X線回析データ（酸化後）

4. 考察

今回の試験において、X線回析データにおいて明らかにM_3O_{8-Z}（斜方晶）相が観察された酸化温度が500℃, 1000℃の試料のうち、酸化温度が500℃において破砕が生じ、1000℃では破砕が生じなかったことについて考察するために、Sariらの研究を紹介する。その研究論文(2),(3)より、U-Pu-O系の3元系状態図を図4に示す。なお、室温における状態図はサンプルを高温（900℃）下で20時間熱処理した後、室温にまで徐冷して作成された。また、600℃, 1000℃の状態図は、サンプルをそれぞれの温度で熱処理した後にクエンチング（急冷）して作成された。研究論文(2)によると、室温及び1000℃の状態図で観察されるM_3O_{8-Z}（斜方晶）相とMO_{2+X}（面心立方晶）相の二相領域では、PuイオンとUイオンの移動によるPuとUの分離が生じて、M_3O_{8-Z}（斜方晶）相のPu濃度が低くなっていると報告している。それは、研究論文(1)によると、M_3O_{8-Z}（斜方晶）相はPu富化度8wt%以下でなければ安定に存在しないためである。それに対して、600℃の準安定状態図で観察されるM_3O_{8-Z}（斜方晶）相とM_3O_7（正方晶）相との二相領域では、PuとUが分離せず、Pu富化度が高富化度（20wt%）のままで析出したものと述べられている。

PuとUの分離の有無については、研究論文(2)では、二相混在のサンプルを適当な酸素ポテンシャル下で熱処理して$MO_{2.00}$に戻し、$MO_{2.00}$が1つの面心立方晶か又は、$M'O_{2.00}+M''O_{2.00}$の2つの面心立方晶で構成されるかを確認することによって判断している。すなわち、600℃は温度が低く、PuとUの移動は生じないため、安定には存在しないM_3O_{8-Z}（斜方晶）相が析出する。逆に、1000℃ではPuとUの移動が起こるには十分な温度であるために安定なM_3O_{8-Z}（斜方晶）相が析出する。

ここで、本試験結果について考えると、酸化温度が500℃ではPuの移動が起こるには十分な温度ではなく、今回の試験で用いたPu富化度が21.5wt%のペレットでは本来ならば安定に存在しないM_3O_{8-Z}相が析出したものと考えられる。本試験では、管状炉中での酸化時間（3時間）が経過すると炉からすぐに取り出して空冷しているために、500℃で析出したM_3O_{8-Z}相が保持され観察されたと考えられる。一方、M_3O_{8-Z}相が析出しても破砕が起こらなかった1000℃では、Puの移動が起こるには十分な温度でPuが結晶粒界から粒内に移動し、結晶粒界で部分的にPu富化度8wt%以下になるために安定なM_3O_{8-Z}相が均一に析出したものと考えられる。このことは、金相観察において酸化後の粒界が明瞭になっていたことが、粒界部分にエッチング効果の異なる別の相、つまりM_3O_{8-Z}相が析出したこととも一致する(1)。

すなわち、1000℃ではPuの移動を伴って結晶粒界にM_3O_{8-Z}相が析出し、結晶格子に歪みを生じないでMO_{2+X}相との2相混合状態となったと考えられる。逆に、酸化温度が500℃ではPuの移動がほとんど起こらないため、結

晶粒内において局所的にM_3O_{8-Z}相が析出することによってMO_{2+X}相との境界で歪みが生じ、これが原因で破砕が生じたと考えられる。600℃，800℃においてM_3O_{8-Z}相が確認されているが、X線回折データでは非常にピークが小さいことから、破砕に至るほどの量が析出しなかったものと考えられる。

しかし、実際の結晶粒界においてPuの移動が生じているのかについては評価を行っていないために、今後M_3O_{8-Z}相の析出メカニズムの解明のための試験を実施して確認を行う必要がある。

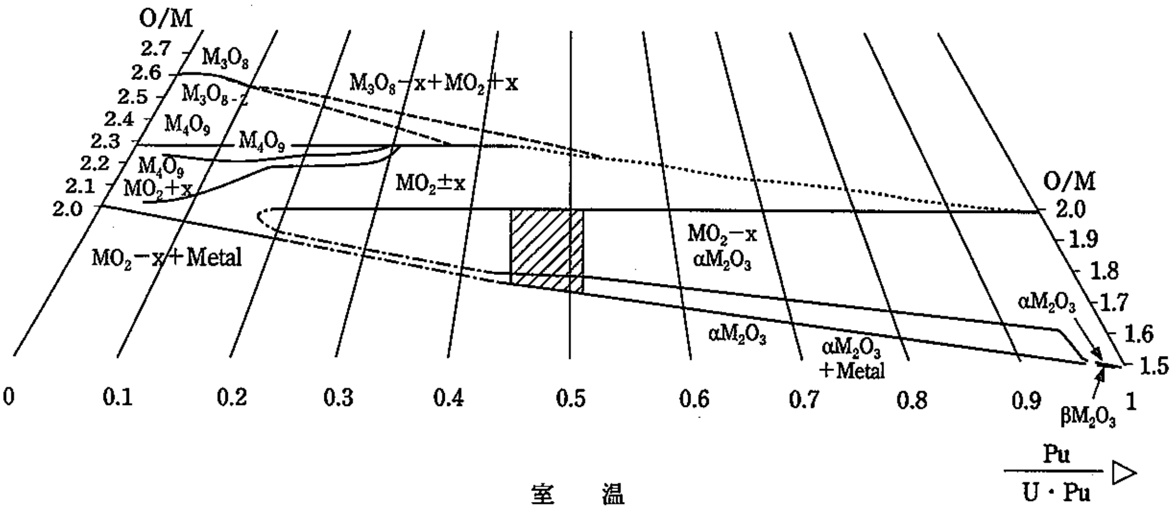

室　温

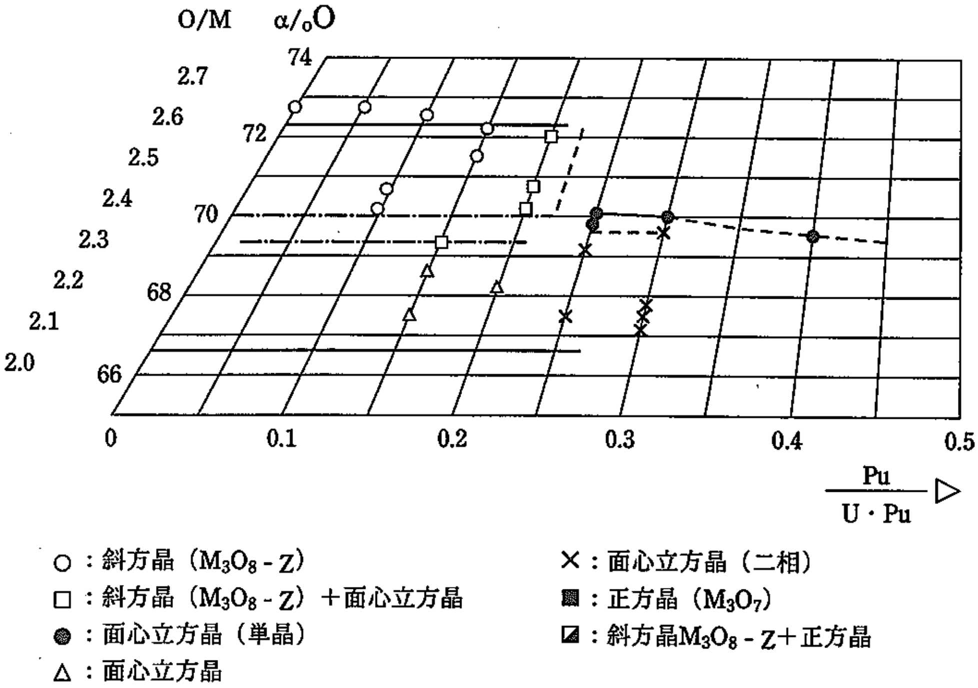

600℃

図４　U−Pu−O系状態図

5. まとめ

本試験で実施した、「もんじゅ」内側炉心燃料ペレットを対象とした酸化破砕試験の結果、酸化温度500℃付近3時間の空気中での酸化により破砕が起こり、乾式回収が適応できることが確認された。今回の試験結果から判断すると酸化破砕による乾式回収を行うには、500℃前後で酸化をおこなうのが最適であると考えられる。また、この時のX線回析による組織についての分析を行ったところ、MO_{2+X}相の中にM_3O_{8-Z}相とみられる相が存在していることが確認された。また、エッチング後の金相写真による観察においても2相分離が確認された。この事より、酸化破砕にはMO_{2+X}相（面心立方晶）の中に、M_3O_{8-Z}（斜方晶）相が析出することにより起こると考えられる。しかし、1000℃で酸化を行ったサンプルでもM_3O_{8-Z}（斜方晶）相が析出しているのが確認されたが、破砕は認められなかった。この違いは、M_3O_{8-Z}（斜方晶）相がPuの拡散を伴って結晶粒界から析出するか、Puの拡散を伴わずに粒内から析出するかによる違いと考えられるが、詳細なメカニズムについての検討は本試験のデータだけでは不十分で、今後M_3O_{8-Z}（斜方晶）相析出のメカニズムについての評価試験を行うことが必要である。

6. 参考文献

(1) C.SARI, U.BENEDICT AND H.BLANK : "METALLOGRAPHIC AND X-REY INVESTIGASIONS IN THE Pu-O AND U-Pu-O SYSTEMS", Thermodynamics of Nuclear Materials 1967, IAEA, Vienna 1968, p.587-611.

(2) C.SARI, U.BENEDICT : "STUDIES ON THE TERNARY SYSYTEM UO_2-U_3O_8-PuO_2" EUR 4136e, EUROPIAN ATOMIC ENERGY COMMUNITY, 1970.

(3) C.SARI, U.BENEDICT AND H.BLANK : "A STUDY OF THE TERNARY SYSTEM UO_2-PuO_2-Pu_2O_3" JOURNAL OF NUCLEAR MATERIALS 1970, Vol.35, p.267-277.

(その他)

- T.L.MARKIN AND R.S.STREET : "THE URANIUM-PLUTONIUM-OXYGEN TERNARY PHASE DIAGRAM" J.inorg. nucl. Chem.,1967, Vol.29, p.2265-2280.

3. MOX Fuel Irradiation Behaviour in Steady State (※) (Irradiation Test in HBWR)

S. Kohno, K. Kamimura

Plutonium Fuel Development Section

ABSTRACT

Two rigs of plutonium-uranium mixed oxide(MOX) fuel rods have been irradiated in Halden boiling water reactor (HBWR) to investigate high burn-up MOX fuel behaviour for thermal reactor. Objective of irradiation tests is to investigate fuel behaviour as influenced by pellet shape, pellet surface treatment, pellet-cladding gap size and MOX fuel powder preparation process.

The two ring have instrumentations for in-pile measurements of the fuel center-line temperature, plenum pressure, cladding elongation and fuel stack length change. The data taken through in-operation instrumentations have been analyzed and compared with those from post-irradiation examination. The following observations are made.

(1) PNC MOX fuels have achieved high burn-up as 59GWd/tMOX(67GWd/tM) at pellet peak without failure.

(2) There was no significant differences in fission gas release fraction between PNC MOX fuels and UO_2 fuels.

(3) Fission gas release from the co-converted fuel was lower than that from the mechanically blended fuel.

(4) Gap conductance was evaluated to decrease gradually with burn-up and to get stable in high burn-up region.

(5) No evident difference of onset LHR for PCMI in experimental parameters (pellet shape and pellet-cladding gap size) was observed, but it decreased with burn-up.

1. Introduction

Power Reactor and Nuclear Fuel Development Corporation (PNC) has been developing plutonium-uranium mixed oxide (MOX) fuel for fast breeder reactor (FBR), light water reactor (LWR) and the advanced thermal reactor (ATR).(1)

In this paper, the thermal and mechanical behaviour of MOX fuel obtained by both in-pile and post-irradiation examination (PIE) are presented. Two of instrumented irradiation rigs in HBWR were occupied for the experiments. One is named IFA-514 of which the irradiation started since July, 1979 and ended in November, 1988, having achieved the maximum burn-up of 49 GWd/tMOX(56GWd/tM) at pellet peak without failure. PIE had been carried out in Kjeller Laboratory until 1990. Three of six rods in IFA-514 rig have continued to be irradiated as a new rig(IFA-565). The irradiation started since November, 1990 and ended in October 1993. The maximum burn-up is now 59GWd/tMOX(67GWd/tM) at pellet peak. The other is named IFA-529 of which the irradiation was performed from July, 1980 to October, 1986 having achieved the maximum burn-up of 33GWd/tMOX(38GWd/tM) at pellet peak. PIE had been carried out also in Kjeller Laboratory until February, 1988.

The experimental parameters are pellet shape (hollow/solid) and pellet surface treatment (ground/as-sintered) for IFA-514/565 experiment, and pellet-cladding gap size and MOX fuel powder preparation method, i.e., direct co-conversion from mixed plutonium-uranium nitrate solution with microwave heating (MH Method)(2) and mechanically powder blending for IFA-529 experiment.

The experiments of IFA-514/565 and 529 are carried out as a part of joint research program between PNC and Japan Atomic Energy Research Institute (JAERI) wiht the participation in the OECD Halden Reactor Proiect.

2. Fuel Designs and Irradiation Conditions

2.1 Design of Rig

IFA-514/565

IFA-514 fuel assembly consists of six MOX fuel rods which are mounted on a circle with the upper and lower tie plates, two spacers and three stay tubes. A simplified configulations of instrumentation and experimented parameters is shown in Fig. 1. The fuel rods have the same fuel stack length of 1380mm.

After non destructive post irradiation examination for six fuel rods of IFA-514 were performed, three of them were reassembled to IFA-565. The design of the clusters is similar to that of IFA-514.

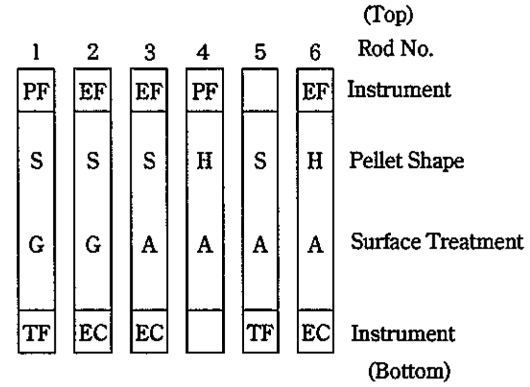

Pellet Shape S : Solid H : Hollow
Surface Treatment G : Ground A : As - Sintered
Instrument PF : Plenum Pressure
TF : Fuel Centreline Temperature
EF : Fuel Stack Length Change
EC : Cladding Elongation

Fig. 1 Simplified Configuration of Instrumentation and Experimental Parameters in IFA - 514

IFA-529

IFA-529 fuel assembly consists of two clusters which have six short MOX fuel rods respectively. All twelve rods are equipped with instruments in either or both ends. The pellet-cladding diametral gap size and MOX pellet fabrication process are experimental parameters. The configulation of instrmentation and experimental parameters is shown in Fig. 2. The fuel stack length is about 550mm.

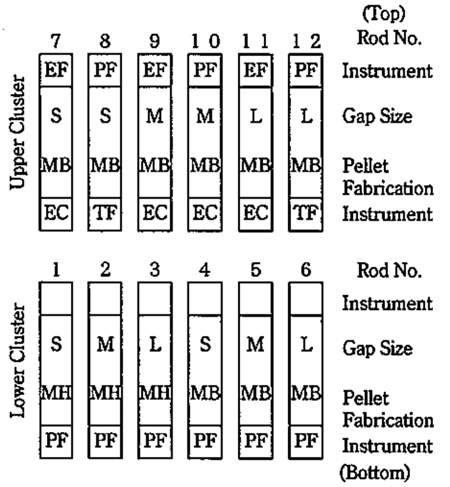

Gap Size S : Small M : Medium L : Large
Pellet MH : Co - conversion Method with Microwave Heating
Fabrication MB : Mechanical Blending Method

Fig. 2 Simplified Configuration of Instrumentation and Experimental Parameters in IFA - 529

2.2 Fuel Rod Specification

IFA-514/565

The fabrication data of IFA-514/565 fuel rods are given in Table. 1. The six fuel rods have the same cladding dimensions as those of BWR 8×8 fuel assembly. The fuel pellets are sintered of 5.8%PuO_2-Nat. UO_2 mechanically blended, powder 94% theoretical density, chamfered, and 10mm long. Pellet-cladding diametral gap size is range from 220μm to 260μm.

Table. 1 Specification Data of IFA - 514/565 and IFA - 529

	IFA - 514/565	IFA - 529
Pellet		
Fabrication Mathod	MB/1	MH*2/MB
Shape	Soild/Hollow	Solid
Surface Treatment	Ground/As*3	As
Outer Diameter (mm)	10.56	10.47~10.64
Inner Diameter (mm)	3.5*4	—
Density (%T.D.)	94	94
PuO_2 Concentration (wt%)	5.8	8.3
U−235 Enrich (wt%)	Nat.U	Nat.U
Cladding		
Material	Zry−2	Zry−2
Outer Diameter (mm)	12.53	12.53
Inner Diameter (mm)	10.80	10.80
Fuel Rod		
Fuel Stack Length (mm)	1380	550
Pellet−Clad Gap (μm Dia)	220~260	160~340
Filling Gas	He	He
Filling Pressure	1 atm	1 atm
Assembly		
Number of Fuel Rods	6	12 (Upper Cluster 6 Lower Cluster 6)

*1 Mechanical Blending Method
*2 Co−conversion Method with Microwave Heating
*3 As−Sintered Pellet
*4 only for Hollow pellet

IFA-529

The fabrication data of IFA-529 fuel rods are given in Table. 1. The pellets are enriched to 8.3%PuO_2-Nat. UO_2 and have 94% theoretical density. Pellet-cladding diametral gap size is in the range from 160μm to 340μm. The difference of MOX pellet fabrication process is shown in Fig. 3.

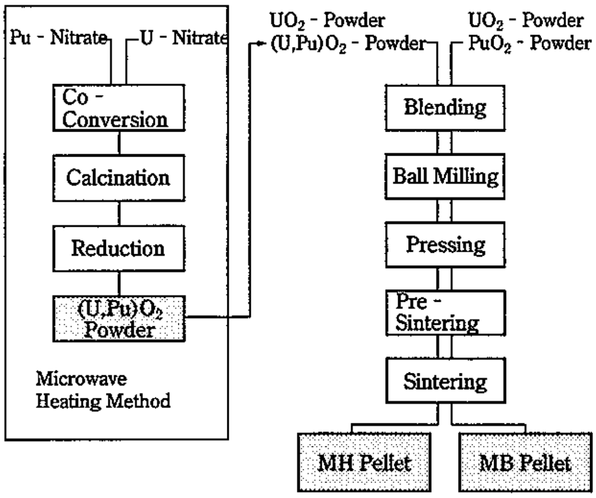

Fig. 3 Flow Chart of MOX Fuel Manufacturing Process

2.3 Irradiation Conditions

IFA-514/565

IFA-514 was irradiated about for 9.3 years. The six rods in IFA-514 were experienced almost same linear heat rating(LHR) except the rods loaded with hollow pellets. The maximum LHR of the rods loaded with solid pellets was 51KW/m. The mean LHR averaged for burn-up was 24KW/m. The pellet peak burn-up was nearly 49GWd/tMOX(56GWd/tM).

IFA-565 is irradiated about for 12.2 years up to now. The mean LHR averaged for burn-up was 23KW/m. The pellet peak burn-up was nearly 59GWd/tMOX(67GWd/tM).

IFA-529

IFA-529 was irradiated about for 6.3 years. The maximum LHR was 50KW/m. The pellet peak burn-up of lower cluster was nearly 31GWd/tMOX(35GWd/tM).

The irradiation conditions of two rigs are summerlized in Table. 2.

Table. 2 Irradiation data of IFA—514/565 and 529

		MAX.Pellet Peak LHR (KW/m)	Ave.LHR (Rod.Ave.) (KW/m)	Pellet Peak Burn-up (GWd/tMOX)	Average Burn-up (GWd/tMOX)	Irradiation *1 Time (Year)
IFA - 514 /565	Sollid Pellet Rod	51	24 (23)	49 (58)	40 (48)	9.3 (12.2)
	Hollow Pellet Rod	48	21 (21)	48 (59)	39 (49)	9.3 (12.2)
IFA - 529	Upper Cluster	50	22	33	25	6.3
	Lower Cluster	50	24	31	28	6.3

* 1 Irradiation time is definded by the time that the rig is in the reactor
* 2 ()including IFA - 565 as of August 1993.

3. Experimental Results and Discussions

3.1 Intemal Pressure of Fuel Rod

IFA-514/565

Fig. 4 shows the comparison of internal pressure between Rod-1 and Rod-4 in IFA-514. There is no significant difference of fabrication specifications between Rod-1 and Rod-4 except the central hole. The data are normalized in the condition of zero power and 240℃. It is seen in Fig. 4 that the rod internal pressure in Rod-1(solid pellet) is much higher than the of Rod-4(hollow pellet). Even though considering that the average LHR of Rod-1 is relatively higher than that of Rod-4 (3KW/m), the internal pressure of Rod-4(hollow pellet) might be still lower than that of Rod-1(solid pellet). It might be caused by the difference of fuel temperature and free volume between two rods.(3) (11)

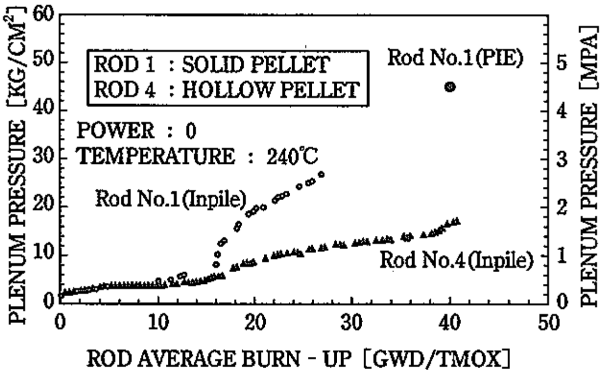

Fig. 4 Plenum Pressure of IFA - 514 as a Function of Burn - up

The internal pressures of the six fuel rods in the lower cluster of IFA-529 are plotted as a function of burn-up in Fig. 5. As those fuel rods are installed in the same lower cluster, the rod average powers are supposed to be approximately equal. It is seen that the internal pressures of Rod-1,2 and 3 loaded with MH pellets are lower than those of Rod-4,5 and 6 loaded with MB pellets. Fig. 5 also shows that except Rod-6, the smaller the pellet-cladding gap size, the lower the internal pressure is. This phenomenon might be explained by taking account of gap conductance dependence upon gap size.⑶⑸

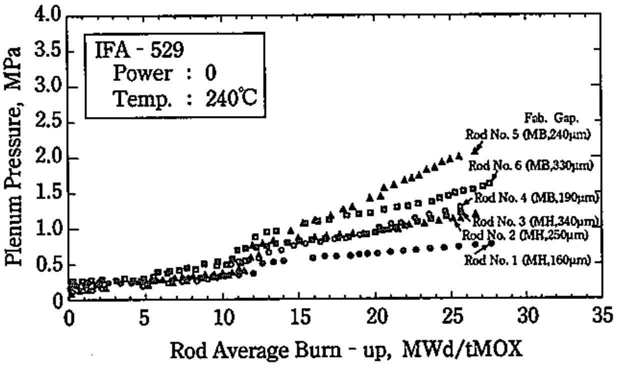

Fig. 5 Plenum Pressure in IFA - 529 at Zero Power as a Function of Burn - up

3.2 Fission Gas Release

Fig. 6 shows the comparison of fission gas release between Rod-1 of IFA-514 and Rod-4 of IFA-514/565. The fission gas release is remarkable from 15GWd/tMOX. It is seen that the fission gas release fraction of Rod-1 keeps to increase until the end of life up to 23% at the burn-up of 40GWD/tMOX.

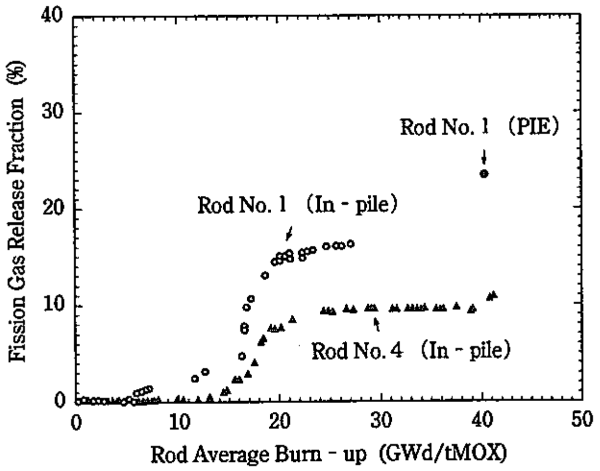

Fig. 6 Fission Gas Release Fraction of IFA - 514/565

On the contrary, the fission gas release fraction of Rod-4 decreases slightly to reach 9% at the end of IFA-514 life. But, at the beginning of the re-irradiation in IFA-565, the fission gas release fraction of Rod-4 increased slightly to reach 10%.

The fission gas release fraction of Rod-1 is much higher than that of Rod-4 at 40GWd/tMOX. Even if taking account of the difference of LHR (5KW/m), it seems the fission gas release fraction of Rod-1 (solid pellet) is larger than that of Rod-4 (hollow pellet). But it is necessary to confirm the in-pile data by using PIE data after the irradiation.

Fig. 7 shows the burn-up dependency of fission gas release fraction for BWR UO_2 fuels. The data of PNC MOX fuels for ATR and BWR are also plotted in fig. 7. The scattered region of PNC MOX fuel fission gas release fraction data is within that of UO_2 fuel. Fission gas release fraction in-pile and PIE data of Rod-1 (sollid pellet) and in-pile data of Rod-4 (hollow pellet) of IFA-514/565 are drawn in the same figure. Those two lines are also located in the scattered region of UO_2 fission gas release fraction data. It is remarkable that even at high burn-up of 40GWd/tMOX(45GWd/tM), fission gas release fraction of MOX fuel Rod-1 is almost equal.⑶~⑹

To compare the fission gas release fraction between different type of fuels, it is necessary to compare at the same linear heat rating.

Generally, fission gas release occurs above 10GWd/tM of burn-up, and the maximum linear heat rating experienced above 10GWd/tM is most effective on fission gas release fraction. A. Ohuchi et al.⑺ made an analysis of measured UO_2 fission gas release fraction as a function of maximum linear heat rating(≥10GWd/tM). The result is depicted in Fig. 8. In this figure, data of PNC MOX-fuels irradiation experiments are also plotted. It is seen that fission gas release fraction data of PNC MOX fuels are located in the band of UO_2.

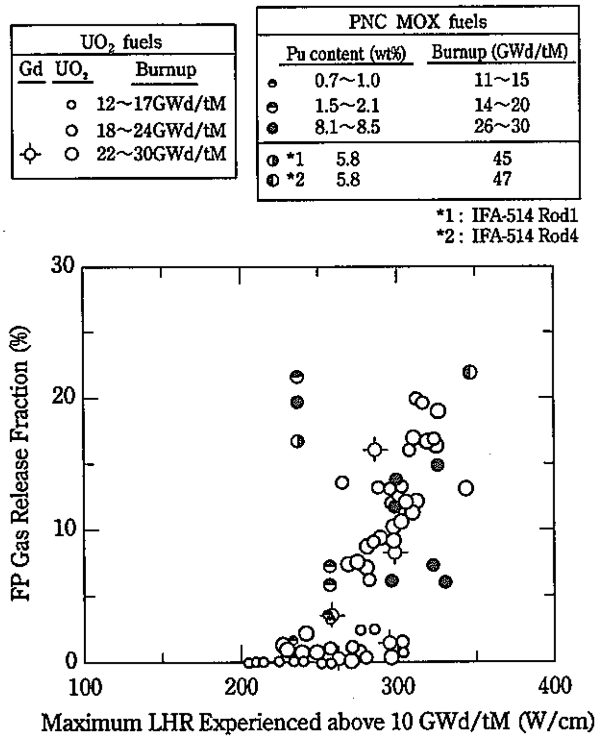

Fig. 8 Fission Gas Release Fraction of UO2 and MOX Fuels as Function of Maximum LHR Experienced above 10 GWd/tM

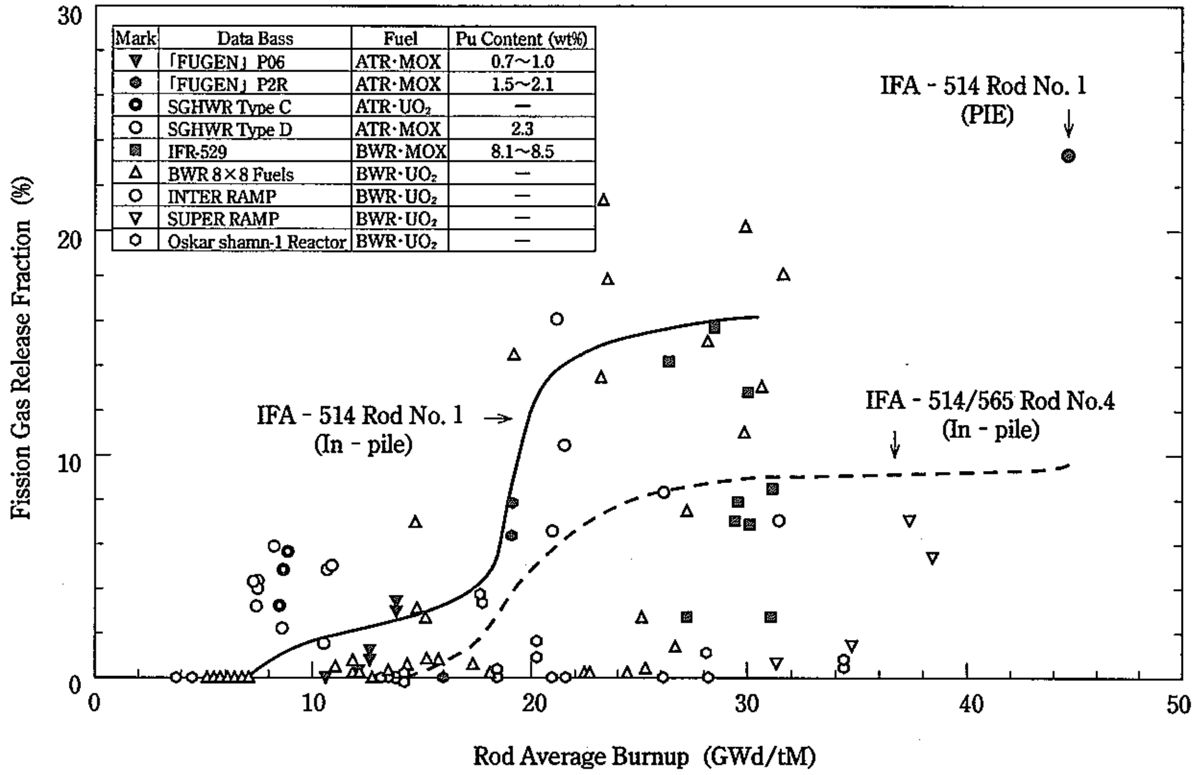

Fig. 7 Fission Gas Release Fraction of UO_2 and MOX fuels as a Function of Burn - up

3.3 Fuel Temperature

In each two fuel rods of IFA-514 and 529, thermocouples were inserted to measure fuel centerline temperature directly. Considering that fuel temperature depends on LHR, the temperature data corresponding to the LHRs of 10, 20 and 30KW/m were picked up for snalysis. Fig. 9 shows the temperature change of Rod-1 and 5 in IFA-514. Although there was a little difference between them up to the burn -up of 16GWd/tMOX, both temperatures become almost same value after the burn-up. No significant difference in pellet surface treatment is observed.

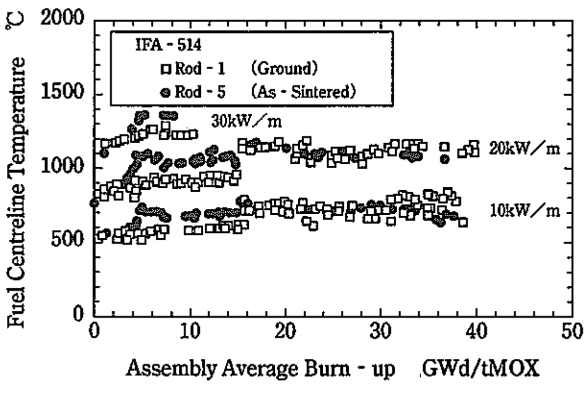

Fig. 9 Fuel Centreline Temperature at T/C Position in IFA - 514

In general, gap conductance increases according to LHR beceause of decrease of gap width. Calculation of gap conductance at various fuel burn-ups were made along the LHR of 20KW/m and it based on data sets of both coolant temperature and fuel centerline temperature. Results of the calculation is shown in Fig. 10. It is seen that gap conductance gradually decreases with burn-up, however in high burn-up region it becomes rather steady.[8]

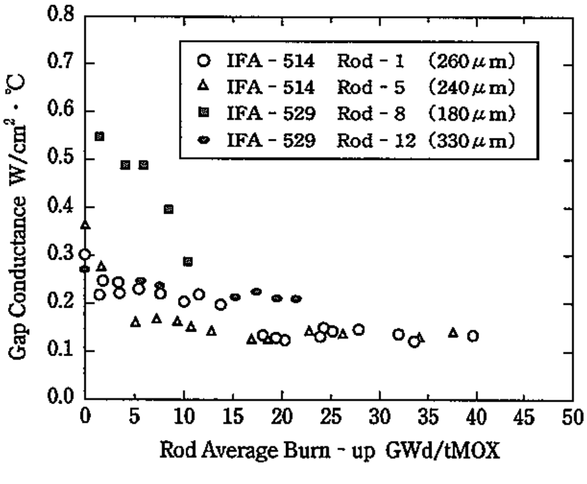

Fig. 10 Gap Conductance as a Function of Burn - up at a 20kW/m

3.4 PCMI Behaviour

In-pile PCMI behaviour was analysed using cladding extensometers of the fuel rods in IFA-514 and 529. In general, cladding elongates according to increase of power due to its thermal expansion. When hard contact between pellets and cladding occurs, cladding makes an abrupt elongation because cladding is dragged out by elongated fuel stack. For example, a relation between cladding elongation and LHR for Rod-3 in IFA-514 is shown in Fig. 11. The LHR at which cladding makes an abrupt elogation is called "onset LHR for PCMI". It is a good indicator to evaluate easily how PCMI occurs.

Fig. 12 shows a dependence of the onset LHR for PCMI on burn-up for Rod-2, 3 and 6 in IFA-514. The onset LHR for PCMI gradually decreases with burn-up. The onset LHR for PCMI of Rod-6 (hollw pellet) is slightly higher than that of other rods until 5GWd/MOX. However, no manifest difference in pellet shapes and pellet surface treatments is observed conceming about PCMI behaviour.

Fig. 13 also shows a dependence of the onset LHR for PCMI on burn-up for Rod-7,9, 10 significant PCMI is observed for any fuel rods. The dependence of the onset LHR for PCMI on burn-up in IFA-529 is similar to that in IFA-514. The onset LHR for PCMI would depend on pellet-cladding gap size, density change of pellet, relocation and rate of power increase. No significant dependence on pellet-cladding gap size is observed in IFA-529.(5)(8)(10)(12)

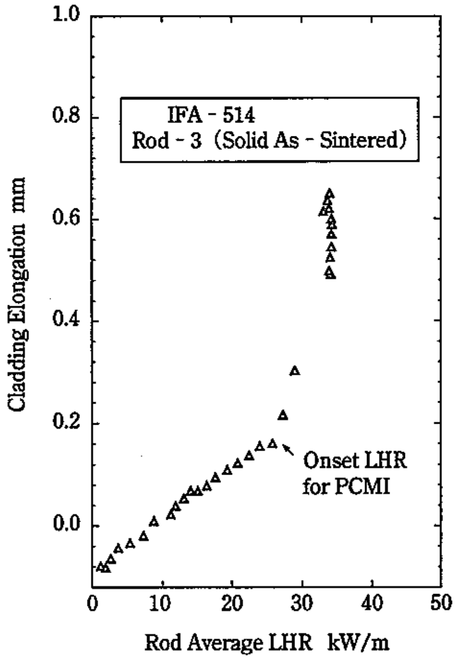

Fig. 11 Example of Dependence of Cladding Elongation on LHR

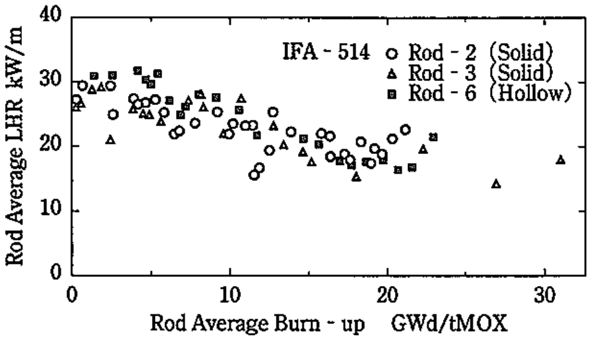

Fig. 12 Onset LHR for PCMI in IFA - 514 as a Function of Burn - up

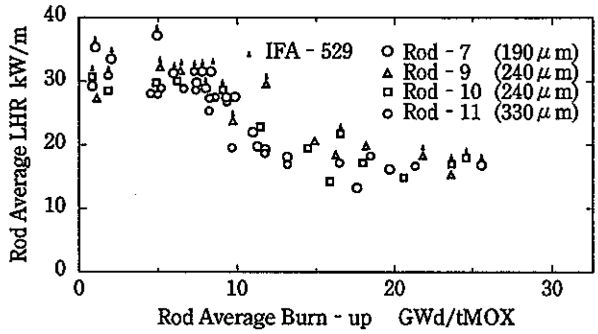

Fig. 13 Onset LHR for PCMI in IFA - 529 as a Function of Burn - up

4. Conclusions

Some conclusions derived from the data obtained by the instrumentations and the PIE are as follows.

(1) PNC MOX fuels have achieved high burn-up as 59GWd/tMOX(67GWd/tM) at pellet peak without failure.

(2) There was no significant differences in fission gas release fraction between PNC MOX fuels and UO_2 fuels.

(3) Fission gas release from the co-converted fuel was lower than that from the mechanically blended fuel.

(4) Gap conductance was evaluated to decrease gradually with burn-up and to get stable in high burn-up region.

(5) No evident difference of onset LHR for PCMI in experimental parameters (pellet shape and pellet-cladding gap size) was observed, bur it decreased with burn-up.

5. Reference

(※) KOHNO S., KAMIMURA K., MOX Fuel Irradiation Behariour in Steady State (Irradiation Test in HBWR), ANS International Topical Meeting on Light Water Reactor Fuel Performance, Frolida, 18-22 April, 1994.

(1) MISHIMA Y., Japanese Fuel Study Related to Extended Burn-up and Plutonium Recycling, IAEA Specialists' Meeting on Improved Utilization of Water Reactor Fuel with Special Emphasis on Extended Burnups and Plutonium Recycling, Mol, 1984.

(2) KOIZUMI M., OHTSUKA K., ISAGAWA H., AKIYAMA H., and TODOKORO A., Development of Process for the co-conversion of Pu-U Nitrate Mixed Solutions to Mixed-Oxide Power Using a Microwave Heating Method, Nuclear Technology 61,55(1983).

(3) KAMIMURA K., ABE T., and YOKOUCHI Y., Fission Gas Release Behaviour of MOX Fuel(IFA-514 and IFA-529), Workshop Meeting on Fission Product Release,Halden, 19-20 September, 1985.

(4) VITANZA C., KOLSTAD E., and GRAZIANI U., Fission Gas Release from UO2 Pellet Fuel at High Burn-up, ANS Topical Meeting on Light Water Reactor Fuel Performance, Portland, 1979.

(5) ABE T., KANEDA K., UEMATSU S. and SHIKAKURA S., Thermal and Mechanical Behavioours of MOX Fuel Rods in IFA-529, Enlarged Halden Programme Group Meeting, Leon, 8-13 May, 1988.

(6) SAIRANEN R., VITANZA C., KELPPE S., and RANTA-PUSKA K., Steady State Fission Gas Release from IFA-505 Data Evaluation Comparison with Release Models, HWR-157(1986).

(7) OHUCHI A. et al, Behaviour of Gaseous and Volatile Fission Products in BWR Fuel Rods, IAEA Specialists' Meeting on Post Irradiation and Examination and Experieence, Tokto, Japan 26-30 Nov. 1984.

(8) MISHIMA T., KAMIMURA K., and TANAKA K., Thermal and Mechanical Behavioours of MOX Fuel Rods, IAEA Technical Committee Meeting on Recycling of Pu and U in Water Reactor Fuels, Cadarache, France, Nov. 113-16, 1989.

(9) KAMIMURA K., MAEDA S., MISHIMA T., Irradiation Test of MOX Fuel Rods For Water Reactor(1)-Thermal Behaviours of IFA-529 Fuel Rods., Atomic Energy Society of Japan, Apr. 2-4, 1990.

(10) MAEDA S., KAMIMURA K., MATSUMOTO M., Irradiation Test of MOX Fuel Rode for Water Reactor(2)-Mechanical Behaviours of IFA-529 Fuel Rods., Atomic Energy Society if Japan, Apr. 2-4, 1990.

(11) KAMIMURA K., FP Gas Release Behaviour of High Burn -up MOX Fuel for Thermal Reactors., IAEA Technical Committee Meeting on Fission Gas Release and Fuel Rod Chemistry Related to Extended Burnup., Pembroke, Canada, Apr. 27-May 1, 1992.

(12) KIKUCHI K., NAKAJIMA Y., and MATSUMOTOM., Post Irradiation Examination of MOX Fuel Rods., Atomic Energy Society of Japan, Mar. 27-29, 1993.

4. マイクロ波加熱直接脱硝装置用オートチューナの開発(※)

加藤良幸，田中　泉，都所昭雄
転換技術開発室　Conversion and Chemical Process Development Section

Automatic microwave tuning system for Microwave Heating method.

Y.Katoh, I.Tanaka, A.Todokoro

In a microwave field, plutonium and uranium mixed solution is concentrated and denitrated by dielectric loss of material. This dielectric loss changes by temperature and states of material. This loss inducts the change of impedance of a oven. However, impedance of microwave generator is constant, so causes mismatching. This mismatching lowers the microwave heat efficiency.

We developed the automatic microwave tuning system. This system can minimize the reflection of microwave from the oven by continually adjusting impedance for Microwave Heating direct denitration method (called MH method).

1. 緒　言

マイクロ波加熱は、被加熱物質のマイクロ波電場における双極子回転あるいは格子振動による発熱を利用した方法であるため、物質の誘電特性が加熱効率に大きく影響する。一方、加熱による物質の状態変化（温度、形態など）は誘電特性の変化(1)(2)を伴い、それがマイクロ波の反射を引き起こし、マイクロ波加熱効率の低下につながる。それがマイクロ波加熱の一般的な欠点の一つになっている。

動燃が独自に開発したマイクロ波加熱直接脱硝法（以下、「MH法」という）は、硝酸プルトニウム／硝酸ウラニル混合溶液にマイクロ波を照射することにより加熱し、濃縮・硝酸塩の分解（脱硝）を経て酸化物に転換する方法である。MH法では、連続的に顕著な被加熱物質の状態変化を伴うために、一般的なマイクロ波加熱である食品等の再加熱や乾燥などの場合と比較すると、加熱効率の低下がより起こり易い条件にある。

被加熱物質の誘電特性変化の影響を少なくする方法としては、整合器（チューナ）をマイクロ波加熱装置に取り付けるのが一般的であり、MH法では従来から3スタブチューナが用いられている。しかし、このチューナは、手動で煩雑な調整をする構造であるために、連続的な誘電特性変化に対しては十分な調整をすることは困難である。そこで、加熱効率の向上と調整の自動化を図ることを目的として、マイクロ波加熱中に自動的に反射波を最小に調整する整合器（以下、「オートチューナ」という）を開発(3)した。

2. オートチューナ装置の試作

2.1 整合(4)の必要性及び概念

マイクロ波加熱装置の電気等価回路を簡略化して示すと図1のようになる。この回路において、R_Sが発振器側、R_Lが負荷側（マイクロ波加熱オーブン全体）の特性インピーダンスを示してあり、ここでR_Lは負荷の誘電特性変化に対応して変化する。この時の発振器回路電圧をVとすると、負荷で消費する電力Pは(1)式で示される。

$$P = I^2 \cdot R_L = \frac{V^2}{R_S + R_L} R_L \quad \cdots\cdots \quad (1)$$

この回路において、R_SとR_Lの比を変化させると消費電力Pは、図2のように変化する。この図から負荷側に最大の電力を供給するには、消費電力Pが最大になるように$R_S = R_L$の条件を満たすようにすれば良い。整合とは、これを行うために図3に示すようにマイクロ波発振器と負荷側の間に整合器を挿入してインピーダンス調整を行うことにより、見かけ上のマイクロ波発振器と負荷との特性インピーダンスを等しくする操作である。

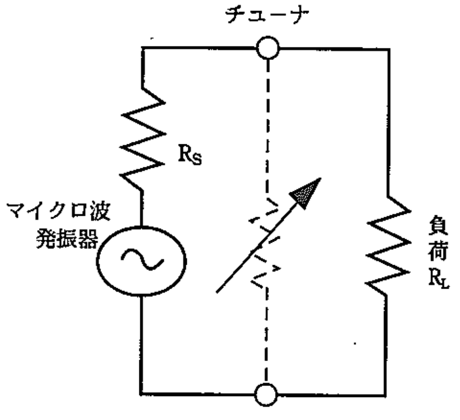

図１　マイクロ波加熱装置の電気等価回路

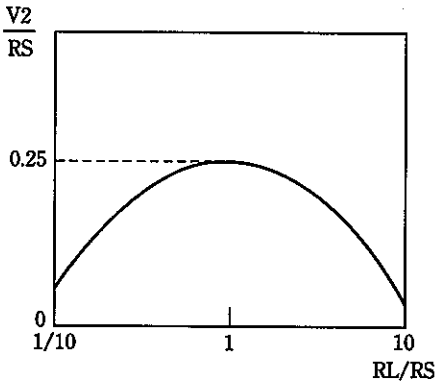

図２　負荷抵抗変化による消費電力変化

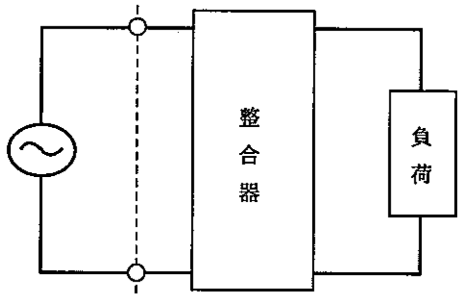

図３　発振回路とのインピーダンス整合

2.2　オートチューナの設計

2.2.1　従来の整合器の特徴とオートチューナへの適用性

一般的な整合器は、スタブ位置を手動で移動することによりインピーダンスを調整するものである。このタイプのチューナでは、位置調整したスタブを固定して使用するため、MH法のようにマイクロ波加熱オーブンの特性インピーダンスが大きく、かつ、それが連続的に大きく変化するような場合には、十分な整合を行うことは難しい。そこで、マイクロ波加熱オーブンと特性インピーダンス変化に応答して自動的にスタブ位置を調整するオートチューナを開発することを目標とした。

従来からマイクロ波回路に用いられているスタブチューナの主なものとしては、EHチューナ，3スタブチューナ，スライディング・スタブチューナの3種がある。これらの中から開発目的に適応できるものを選定し、自動化を図ることとした。

3種類のチューナの比較を表1に示す。EHチューナは、スタブの駆動トルクが大きく、かつ、インピーダンス調整が難しい構造であること、3スタブチューナは、3本のスタブをそれぞれ位置調整することにより整合を行うために時間がかかることから、自動化には向いていない。一方、スライディングスタブチューナは、1本のスタブを縦・横方向動作させることのみで整合が行えるため、スタブ位置調整の自動化は容易である。そこで、スライディングスタブチューナを開発する装置のベースチューナとして選定した。

表１　各種チューナの比較

	駆動箇所	特長及び整合操作性	オートチューナ開発上の課題	自動整合の容易さ
3スタブチューナ	3	安価、耐電力性確保が容易。3つのスタブを順次調整し、数回ずつ繰り返す必要有り。	スタブ相互の干渉があり，動作回数が多く，速度上昇が困難。	△
スライディング・スタブチューナ	2	目的とする特性インピーダンスの絶対値及び位相角を直接設定可能。	導波管開口部からのマイクロ波漏えい防止が必要。	◎
EHチューナ	2	ミリ波・大変動負荷向き。微小調整がむずかしい。	短絡板の安定した電気導通確保がむずかしい。	×

2.2.2　オートチューナによる整合動作

オートチューナを用いてマイクロ波回路の整合を行う場合、整合の度合いを判断する指標は、入射電力と反射電力の比であるが、通常その値を直接用いるのではなく、(2)式で求められる定在波比（以下VSWRという）を用いる。

$$\mathrm{VSWR} = \frac{1+\rho}{1-\rho} \quad \cdots\cdots(2) \qquad ここで,\ \rho = \frac{反射電力}{入射電力}$$

この電力信号は、マイクロ波入・反射電力の一部（mWオーダ）を取り出して電力計に送って計測する。

オートチューナによる整合の動作を図4により説明する。まず、被加熱物質の状態変化等により、負荷側とマイクロ波発振器に特性インピーダンス差が生じる。それが点A1であり、VSWRが大きく、反射電力が大きい状態である。そこで、オートチューナのスタブを横軸方向に動かし位相角を変化させ、VSWR最小値である点A3に調整する。しかしながら、その調整は、スタブ移動前後のVSWRを検知比較して最小点を探すため、直接、点A3を見つけることが出来ず、点A3を一旦通過して点A2に到達してしまう。そこで現在点と過去測定点のデータから曲線を近似して最小点である点A3を見つける。これにより、A曲線での整合は終了したが、さらにY軸の移動を行うことにより、スタブで発生させるインピーダンスの絶対値の増減が行われ、曲線全体が上下に変動し、最小値となるB曲線に到達して整合が終了する。

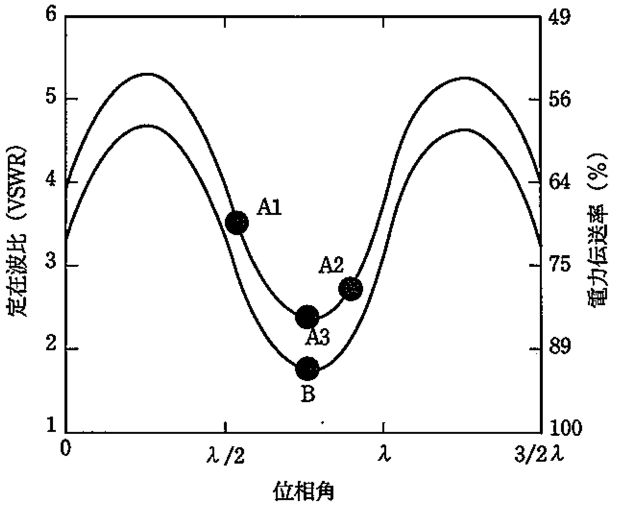

図4　オートチューナによる整合動作

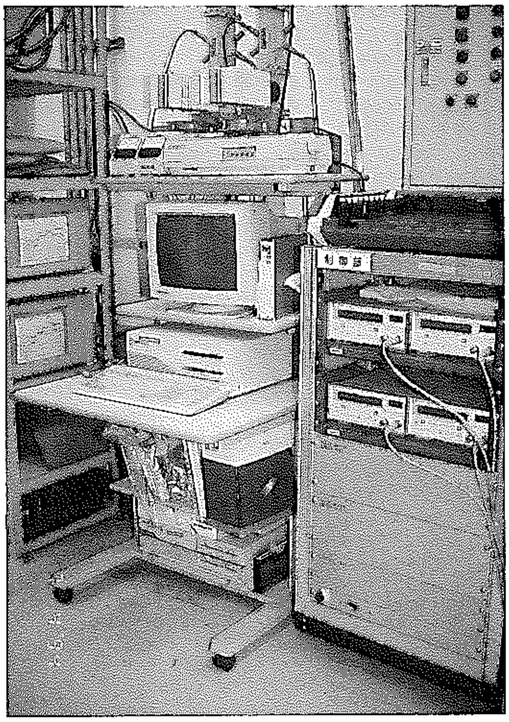

写真1　オートチューナ操作・制御部

写真2　チューナ部

3.　オートチューナの設計及び試作

2.2.1項で選定したスライディング・スタブチューナは、主に計測用及び可変疑似負荷として用いられるものであり、通常市販品は小電力での用途に限られるために、MH法のような大電力（今回試験装置で1.5kW／系統，実規模施設では5kW／系統）での使用ではマイクロ波の漏えいが問題になる構造となっている。そこで、スタブ周辺部に同軸状のチョークを設けることにより、マイクロ波電界の集中するスタブ周辺部からのリークを防止するとともに、スリット状の開口部については、非接触式のガイド板で、覆った。この対策により、マイクロ波の漏えい量は、1kWの入力時でアメリカ規格協会(ANSI)が規定する5mW／cm^{2}の1／10である0.5mW／cm^{2}以下を達成できた。

次に、スタブの駆動方法は、装置上の性能要求である正確かつ高速動作可能なものでパソコンとの取り合いが容易であるものでなくてはならない。このため、各種モータの動作速度や停止精度及びパソコンでの制御性等について検討し、4−5相パルスモータを選定した。さらに、マイクロ波の入・反射電力をリアルタイムで取り込めるようにするために、通常のパソコン制御で行うような機器間の通信（RS−232C等）を採用せず、電力計のアナログ信号をパソコンに入力した。

また、チューナの制御として、マイクロ波加熱系統が2系統であるため、並列同時制御を行うようにソフトを組んだ。

装置の構成を図5に、オートチューナの操作・制御部とチューナ部の外観写真を写真1，写真2に示す。

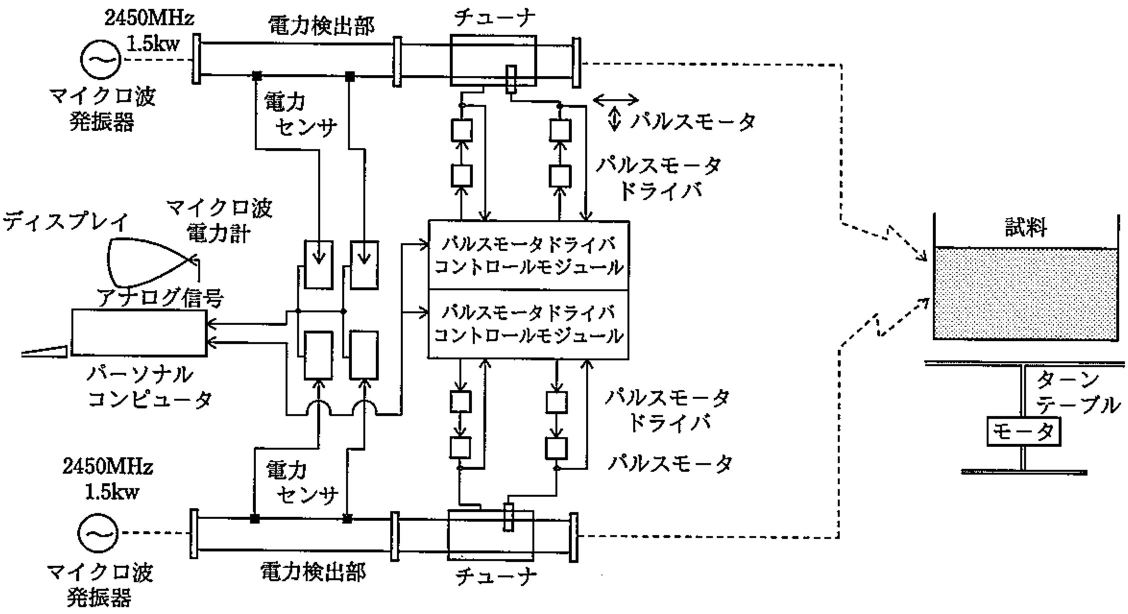

図５　オートチューナの構成

4.　装置の基本特性確認試験

オートチューナを用いて、硝酸ウラニル溶液及び硝酸プルトニウム／硝酸ウラニル混合溶液（以下混合溶液という）の脱硝試験を行い、マイクロ波加熱効率及び生成する脱硝体の物性等に関して従来からの整合方法である3スタブチューナによるスタブ固定の場合との比較を行った。

4.1　試験装置

試験装置はマイクロ波発振器，電力検出部，チューナ脱硝オーブンの順に導波管を用いて接続した。試験装置の構成を図6に示す。主な装置の仕様を表2に示す。

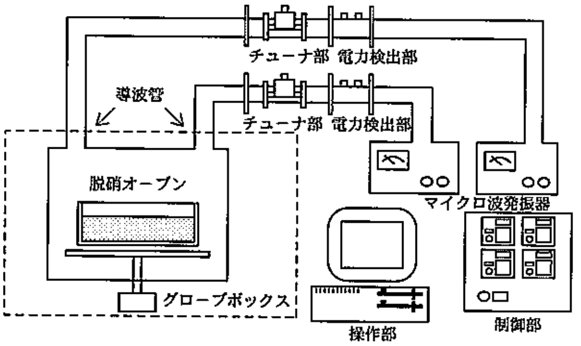

図６　試験装置の構成

表２　装置の仕様

脱硝装置		脱硝皿
マイクロ波発振出力	1.5kw×2基	窒化珪素製 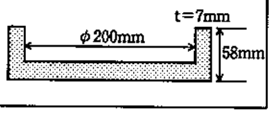
マイクロ波電力計	ダイオード検波型×4台	
導波管長さ	8400/8100mm	
オーブン容量	φ 500×550mm	
ターンテーブル	Max.9 rpm可変	
オーブン排気風量	490Nℓ/min	

4.2　試験方法

硝酸ウラニル溶液または混合溶液を所定量計量して脱硝皿に給液したのち、マイクロ波を照射し、溶液を加熱，濃縮，脱硝させた際の脱硝終了までの時間及びVSWR値の変化を測定した。また、脱硝生成物の状態観察及び熱分析を実施した。なお、同一条件での試験をオートチューナ使用時とスタブ固定時でそれぞれ実施した。後者の場合は、脱硝時に最も整合がとれる条件にスタブを固定した。試験条件を表3に示す。

表３　脱硝試験時の溶液条件

		Pu濃度 (g/L)	ウラン濃度 (gU/L)	硝酸濃度 (N)	試料容量 (L)	試験繰返 n
硝酸ウラニル溶液脱硝試験		——	240	1.5	0.8	3
硝酸Pu/U混合溶液脱硝試験	オートチューナ使用時	125	125	3	0.8	1
	転換施設脱硝工程（スタブ固定）	125	125	3	8	——

4.3　試験結果及び考察

試験結果を表4に示す。オートチューナ使用時にはスタブ固定条件と比較して、脱硝終了時間が平均8%短縮するとともに、VSWR値についてもオートチューナ使用時の方が全体的に低く抑えることができた（図7参照）。このことは、オートチューナを使用することで常に整合が行えるため、マイクロ波利用効率が向上していることを示している。なお、脱硝終了時間のばらつきについては、両条件とも同じ程度であり、オートチューナの動作の安定性を確認することができた。

脱硝生成物の揮発性不純物量（550℃での加熱減量）は、5〜10%程度であり、脱硝状態の観察結果でも差が無かったことから、オートチューナ使用による脱硝生成物への影響も無いことが確認できた。

さらに、オートチューナの作動に関する不具合はこれまで生じておらず、マイクロ波の漏えいについての当初の設計値を下回るレベルであった。

以上のことから、オートチューナの性能が当初の設計どおりであるあることが確認でき、それを使用することにより、脱硝生成物の物性等に影響を与えることなく、マイクロ波利用効率を向上できることがわかった。

表４　脱硝試験結果

	スタブ固定時*1				オートチューナ使用時			
	試験No.	脱硝終了時間（分）	加熱減量（w/o）		試験No.	脱硝終了時間（分）	加熱減量（w/o）	
			表面	底部			表面	底部
硝酸ｳﾗﾆﾙ溶液試験	MU-1	２９	８	６	AU-1	２５	６	４
	MU-2	２６	１２	１２	AU-2	２６	１３	１３
	MU-3	３０	１１	１３	AU-3	２７	６	１０
	平均	２８	１０	１０	平均	２６	８	９
Pu/U溶液試験	—	—	７	７	AP−１	２７	９	９

＊１　Pu/U溶液試験のスタブ固定時データは転換施設脱硝工程のものである。

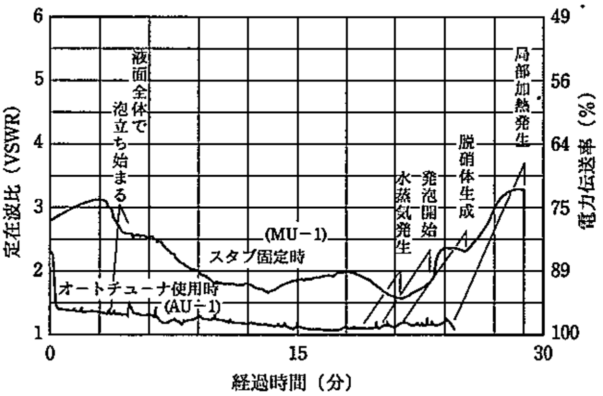

図７　硝酸ウラニル溶液脱硝時のVSWR変化の１例

5.　実規模施設への適用性

プルトニウム転換技術開発施設において現在稼働しているマイクロ波脱硝装置は、5kWのマイクロ波発振器4基が1つのオーブンに取り付けられている。今回の装置の耐電力仕様は2kWではあるが、設計裕度を大きく取ってあるため、若干のマイクロ波漏えい対策の補強を行うことで対応は容易にできる。さらに、マイクロ波加熱系統数が増加するため、チューナも4系統化する必要があるが、より高速で演算処理できるCPUの採用及び多系統同時並列制御を可能にするためのソフト変更を行うことで対応できる。

これらの処置により、今回開発したオートチューナを実規模施設へ適用させることは可能である。

この装置の設計・製作を行い、プルトニウム転換技術開発施設脱硝工程に設置して平成6年度に実証試験を実施する予定である。

6.　結　論

マイクロ波加熱効率を向上させるためのオートチューナは、ベースチューナにスライディング・スタブチューナを採用し、マイクロ波の入・反射電力を指標にして自動制御することで完成させることができた。このオートチューナを使用することで、以下の効果が得られることが確認できた。

①煩雑な整合操作を自動化できることで省力化を図ることができ、マイクロ波の利用効率が平均で8%程度向上し、加熱時間を短縮できた。

②マイクロ波加熱処理のたびに負荷の濃度，体積等が異なり、それによるマイクロ波吸収特性（特性インピーダンス）の変化に対応して、常に最良の加熱効率で処理することが可能となった。

7.　参考文献

(※) 加藤良幸，田中泉，他“マイクロ波加熱直接脱硝装置用オートチューナの開発”日本原子力学会　1993秋の大会　K1(1993).

(１) 大島博文，辻信雄，“マイクロ波加熱法によるプルトニウム・ウラン混合転換連続プロセス”
日本原子力学会誌　26　[4]　(1984).

(２) 加藤良幸，田中泉，他　“ウラン及びプルトニウム化合物のマイクロ波領域での誘電率”
日本原子力学会　1993春の年会　K18　(1993).

(３) 近藤　勲，鈴木徹，“マイクロ波加熱装置”
日本特許出願番号：平2−313129
ｱﾒﾘｶ特許受理番号：07/719，535 (Dec. 22, 1992).

(４) 佐藤　進，“アンテナ・電波伝搬”オーム社 (1976).

5. MOX燃料電解溶解試験（※）

木原義之，都所昭雄，大高昭博*，小笠原誠洋*
転換技術開発室　Conversion & Chemical Process Development Section
*検査開発株式会社　Inspection Development Corporation

Electrolytic Dissolution Test of MOX Fuel

Y.Yoshiyuki, A.Todokoro, A.Ohtaka* and M.Ogasawara*

A method of electrolytic dissolution has been studied to dissolve plutonium dioxide in nitric acid. This dissolution uses Ag^{2+} as an ionic catalyst to oxidize PuO_2(IV) to PuO_2^{2+}(VI). Ag^{2+} is generated by electrolysis of silver nitrate.

This method is to be developed for dissolving mixed oxide, or decontamination of plutonium contained in solid wastes in plutonium fuel fabrication facility. This report summarizes the effect of UO_2 on PuO_2 dissolving velocity with wide range of the MOX in ratio of Pu to U.

1. はじめに

硝酸中において、二酸化プルトニウム(PuO_2)がPu^{4+}イオンとなる溶解生成反応の自由エネルギー($\Delta G°$)は、+32.04kJ/mol(1)であることから、PuO_2は、硝酸にきわめて溶解し難い金属酸化物の一つである。

PuO_2の硝酸への溶解技術向上のために様々の研究が行われている(2)。その一つとして硝酸にフッ化水素酸を添加する方法があるが、溶解速度が時間経過とともに著しく低下する(3)、あるいはPuを精製するときのフッ化物イオンの除去が困難(4)等の理由で工学規模での利用には課題がある。また、硝酸－フッ化水素酸にヒドラジンを添加することで、PuがⅢ価まで還元されるために、溶解速度が向上する(5)という報告例もある。

一方、電解酸化反応で生成するAg^{2+}等の酸化剤を用いるPuO_2の溶解法（電解溶解法）に関する研究が、Fontenay-aux Roses研究所(6)、Oak Ridge国立研究所(7)、および日本原子力研究所(4),(8)で行われている。この方法は、(1)式に示す反応で生成したⅡ価の銀(Ag^{2+})が、(2)式に示す反応でPuO_2をPuO_2^{2+}まで酸化することで硝酸への溶解が進行するものであり、室温における溶解速度が速いだけでなく、(1)式の反応でAg^{2+}を再生できる利点を有している。

$$Ag^{+} \rightarrow Ag^{2+} + e^{-} \qquad (1)$$

$$PuO_2 + 2Ag^{2+} \rightarrow PuO_2^{2+} + 2Ag^{+} \qquad (2)$$

われわれは、この電解溶解法をプルトニウム燃料スクラップからのPu回収のための溶解およびPuO_2付着固体廃棄物の除染技術等に適用するための開発を進めている。プルトニウム燃料製造施設ではPuO_2－UO_2混合酸化物(MOX)として取り扱うことが多く、これらに適用する場合の溶解対象はMOXとなる。したがって、種々のPuO_2含有率となるよう機械混合したMOX粉末を用いた溶解試験の結果、PuO_2の溶解速度に及ぼすUO_2の影響が明らかになったので報告する。

2. 試　験

2.1 溶解試料

溶解に用いた試料は、PuO_2粉末とUO_2粉末を所定のPuO_2含有率となるようそれぞれ秤量し、機械混合した。PuO_2粉末は、しゅう酸沈殿法で酸化物に転換したものであり、約3%の^{241}Amを含む。UO_2は、マイクロ波加熱直接脱硝法で酸化物に転換したものであり、天然ウランである。それぞれの粉末物性を表1に示す。

表１　溶解試料の粉末物性

項　　　目		PuO_2	UO_2
転換時の熱処理温度（℃）	:	８００	８５０
比表面積（m^2／kg）	:	7.74×10^3	1.30×10^3
平均粒径（μm）	:	1.10	1.30
Pu、U含有率（%）	:	85.4	87.7

2.2 試験装置および条件

試験装置は、図1に示すように溶解槽と定電流発生装置から構成されている。溶解槽は、陽極槽と陰極槽がAl_2O_3製の隔膜（細孔5μm）で隔たれており、陽極槽の外側には陽極電解液を恒温にするための冷却ジャケットを取り付けている。定電流発生装置は、高砂製作所製SX035－30型を使用した。これらの仕様を表2に示す。

試験は、PuO_2含有率をパラメータとしてPuO_2の溶解速度を測定する試験と陽極電解液遊離酸濃度をパラメータとしてAg^{2+}の生成速度を測定する試験の2種類を実施した。

いずれの試験においても陽極電解液の硝酸銀濃度は

0.15mol/ℓ、陰極電解液には4mol/ℓ硝酸溶液を用い、陽極電解液を回転子で撹拌しながら印加電流5.6A（電流密度824A/m²）、温度25℃で定電流電解を行った。時間毎に陽極電解液をサンプリングし、Ag^{2+}濃度あるいはPu、U、遊離酸濃度を分析した。なお、陽極電解液量は0.8ℓ、陰極電解液は0.2ℓとし、サンプリング後の液量が一定となるよう陽極電解液を添加した。Ag^{2+}の生成速度を測定する試験では、陽極電解液遊離酸濃度を1、2、3、4mol/ℓとした。PuO_2の溶解速度を測定する試験の条件は、表3に示すように設定した。

なお、硝酸は関東化学㈱製特級(d=1.38)、硝酸銀は関東化学㈱製（純度99.9%）を使用した。

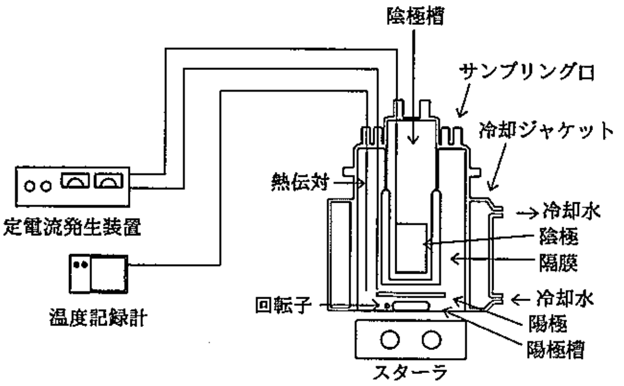

図1　電解溶解試験装置概略図

表2　試験装置の仕様

〔溶解槽〕		
陽極材質	:	Pt
陽極面積（m²）	:	6.3×10^{-3}
陽極槽体積（ℓ）	:	1.5
陰極材質	:	Tiに2μmPtコーティング
陰極面積（m²）	:	2.24×10^{-2}
陰極槽体積（ℓ）	:	0.33
〔定電流発生装置〕		
型式	:	SX 035－30
出力電圧（V）	:	max. 30
出力電流（A）	:	max. 30

表3　PuO_2の溶解速度測定試験条件

PuO_2重量（kg）	:	33×10^{-3}
PuO_2含有率（%）	:	100、50、30、20
陽極電解液遊離酸濃度（mol／ℓ）	:	4

2.3　分析方法

Pu濃度は、Puの原子価をⅥ価に調整したのち、0.05mol/ℓ硫酸第一鉄（Ⅱ）アンモニウム溶液を過剰に添加し、

$$PuO_2^{2+}+2Fe^{2+}\rightarrow Pu^{4+}+2Fe^{3+} \qquad (3)$$

の反応で消費した残りのFe^{2+}を0.05mol/ℓ重クロム酸カリウム溶液で滴定して分析(9)した。

遊離酸濃度およびU濃度は、0.1mol/ℓ水酸化ナトリウム溶液を用いた中和滴定で遊離酸濃度を求めたのち、過酸化水素を添加してウランを沈澱させ、遊離した酸根を再び0.1mol/ℓ水酸化ナトリウム溶液を用いた中和滴定でU濃度を求める、中和滴定－過酸化水素沈澱アルカリ中和滴定法(10)で分析した。

Ag^{2+}濃度は、試料に0.1mol/ℓ硝酸セリウム（Ⅲ）溶液を添加し、

$$Ag^{2+}+Ce^{3+}\rightarrow Ag^{+}+Ce^{4+} \qquad (4)$$

の反応により生成したCe^{4+}を0.1mol/ℓしゅう酸ナトリウム溶液で滴定(7)して分析した。

滴定装置は、平沼産業㈱製平沼自動滴定装置COM－TITE－900を使用し、電極はPu濃度分析用として堀場㈱製白金複合電極＃6810－06Tを、Pu濃度以外の分析用には平沼産業㈱製白金電極PT－301を使用した。

3.　試験結果及び考察

表3に示した条件で測定したPuO_2、UO_2の溶解挙動および遊離酸濃度変化について、PuO_2のみの結果を図2に、MOXの結果を図3に示す。いずれの条件においてもPuO_2は完全に溶解したが、PuO_2の溶解速度はUO_2に影響を受けていることがわかる。すなわち、PuO_2のみのときの溶解速度は一定であるにもかかわらず、MOXのときのPuO_2の溶解はUO_2の溶解が終了に近づいたあたりから始まり、直線の傾きから求めた溶解速度は表4に示すように、UO_2の比率が高くなるほど遅くなった。

UO_2の溶解反応はAg^{2+}に関係なく速やかに進行し、NO_Xを発生する。桜井ら(11)は、(5)式に示す反応で生成したNOの一部が(6)式により速やかにNO_2になると報告している。本試験においても図3に示すように、UO_2の溶解に伴って遊離酸濃度が減少した。

$$3UO_2+8HNO_3\rightarrow 3UO_2(NO_3)_2+2NO+4H_2O \qquad (5)$$

$$NO(g)+2HNO_3(\ell)\rightarrow 3NO_2(g)+H_2O(\ell) \qquad (6)$$

PuO_2の溶解速度を律速するAg^{2+}の生成速度(4)は、図4に示すように陽極電解液遊離酸濃度に比例して速くなった。Ag^{2+}の濃度を1×10^{-2}mol/ℓ程度として温度を25℃に保ち、時間経過とともにAg^{2+}の濃度変化を測定した結

果、図5に示すように遊離酸濃度が高いほどAg^{2+}は安定であった。このためAg^{2+}の生成速度は、遊離酸濃度に比例するものと考えられる。

すべてのUO_2が(5)式にしたがって溶解したものと仮定したときの遊離酸濃度におけるAg^{2+}の生成速度を図4中に示した直線の式から求め、(2)式に基づき、$PuO_2$1モルの溶解にAg^{2+}2モルが必要として計算したPuO_2の溶解速度は、表4に示すように実測値と良く一致した。

以上から、PuO_2の溶解速度がUO_2比率が高くなるに従い遅くなるのは、UO_2の溶解により遊離酸濃度が低下し、Ag^{2+}の生成速度が遅くなるためと考えられる。

また、溶解反応初期においてPuO_2の溶解開始が遅れる原因は、Ag^{2+}を含む硝酸溶液に亜硝酸の分解で生成したNO_XガスをパージしたところAg^{2+}が速やかに還元されたことから、(5)、(6)式に示すUO_2の溶解で発生するNO_XガスによりAg^{2+}が還元されるためと考えられる。

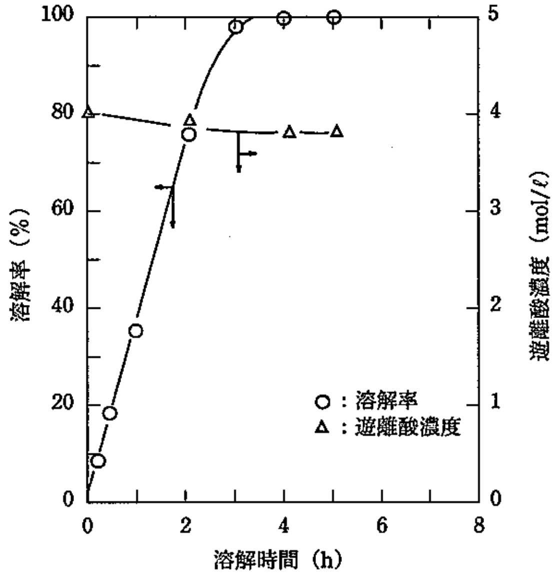

図2　PuO_2粉末溶解挙動

表4　PuO_2の溶解速度

PuO_2含有率（%）	PuO_2の溶解速度（kg/h） （実測値）	（計算値）
100	11.9×10^{-3}	11.5×10^{-3}
50	11.0×10^{-3}	10.6×10^{-3}
30	9.6×10^{-3}	9.4×10^{-3}
20	3.1×10^{-3}	7.9×10^{-3}

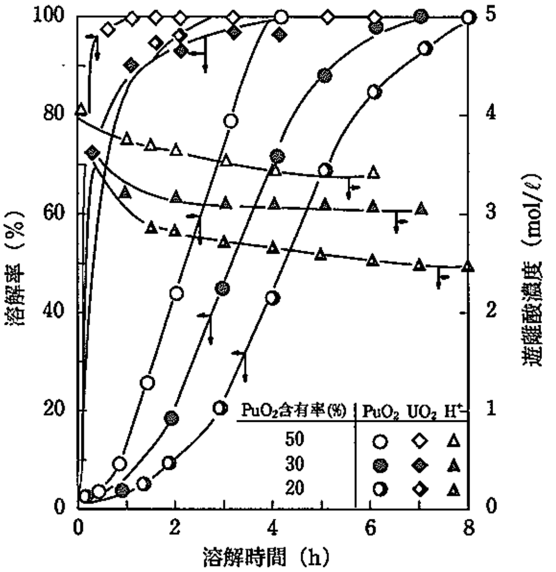

図3　MOX粉末溶解挙動

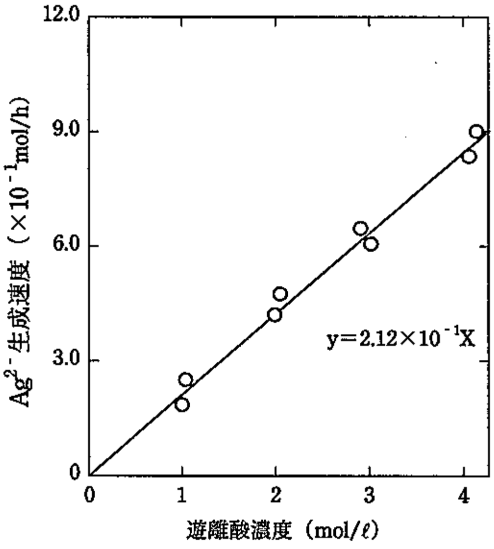

図4　Ag^{2+}生成速度と遊離酸濃度の関係

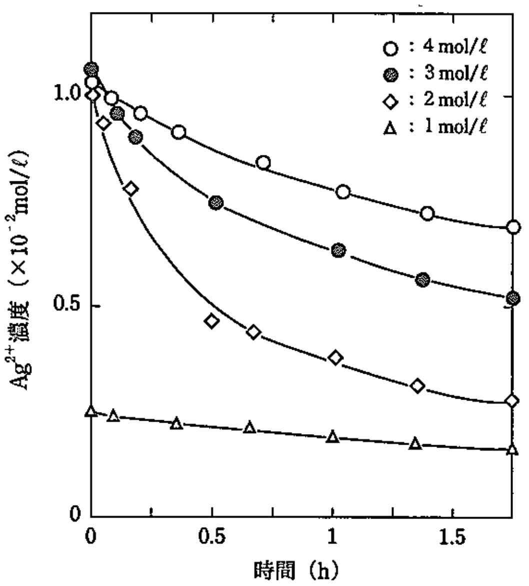

図5　Ag^{2+}濃度変化への遊離酸濃度の影響

4. おわりに

Ag^{2+}を酸化剤として用いる電解溶解法により、種々のPuO_2含有率となるよう機械混合したMOX粉末を溶解した結果、PuO_2の溶解速度に及ぼすUO_2の影響について、溶解初期においては、UO_2の溶解に伴い発生するNO_XガスによりAg^{2+}が還元されるためにPuO_2の溶解は進行せず、また、UO_2の溶解による遊離酸濃度の低下によりAg^{2+}の生成速度が遅くなるためにPuO_2の溶解速度が遅くなることが明らかになった。

5. 参考文献

(※) 木原義之，都所昭雄，他“電解溶解技術開発”動燃技報，No.89 (1994).

(1) C.Madic, M.Lecomte, et al., “Mechanism of the Rapid Dissolution of PuO_2 under Oxidizing Conditions, and Applications.” RECOD’91, Proceedings Vol. 2, 715 (1991).

(2) J.L.Ryan, L.A.Bray, “Actinide Separations.” ACS Symp. Ser. 117, 499 (1980).

(3) O.K.Tallent, J.C.Mailen, “Study of the Dissolution of Refractory PuO_2 in Nitric-Hydrofluoric Acid Dissolvents at 100 ℃.” Nucl. Technol., 32, 167 (1977).

(4) 桜井　聡，館盛勝一，他，“電解酸化法による二酸化プルトニウムの溶解（Ｉ），溶解条件の検討とスケールアップ予備試験，”日本原子力学会誌，31 (11), 1243 (1989).

(5) Mrs. A.M.Shakila, T.G.Srinivasan, et al., “Dissolution of PuO_2 in HNO_3-HF-N_2H_4 Medium.” Nucl. Technol., 79, 116 (1987).

(6) J.Bourges, C.Madic, et al., “Dissolution du Bioxyde Plutonium en Milieu Nitrique per L'argent (II) Electrogenere”, CEA-CONF-8280 (1985).

(7) F.M.Scheitlin, W.D.Bond, “Recovery of Plutonium from HEPA Filters by Ce (IV)-Promoted Dissolution of PuO_2 and Recycle of the Cerium Promoter,” ORNL/TM-6802 (1980).

(8) 桜井　聡，館盛勝一，他，“電解酸化法による二酸化プルトニウムの溶解（II），スケールアップ実験と精製法，”日本原子力学会誌35 (2), 147 (1993).

(9) G.W.C.Milner, A.J.Wood, AERE-R4975 (1965).

(10) K.Motojima, K.Izawa, Anal. Chem, 36, 733 (1964).

(11) T.Sakurai, A.Takahashi, et al., “The Composition of NO_X Generated in the Dissolution of Uranium Dioxide,” Nucl. Technol., 83,24 (1988).

6. 不溶性タンニンによる放射性廃液中の微量プルトニウムの吸着挙動 (※)

根本　剛*，沼田浩二*，根本康弘**，都所昭雄*
*転換技術開発室　Conversion and Chemical Process Development Section
**原子力技術　Nuclear Engineering Company

Adsorption behavior of the trace amounts of plutonium in radioactive waste solution by insoluble tannin

T.Nemoto*, K.Numata*, Y.Nemoto** and A.Todokoro*

ABSTRACT

The adsorption behavior of the trace amounts of plutonium from radioactive waste solution by insoluble tannin in the form of additional condensed resin was investigated to be as follows.

1) Pu^{4+} was effectively and quickly adsorped on insoluble tannin at pH 3.0～10.0 from radioactive aqueous solution.
2) The maximun adsorption capacity of plutonium was 0.175gPu/g dry adsorbent.
3) The adsorption isotherms were found to be fitted by Frendlich type equation in the investigated concentarated ranges.

1. 緒　言

MOX燃料製造施設であるプルトニウム燃料第一、第二及び第三開発室から発生する硝酸プルトニウム／ウラニルを含む工程廃液及び分析廃液は、プルトニウム燃料第二開発室の湿式回収室(A/F104)に設置してあるプルトニウム廃液処理設備に受入れ、必要に応じて中和ろ過後、鉄共沈・活性炭吸着・キレート樹脂吸着処理を行い、放射性核種を除去している。

これらの処理に伴う中和沈澱物、スラリーなどの二次的副生物の発生は避けられず、本設備の焙焼工程で加熱焙焼処理により減容し酸化物としたのち、放射性固体廃棄物として貯蔵している。しかし、今後これらの副生物の保管・最終処理をどうするかが大きな課題になっている。したがって、原子力界の大きな目標である「廃棄物発生量の低減化」の観点から、副生物の発生しないあるいは発生しても処理が容易な新しい廃液処理プロセスの開発が望まれている。

著者らは、不溶性タンニン（以下吸着剤と記す）(1)がTRU元素、重金属などに対して高い吸着性を有すること(2),(3)、この吸着剤は植物中のタンニンを原料としたC、H、Oの元素から構成されているため、焼却減容が可能であり、副生物発生量の低減化につながることに着目した。

しかし、核燃料製造工程から発生する廃液中のウラン、プルトニウムのうち、ウラン吸着時の吸着速度、吸着量などの吸着特性については、ある程度データが揃っているが(3)、プルトニウムに関するデータはカラム試験で得られた濃度変化のみであり、プロセスへの適用性を検討する上で不十分である。例えば、プルトニウムはどのような吸着挙動を示すのか、またα線放射能濃度が現在の放出基準値よりさらに一桁程度まで除去可能かなど実験を通じてデータを蓄積する必要がある。プルトニウムを含む放射性廃液処理への適用性の検討に必要なデータを得るため、第一段階として基礎試験を実施した。

本報では、微量のプルトニウムを含む溶液を用い、吸着剤の除去率に及ぼすpHの影響、単位重量あたりの吸着量、吸着挙動などについて、基礎的特性を得るためのバッチ法による実験と実廃液処理に適用することを考慮しカラム法による実験を行い、主としてバッチ実験を中心に、その実験結果の一部について報告する。

2. 不溶性タンニンと吸着特性

ウラン吸着剤は、ウラン含有廃液の処理、海水からのウラン回収などの目的でこれまでに多くの吸着剤が開発されている(4)~(8)。それらのうち、有機系吸着剤の一つとしてタンニン系吸着剤があり、吸着性能の改良がなされている。

今回使用した吸着剤(1)は、縮合型タンニン粉末をアンモニア水に溶解し、アルデヒド水溶液を混合してゲル状組成物を生成し、この組成物を室温または加熱熟成して得られたもので、水、酸またはアルカリのいずれに対しても不溶である。従来のタンニン系吸着剤(8)は、微粒子の凝集物であるため、充填カラムに通液している間に、凝集形態が変化し、カラムの圧損が増大するという欠点があった。本吸着剤は微粒子をゲル状にすることにより、通液性を改良したものである。

このゲル状吸着剤は、TRU元素の他、クロム、水銀、鉛、鉄、コバルトなどの金属成分をよく吸着する。これはFig. 1に示すようにポリフェノール性水酸基が官能基となって金属元素とキレート化合物を形成するためと考えられる。また、ゲル状にすることにより上記官能基が金属元素と配位し易い立体構造になり、かつ極めて強い親水性物質であるため、優れた吸着性能を示すものと考えられる。

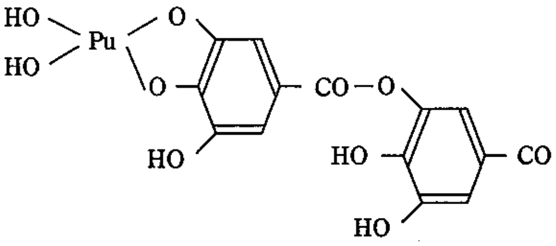

$Pu(OH)_4 \rightarrow Pu^{4+} + 4OH^-$

Fig. 1 Chemical structure of Pu^{4+}-adsorbent

3. 実験方法

3.1 不溶性タンニンの調整

通常、この吸着剤は湿った状態で、pH2の酸性水溶液（約$0.1N-HNO_3$）中に密封保管している。このままの状態で使用するとやや酸性領域であるため、吸着性能に影響を及ぼす恐れが懸念されるので、本実験では吸着剤を純水で洗浄しpH6～pH8にして使用した。また、カラム法による実験では吸着剤を充填したカラムにバッチ法と同様に純水を通液し、pHを中性領域に調整した。なお、本実験においては全て1.0～2.4mmに細分化した吸着剤を使用した。

3.2 試験液

実験に供した試験液は、プルトニウム溶液と実廃液の2種類であり、下記の通り調整した。

1）プルトニウム溶液

硝酸プルトニウム溶液をFig. 2に示すフローにより精製し、本試験液とした。なお、ほぼ中性領域の試験液のα線放射能濃度は約10^4～10^5Bq/mlである。

2）実廃液

プルトニウム廃液を鉄共沈処理したのち、廃液をろ紙（東洋濾紙No.5B）でろ過し試験液とした。なお、α線放射能濃度は前項のプルトニウム溶液と同様に約10^4～10^5Bq/mlである。

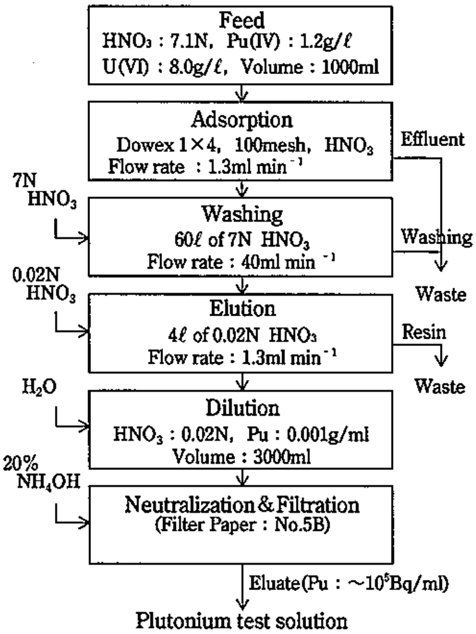

Fig. 2 Flow Sheet for the preparation of plutonyl nitrate test solution from mix solution of plutonyl and uranyl nitrate

3.3 バッチ法によるプルトニウム吸着試験

十分洗浄した一定量の吸着剤をビーカに入れ、さらに所定のpHに調整した一定量の試験液を加え、室温でマグネチックスターラで所定時間撹拌した。その後ろ紙（東洋濾紙No.5B）で吸着剤を分離除去し、ろ液中のプルトニウム濃度をα線放射能濃度から求めた。

吸着剤の吸着量及び吸着率は次式により求めた。

$$n = V(C_0 - C)/m \quad \cdots\cdots\cdots\cdots\cdots\cdots \quad (1)$$

$$p = (C_0 - C)/C_0 \times 100 \quad \cdots\cdots\cdots\cdots\cdots\cdots \quad (2)$$

ここで、nは吸着量(Bq/g - adsorbent)、pは除去率(%)、mは吸着剤量(g)、Vは試験液の容量(ml)、C_0及びCはそれぞれ実験開始前及び平衡到達後のα線放射能濃度である。なお、吸着量はすべて湿潤重量の値を基準に求めた。

3.4 カラム法によるプルトニウム吸着試験

バッチ法と同様に細分化した吸着剤を内径5mmφまたは10mmφのカラムに所定の長さに充填した。充填したのち、カラム内充填剤量の約10倍量の純水をゆっくり通液し、pHを中性領域に調整するとともに、カラム内の気泡を除去した。

実験は試験液のpH、α線放射能濃度、線速度(LV)、カラム長さをパラメータに通液し、一定時間毎にカラム通液後の溶液中のα線放射能濃度を測定した。

3.5　α線放射能濃度の測定

試料皿（SUS製直径50mmϕ）に試料を正確に1ml～5ml入れ、ホットプレート上で蒸発乾固し空冷したのち、α線計測装置で1min～5min計測した。検出器の計数効率はあらかじめ標準試料で測定し求めた値を採用した。

4.　実験結果及び考察

4.1　バッチ法によるプルトニウム吸着実験

4.1.1　プルトニウム吸着時の経時変化

プルトニウム溶液50ml中に吸着剤をそれぞれ1g（乾燥重量0.2g）と10g（乾燥重量2.0g）添加し、プルトニウム吸着量の経時変化を調べた。なお、プルトニウム溶液中のα線放射能濃度は7.77×10^3Bq/ml (2.31×10^{-5}mgPu/ml)、pHは7.1であった。

Fig. 3に示すように、吸着剤添加量によりプルトニウムの平衡吸着濃度は変化するが、吸着時間はいずれも5分から10分で平衡に到達した。なお、1時間後におけるプルトニウムの除去率はいずれも約98.5%でっあた。

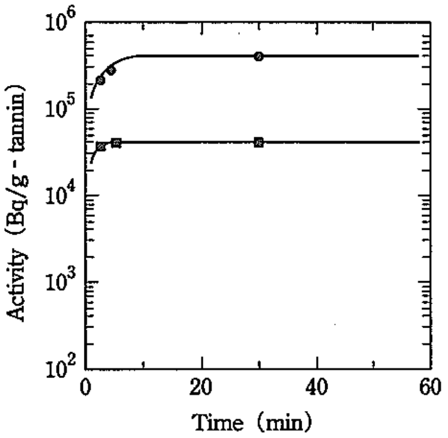

Activity : 7.77×10^3Bq/ml pH＝7.1
Volume : 60 ml
Adsorbent weight : ▨ 10g
● 1g
Mixing time : 60 min

Fig. 3　Time course of adsorption from plutonium solution by adsorbent

4.1.2　プルトニウム吸着量と吸着剤量との関係

つぎに、吸着剤の単位重量あたりの吸着量及び除去率が吸着剤の添加量によってどのように変化するかを調べた。すなわち、α線放射能濃度が3.86×10^5Bq/mlの溶液60ml中に吸着剤をそれぞれ1、5及び10g添加し、4.1.1の実験と同じ条件で1時間接触させた。

その結果、Fig. 4に示すように吸着剤量が増加するにつれて、吸着剤の単位重量あたりのプルトニウム吸着量は減少する傾向が認められた。また、吸着剤の増加に伴って吸着率はわずかに減少する傾向を示したが、いずれも98%以上であった。なお、プルトニウムの最大吸着量は、吸着剤（乾燥状態）1gあたり0.175gPuでありウランの0.208gUとほぼ同じ値を示した。

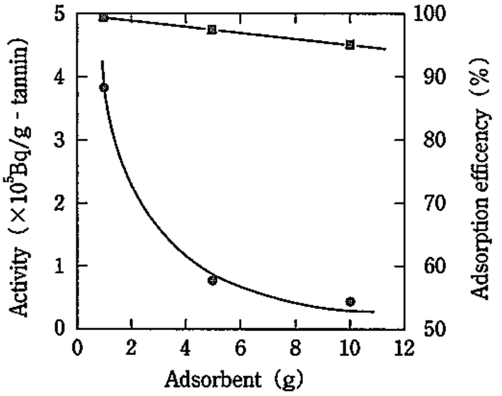

Activity : 3.86×10^5Bq／ml pH＝7.1
Volume : 60 ml
Mixing time : 60 min
● Activity
▨ Adsorption

Fig. 4　Relation between the amount of adsorbent and adsorption efficency by adsorbent

4.1.3　プルトニウム吸着とpHとの関係

吸着剤によるプルトニウムの吸着量が溶液のpHによってどのように変化するかについて、吸着剤量0.1g～5gの範囲でpHを4、5、6、7、8、9及び10の7段階に変化させて、プルトニウム溶液（α線放射能濃度6.40×10^2Bq/ml）60mlと1時間撹拌し、プルトニウムの吸着量を調べた。なお、pHの調整は硝酸あるいはアンモニア水を用いた。

その結果、Fig. 5に示すように、プルトニウムの吸着量は、pHは4～10の範囲ではいずれもほとんど変化なく、ほぼ100%吸着された。一般に、吸着剤は強酸性溶液ではpHの低下とともに溶液中のH^+イオンが増加し、H^+が優先して吸着剤に吸着する。一方、pHが高くなるとNH_4^+イオンの増加とともにNH_4^+が吸着するため、除去率が低下するといわれている(11)。今回のプルトニウムの場合はウランの場合(3)と同様にあまりその影響を受けず、かなり高範囲のpHで使用できることがわかった。

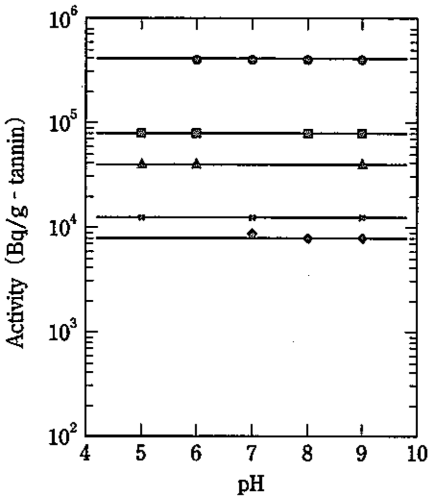

Activity　　: 640 Bq/ml
Volume　　: 60 ml
Mixing time : 60 min
Adsorbent : ● 0.1g, ▨ 0.5g, ▲ 1.0g
× 3.0g, ◆ 5.0g

Fig. 5　Effect of pH on the adsorption of plutonium by adsorbent

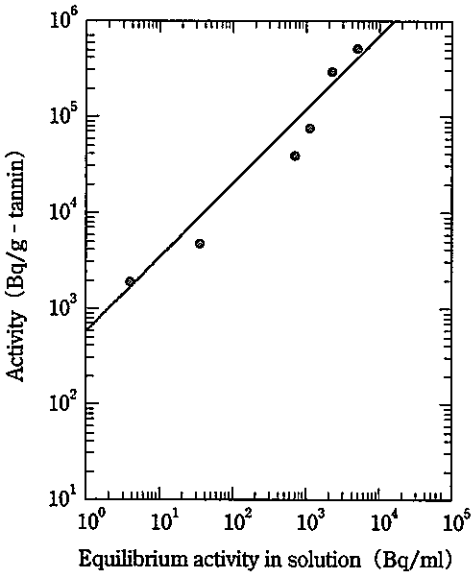

Volume　　　: 60 ml
Mixing Time : 60min

Fig. 6　Plutonium adsorption curve for adsobent

4.1.4 プルトニウム吸着量とプルトニウム溶液中のプルトニウム濃度との関係

プルトニウムの吸着量がプルトニウム濃度によってどのように変化するかを調べた。吸着剤1gに対してα線放射能濃度の異なる溶液を60mlと撹拌し、1時間後の吸着量を調べた。

室温下における吸着平衡後の平衡吸着量を吸着等温線で表すと、Fig. 6のようになる。一般に液相から固相への吸着現象は(3)式に示すようにFreundlih吸着等温式⁽¹¹⁾にしたがうといわれている。

Freundlich式：

$$q = kc^{1/n} \quad \cdots\cdots\cdots\cdots\cdots\cdots \quad (3)$$

$$\log q = \log k + 1/n \log c$$

ここで、q：吸着剤1gあたりの吸着物質の量 (Bq/g)
c：吸着平衡時の溶液中の吸着物質の濃度 (Bq/ml)
k, 1/n：任意のパラメーター

このFreundlich式のkの値が大きいほど吸着剤の吸着能が高く、1/nの値が0.5以下で吸着剤として実用性がある。特に、1/nの値が0.1～0.5の時吸着が良好に起こり、2より大きいと吸着が起こりにくいといわれている。今回使用した吸着剤では、1/nは0.78以下であり、またkは0.20である。なお、α線放射能濃度が10^0～10^{-1}Bq/ml以下の極低濃度においてもこのFreundlich式が適用できるかどうか確認する必要がある。

4.1.5 実廃液からのプルトニウム吸着予察実験

鉄共沈処理後の上澄液（実廃液）を使用し、吸着剤量を変えて実験を行った。その結果をFig. 7に示す。

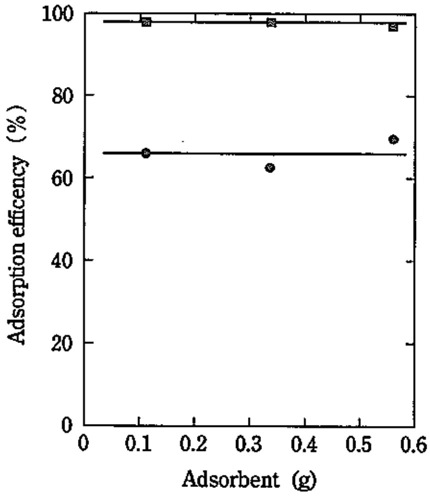

Activity　　: ▨ 640Bq/ml
● 72Bq/ml
Volume　　: 60 ml
Mixing Time : 120 min

Fig. 7　Relation between the amount of adsorbent and adsorption efficency by adsorbent

実廃液でのプルトニウム除去率は、吸着剤量を変えてもいずれも約65%であり、不純物を含まないプルトニウム溶液での99%に比べて約30%も低下している。

この吸着剤はアルカリ金属やアルカリ土類金属を吸着

しない性質があり、溶液中にNa^+、Mg^+イオンを含む場合でもウランやプルトニウムを選択的に吸着する(3)(4)。一方、遷移元素であるFe^{3+}イオンなどに対する吸着が高いという性質があるため、鉄共沈処理後の溶液中に含まれるFe^{3+}イオンの吸着の影響を受けプルトニウムの吸着率が低下したものと考える。

4.2 カラム法によるプルトニウム吸着実験

4.2.1 プルトニウム吸着特性への線速度の影響

カラム法による実廃液からプルトニウムの除去を想定し、通液速度及びプルトニウム濃度の吸着に及ぼす影響を調べた。

内径5mmφ、長さ50mmのカラムに吸着剤1gを充填し、線速度を0.5cm/hr〜1.2cm/hrの線速度（SV=5〜40の空間速度）で、α線放射能濃度を変えた溶液をカラムに通液し、流出液中のα線放射能濃度を測定した。その結果をFig. 8に示す。

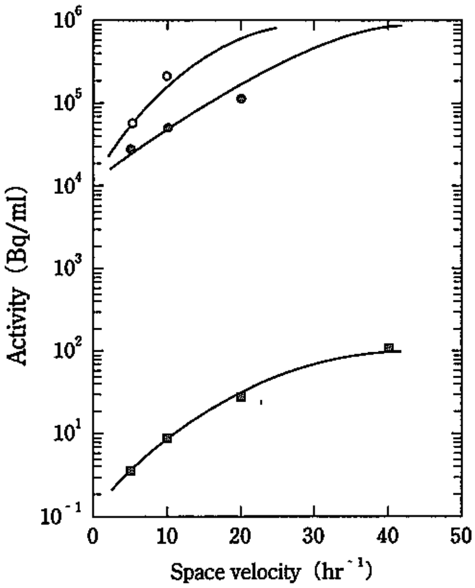

Bed Volume　　　: 1 cm^3(5mmφ×50mmt)
Adsorbent weight　: 1 g　(Dry weight 0.2g)
Activity :　■ 1.92×10^3 Bq/ml PH=8.2
　　　　　● 1.53×10^5Bq/ml PH=4.5
　　　　　○ 1.53×10^5Bq/ml PH=3.0

Fig. 8　Effect of spece velocity and activity on adsorption of plutonium by column test

流出液中のα線放射能濃度は、通液する溶液中のα線放射能濃度により変化し、濃度に比例して上昇する。

また、線速度の上昇に伴って流出液中のα線放射能濃度が増加する傾向を示した。さらに、低濃度と高濃度プルトニウム溶液を比較した結果、Table 1に示すように低濃度の方が除去率が大きく、流出液中のα線放射能濃度を低く処理できる。したがって、実際にカラム法によりα線放射性核種を除去する場合は、設備の処理能力、処理液量、処理後のα線放射能濃度などを考慮する必要があるが、特に流出液中のα線放射能濃度は線速度に大きく影響されるため、可能なかぎり線速度の遅い供給条件、すなわち低流速で通液することが望ましい。

なお、線速度と流出液中のα線放射能濃度，破過点などについては、今後実施する計画である。

Table. 1　Effect of LV on adsorption of plutoium by column test

pH	Activity (Bq/ml)	Flow rate (ml/min)	LV* (cm/min)	Absorption efficiency (%)
3.0	640	0.09	0.46	96.1
		0.18	0.92	85.7
		0.36	1.84	63.4
		0.72	3.68	50.7
4.5	72	0.09	0.46	98.9
		0.18	0.92	96.7
		0.36	1.84	92.3
		0.72	3.68	82.5

*LV : Liner velocity

4.2.2 連続通液時のプルトニウム吸着特性

一例としてpH8.2に調整した1.92×10^3Bq/ml のα線放射能濃度の溶液をカラムに通液し、流出液中の濃度を測定しその漏出濃度を調べた。その結果、Fig. 9に示すように線速度が1.99cm/minと速いため、流出液中のα線放射能濃度は2〜3Bq/mlになった。

一方、カラム中の吸着剤1glあたり約1000倍量以上通液したが、流出液中のα線放射能濃度はほとんど変化がなく処理できることが分かった。

5.　結　論

プルトニウム取扱い設備から発生する放射性廃液中に含まれる極微量のα線放射性核種（主としてプルトニウム）を除去するための吸着剤として、不溶性タンニンについて吸着特性を中心に基礎的な実験を行った結果、次のような結論が得られた。

(1)　通常、吸着剤の吸着性能は処理対象液のpHに依存するが、本吸着剤のpHは4〜10と広い範囲でプルトニウムを効率的に、しかも短時間で吸着することが可能である。

(2)　吸着剤1g（乾燥重量0.2g）あたりのプルトニウムの飽和吸着量は約0.175gであり、ウランの0.208gとほぼ同じ吸着容量を示す。

(3)　溶液中のα線放射能濃度が10^5〜10^0Bq/mlの範囲での吸着はFreundlich式により整理できる。しかし、処理後の最終的のα線放射能濃度として、現在10^{-3}Bq/mlを目標にしており、今後極低濃度領域での挙動を実験を通して確認する必要がある。

(4)　カラム法で処理する場合は、吸着時の流出液の

濃度を考慮し、通液速度、カラム長さ、処理液濃度などにより最適条件を設定する必要がある。

終わりに、本実験を行うにあたり、試料の放射能濃度測定に協力して頂いた原子力技術株式会社の関係者に対し感謝いたします。また、貴重な吸着剤の提供と有意義な助言を頂いた三菱原子燃料株式会社　亀井義信氏に深く感謝の意を表します。

参考文献

(※) 沼田浩二，他，“ノンスラッジ廃液処理プロセスの開発（Ⅱ）ーカラム式不溶性タンニンによるPu吸着挙動ー”，日本原子力学会「1994年春の年会」予稿集，A7，1994.

(1) 三菱原子燃料㈱，“不溶性タンニンのウラン・重金属吸着剤”，新金属工業，№348，29，(1992).

(2) 亀井義信，他，“不溶性タンニンによるウラン含有廃液処理”，日本原子力学会「1992年春の年会」予稿集，C28，1992.

(3) 亀井信義，他，“不溶性タンニンによる　TRU含有廃液処理”，日本日本原子力学会「1992年春の年会」予稿集，C29，1992.

(4) 坂口孝司，“生物体や生体物質を利用するウラン資源の回収”，月刊海洋科学，Vol.15，№11，p.681，1983.

(5) 坂口孝司，“ウランの生体濃縮”，Isotope news，№6，p.2　1979.

(6) 坂口孝司，他，“多糖キサンドゲン酸チタン（Ⅳ）塩による海水ウランの回収”，日化，№6，p.787，1979.

(7) 堀　隆博，“アミドオキシム型キレート樹脂の海水ウラン吸着平衡特性1”，化学工学論文集，Vol.13，№6，p.795　1987.

(8) 特許　特開平　5−66291，H3.12.12
“金属元素吸着剤の製造方法及び該吸着剤による金属元素の吸着分離方法”.

(9) 特許　特開平　5−50058，H3.8.23
“タンニン系吸着剤による重金属類の吸着分離方法及び該吸着剤の再生方法”.

(10) 南澤宏明，他，“化学処理した天然ゼオライトにおける鉛（Ⅱ）の吸着特性”，日化，№12，p.1605，1979.

(11) 慶伊富長，“吸着：共立全書157”，共立出版　1976.

7. Selective Excitation of a Branched Vibrational Ladder in the Uranium Hexafluoride Laser Isotope Separation (※)

M.Suzuki, Y.Miyamoto, M.Hasegawa and Y.Shimazaki
Enrichment Technology Development Section

ABSTRACT

Theoretical investigation was made on the dynamics of initial excitation process in molecular laser isotope separation for uranium hexafluoride(UF_6) based on the generalized N-level density-matrix equation derived by Goodman, et al. Branched vibrational model due to anharmonic-splitting components for the ν_3 mode of UF_6 molecule were formalized and phase interferences of density-matrix elements were considered to analyze the selective excitation. Because of a power-broadening effect, no more than 0.05J/cm^2 fluence of a laser pulse completely masks high enrichment peaks in broadband ($\Delta\nu$ = 2GHz) pumping case. Even when matching the laser frequency with ν_3 band ($n = 0 \rightarrow 1$) of $^{238}UF_6$, the enrichment factor ($\alpha \equiv R_{product} / R_{feed}$, $R \equiv [^{235}UF_6]/[^{238}UF_6]$; R is the abundance ratio and [ ] means the mole fraction.) dese not decrease. A narrow spectral linewidth ($\Delta\nu$ = 400MHz) is shown to be essential to achieve a high concentration ratio in the system with a branched N-level ladder as expected from a general two-level system. The exciting frequency, which does not necessarily accord with the ν_3 band of $^{235}UF_6$, gives the maximum enrichment peak. Both the detuning of the optimum frequency and the sharp enrichment peak suggest a direct excitation due to multiphoton resonance. Spectral stability of the laser pulse is also required to excite only the desired isotope for the system with complicated anharmonic-splittings.

1. INTRODUCTION

In the IRMPD(Infrared Multiple Photon Dissociation) of uranium hexafluoride(UF_6) isotope separation, we have to excite the isotope $^{235}UF_6$ in a discrete level region. A scheme using two infrared laser pulses has been experimantally demonstrated(1)(2). One is tuned at a fundamental vibrational frequency and does not have enough fluence to dissociate the excited molecules. The other is sufficiently detuned from the fundamental frequency but has an appropriate frequency and enough fluence to excite the molecules through a quasicontinuum to dissociation. Because of a small isotope shift of the polyatomic molecule the first laser source should be satisfactorily monochromatic and tunable for highly selective excitation of the desired isotope. Since a TEA(Transversely Excited Atmospheric) CO_2 laser provides only discrete frequencies corresponding to the rotational lines of CO_2 molecule, a TEMA(Transversely Excited Multi-Atmospheric) CO_2 laser has been developed in order to obtain continuous tunability(3).

Making use of pressure broadening of the individual rotational line to increase the laser gain in the midst of the two adjacent lines simultaneously decreases monochromaticity which is important for isotope separation in the usual sense. Precise control of spectral characteristics of the laser pulse seems to be necessary in the complicated vibrational levels of UF_6 molecules. Particularly, the tunable 16μm laser pulses have been successfully generated only through a four-wave mixing process with the TEMA CO_2 laser pulse in a multiple-pass Raman cell(4)(5), so that an appropriare energy of the TEMA pulse is required for long propagation and nonlinear conversion. Some techniques for SLM(Single Longitudinal Mode) operation of the TEMA CO_2 laser have been reported using near threshold oscillation (6), however, a competitive relation between the spectral narrowing and enough energy extraction per pulse has limited the usefulness of the TEMA laser.

When a laser fluence is increased, a power broadening estimated by a known magnitude of ν_3 vibrational dipole moment of the molecule UF_6 becomes comparable to the Q-branch linewidth(7). This means that a coherent Rabi oscillation period comes to be as short as an oscillator decay time due to the inhomogeneously broadened medium. The highly degenerated levels make the dephasing time small, because the density of vibrational stated is 10^4 cm at vibrational energy 3×10^3 cm^{-1} in the molecule(8). Nevertheless, a detail phase relationship between the polarization of the absorbing molecule and the light field in the initial excitation stage is expected to influence selectivity until the relaxation sufficiently alters the system behavior to mask any coherent phenomena. In order to clarify an effect of the fluence and the frequency stability on the enrichment factor ($\alpha \equiv R_{product} / R_{feed}$, $R \equiv [^{235}UF_6]/[^{238}UF_6]$; R is the abundance ratio and [ ] means the mole fraction.), an amount of detuning and a Rabi frequency should be carefully examined. Therefore, the time-dependent Schrödinger equation is adopted to analyze the dynamics of the N-level excitation process. In addition to the general vibrational ladder the molecule UF_6 has the anharmonic-splitting components on individual vibrational level, so that various excitation channels via the splitting components interfere with the coherent excitation each other.

The selection rule for dipole transition between successive levels complicates this problem(8). The branched N-level ladder model composed of detunings of the splitting components is developed for the calculations to investigate the spectral dependency of the enrichment factor in coherent pumping.

2. BASIC EQUATIONS

The coherent dynamics of a two-level system absorbing light from a monochromatic source has been discussed using the OBE(Optical Bloch Equation)(9). For a molecule undergoing thermalizing collisions with a reservoir, both the population decay time(T_1) and the phase relaxation time(T_2) describe the collisional randomization with the Markoff approximation(10). In this study density-matrix equations are used to investigate the population dynamics of UF_6 molecules in the branched N-level ladder. The time evolution of the density matrix equation is given by(11)(12)

$$\frac{d\rho}{dt} = \frac{i}{\hbar}[\rho,H] + \left(\frac{1}{t}K\rho - \frac{1}{t}\rho\right) - \frac{1}{\hbar}\sum_{n=0}^{N-1}\Gamma_n(\rho P_n + P_n\rho). \tag{1}$$

In this equation ρ and H are the density matrix and the harmonic Hamiltonian, respectively. The second term in the right-hand side accounts for the phase relaxation, $\tau^{-1}K\rho$, and the population decay,$\tau^{-1}\rho$. The third term represents the effect of irreversible decay such as intramolecular relaxations into the high density background modes. $\Gamma_n/\hbar$ is this decay constant from the nth vibrational state and P_n is the projection operator. An N-level vibrational ladder model in the presence of collisional perturbations with a heat bath of inert molecules and irreversible relaxation to the background modes is schematically represented in Fig. 1. By assuming the harmonic Hamiltonian the solution of the density-matrix element is written as follows:

$$\rho_{nm} = C_{nm}e^{i(m-n)xt}e^{-\lambda t} \tag{2}$$

where χ is the driving laser frequency. C_{nm} and λ is the complex eigenvector components and the eigenvalue, respectively. Substituting this form of solution into Eq. (1) and using the RWA(Rotating Wave Approximation), one finds the equations of nondiagonal and diagonal matrix elements of the complex eigenvector.

$$-C_{nm}Q_{nm}(\lambda) + \beta_m C_{nm-1} - \beta_{m+1}C_{nm+1} + \beta_n C_{n-1m} - \beta_{n+1}C_{n+1m} = 0, \quad n \neq m \tag{3}$$

$$\lambda C_{nn} - \left(\frac{2\Gamma_n}{\hbar}\right)C_{nn} + \beta_n C_{nn-1} - \beta_{n+1}C_{nn+1} + \beta_n C_{n-1n} - \beta_{n+1}C_{n+1n} = 0, \tag{4}$$

where Q_{nm} is given by

$$Q_{nm}(\lambda) = \frac{1}{\tau} + \frac{(\Gamma_n + \Gamma_m)}{\hbar} - \lambda + i\sum_l\sum_k(x - \omega_{nl,mk}). \tag{5}$$

Since the lifetime of the vibrational level is relatively long, the T_1−type relaxation term is neglected in Eq.(4). The Rabi frequency β_n is given by $\beta_n = (\alpha_n E/2\hbar)$; α_n and E are the dipole moment for the n → n + 1 transition and the electric field strength, respectively. The dipole moment has been reported only for the first-step transition (n = 0 → 1)(7). For succesive transitions the dipole moments are assumed to be $\alpha_n = (n+1)^{-1/2}\alpha_0$(13)(14). The last term in the right-hand side of Eq.(5) represents the detuning contribution between the laser frequency and the individual energy level $\omega_{nl,mk}$. l and k represent the anharmonic-splitting components in the n and m vibrational level, respectively. With the summation of l and k, phase interference of the density matrix is considered in the n → m transition. The spherical-top-type molecule UF_6, which belongs to the symmetry O_h (octahedron), has high degeneracies of the vibrational states.(8) These degeneracies are partially removed to form anharmonic-splitting components that are related to different values of vibrational angular momentum. The split energy levels for ν_3 mode of the UF_6 molecule with vibrational quantum number from 0 to 4 are shown in Fig. 2. Forbidden transitions due to the selection rule are indicated by the dotted lines. Spectroscopic data of the Q-branch of the ν_3 overtone of UF_6 have been discussed in many papers(14)(15), and we adopt the most recently published data of $^{238}UF_6$ energy levels listed in Table. 1.(16)

For the N-level vibrational system, the matrix equations describe a set of N^2 coupled eigenvalue-eigenvector problems, and are solved using a standard matrix-diagonalization package. From N particular eigenvalues the general solution of the diagonal element can be written as follows :

$$\rho_{jj}(t) = \sum_{ij}^{N} \alpha_j C_{ij} e^{-\lambda_j t} \qquad (6)$$

The N coefficients α_j are introduced to match the general solution to an arbitrary population at time t = 0.

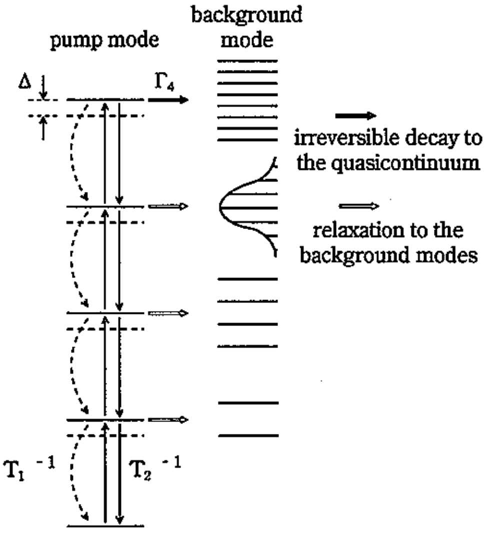

Fig. 1
Schematic representation of a calculation model for the vibrational ladder. T_1 and T_2 are the population decay time and the phase relaxation time, respectively. Γ_4 indicates the irreversible transfer rate to the quasicontinuum from the n=4 level. Δ represents the detuning.

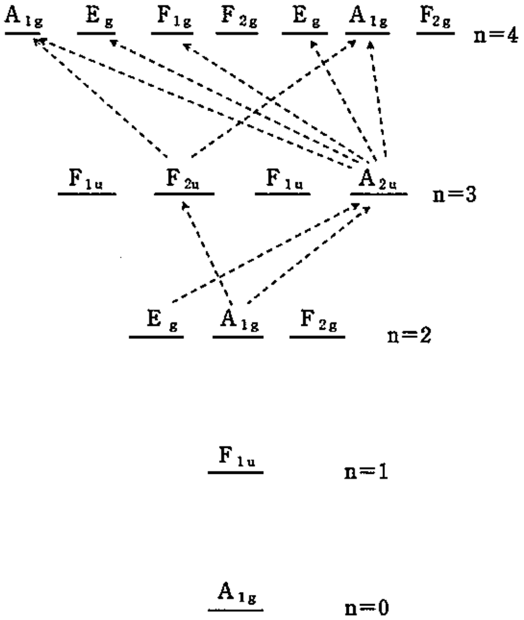

Fig. 2
Branched N-level model of anharmonic-splitting components for the ν_3-mode of the molecule UF_6. Splittings of states of vibrational quantum number n from 0 to 4 are shown with the symmetry symbols. The dipole-forbidden transitions due to the selection rule are shown in the dotted lines.

		$^{235}UF_6$	$^{238}UF_6$
n=1	F_{1u}	628.31	627.72
n=2	E_g	1253.94	1252.84
	A_{1g}	1254.19	1253.09
	F_{2g}	1256.76	1255.66
n=3	F_{1u}	1877.20	1875.60
	F_{2u}	1882.58	1880.98
	F_{1u}	1882.86	1881.16
	A_{2u}	1885.50	1883.80
n=4	A_{1g}	2497.95	2495.75
	E_g	2497.96	2495.76
	F_{1g}	2505.93	2503.73
	F_{2g}	2506.30	2504.20
	E_g	2508.80	2506.60
	A_{1g}	2509.07	2506.87
	F_{2g}	2511.62	2509.42
		estimated	

(cm^{-1})

Table. 1
Energy levels of anharmonic-splitting components in the $n\nu_3$ overtone of UF_6. The levels of $^{238}UF_6$ are quoted from the reference (16) and those of $^{235}UF_6$ are estimated by adjusting the anharmonic constant to match the reported n=0 → 1 transition frequency. (14) (15)

3. RESULTS

The population of the individual vibrational level shows the oscillatory behavior which is characteristic of coherent excitation, and the effects of both the Rabi frequency and the detuning in the simplified N-level model are checked with the reference(17). Results of the product yield and the enrichment factor, which are calculated from the population $\rho_{55}(t)$ at the end the laser pulse, will be shown in this section.

3.1 Most Suitable Condition of the Laser Pulse

In order to investigate the optimum frequency for exciting the $^{235}UF_6$ molecule efficiently and the effect of power broadening on the enrichment factor, typical parameters are chosen for the calculations as follows. The pathway to the quasicontinuum is only from the uppermost level(n = 4) in the discrete region and the transition rate is assumed to be given by $\Gamma_4 = 10^{-2}(ns^{-1})$. Although we can consider an arbitary input pulse shape by changing the Rabi frequency and solving the eigenvalue equations successivly, we assume a square input pulse with 100 ns temporal width for the first approximation. The laser linewidth is given by $\Delta\nu$ = 2(GHz), and the phase relaxation time T_2 is assumed to be $T_2 = (2\pi\Delta\nu)^{-1}$. Excited molecules to the quasicontinuum are assumed to be dissociated unconditionally. The enrichment factor is obtained by the calculations for both the isotopes $^{235}UF_6$ and $^{238}UF_6$. The enrichment factor and the dissociation yield as a function of both the laser fluence and the frequency are shown respectively in Fig. 3(a) and Fig. 3(b). The frequency ranges from 626.5cm^{-1} to 628.9cm^{-1} corresponding to the CO_2 rotational line from 10R(28) to 10R(32) and the practical fluence range up to 0.45J/cm^2 are examined. It is understood in Fig. 3(b) that in accordance with the anharmonic red-shift the dissociation yield increases as the frequency goes away from the ν_3 fundamental 627.7cm^{-1} to the red side. With an increase of the laser fluence the yield increases gradually and a slight saturation is seen around the converted 10R(28) frequency. In Fig. 3(a), the sharp maxima of the enrichment factor are shown and more than 10 values of the factor are obtained at 628.7cm^{-1}. Nevertheless, the peaks are significantly reduced when increasing the fluence (>0.05J/cm^2) and detuning from the optimum frequency (>0.2cm^{-1}). This suggests that the power broadening due to the increase of intensity smears out the maxima and the optimum frequency is influenced by the complicated anharmonic levels. At 627.7cm^{-1} corresponding to the ν_3 fundamental of $^{238}UF_6$ molecule, any depletion of the factor is not seen.

3.2 Background Reservoir and Narrow-Band Pumping

For UF_6 molecules the overtone bands of other vibrational modes and the combination bands among them are possible to construct the background reservoir for the ν_3 mode. The case whose transition pathway from the discrete region to the quasicontinuum is extended to the lower vibrational levels is calculated. The interference from the background reservoir is assumed as the irreversible transfer to the quasicontinuum. Since the transfer probability due to collisional perturbation should be proportional to the background mode density, the transfer retes are given by $\Gamma_2 = 10^{-4}(ns^{-1})$ and $\Gamma_3 = 10^{-3}(ns^{-1})$. The change of the enrichment factor as a function of the frequency and the fluence is shown in Fig. 4(a). Although the collisional escape from the halfway point of the vibrational ladder has been thought not to affect the enrichment factor, the sharp peaks in Fig. 3(a) are completely gone. This means that irradiation of the laser pulse to the UF_6 molecule the cooling of vibrational temperature using a supersonic jet is useful because of not only the sharpening of the absorption spectrum but also the decreasing of the initial population of other vibrational modes.

The dephasing time T_2 destructs the coherent excitation buildup. The inhomogeneous spectrum of the ν_3 Q branch has a wide bandwidth to absorb all of the photons generated from the laser pump. In this case the time T_2 is determined by the linewidth of the laser. The linewidth $\Delta\nu$ = 400MHz is given in order to investigate the effect of the spectral narrowing on the enrichment factor. The transfer rate from the uppermost level is given by $\Gamma_4 = 10^{-2}(ns^{-1})$ and the pathways from level 2 and 3 are prohibitted to correspond to the case in Fig. 3. The detailed structure composed of peaks and valleys of the enrichment factor is shown according to the frequency change in Fig. 4(b). In addition to the same peaks shown in Fig. 3(a), one more peak is seen around 627.5cm^{-1}. Although the former peaks quickly decrease as fluence increases, the latter has a long tail in the fluence axis. This different behavior of the fluence dependency suggests that in the complicated energy level the coherent excitation analysis give us more detailed information than a simple power-broadening estimation. It should be noted that in the low fluence region (<0.05J/cm^2) the factor goes up and down according to the frequency change and the enrichment factor often decreases below a unity. This means that an excitation ratio of $^{238}UF_6$ exceeds that of $^{235}UF_6$. The pump laser likely depletes the enriched product without the mean frequency stability less than a few gigahertz(<0.1cm^{-1}).

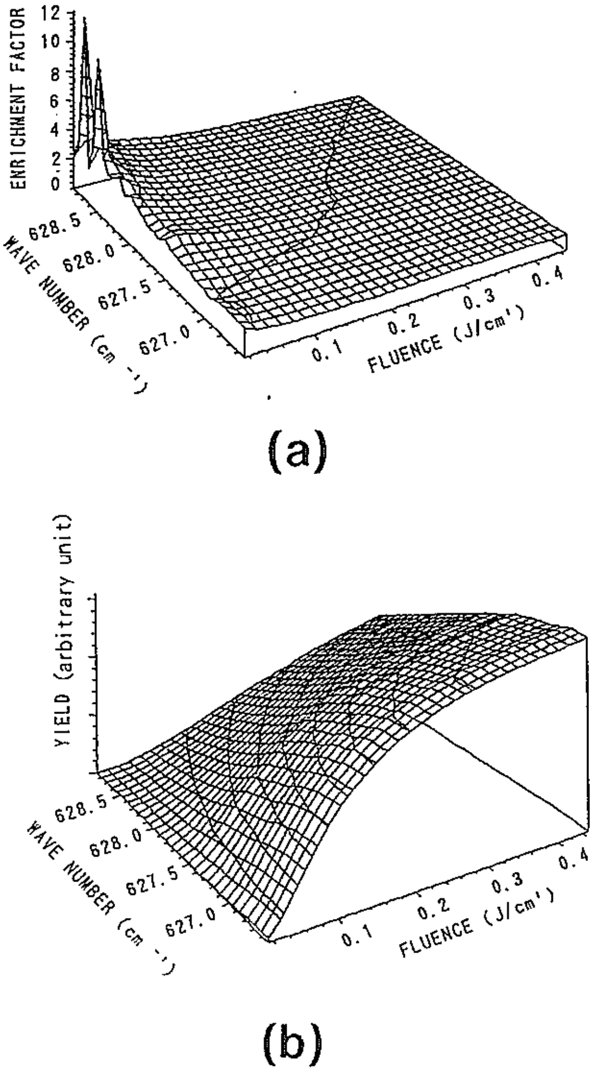

Fig. 3

(a) Enrichment factor as a function of both the laser frequency and the fluence. The frequency range around the $\nu_3(n=0\rightarrow1)$ transition (626.5~628.9cm^{-1}) and the practical fluence up to 0.45 (J/cm^2) are investigated. The irreversible transfer rate to the quasicontinuum is $\Gamma_4=10^{-2}$ (ns^{-1}), and the pumping laser linewidth is $\Delta\ \nu=2$ GHz.

(b) The product yeild of both $^{235}UF_6$ and $^{238}UF_6$.

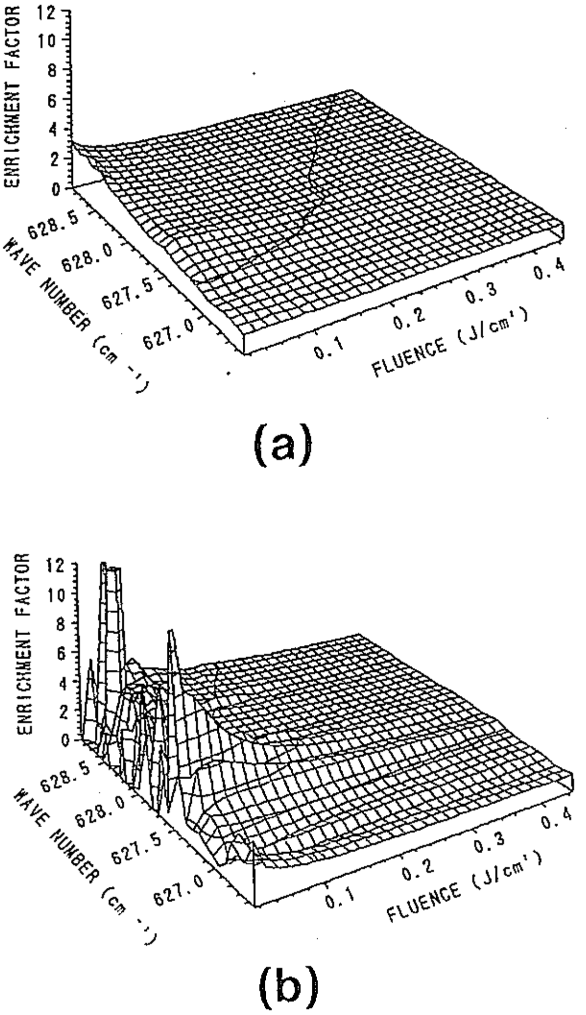

Fig. 4

(a) The effect of the irreversible decay from the intermediate levels in the pumped ladder to the background modes. The decay rates of the level 2 and 3 are given by $\Gamma_2=10^{-4}$ (ns^{-1}) and $\Gamma_3=10^{-3}$ (ns^{-1}), respectively. The change of the enrichment factor is shown as a function of both the laser frequency and the fluence.

(b) Instead of the broad linewidth ($\Delta\nu=2$ GHz) in Fig. 3, the narrow linewidth case ($\Delta\ \nu=400$ MHz) is investigated. The irreversible decay rates are set by $\Gamma_2=\Gamma_3=0$ and $\Gamma_4=10^{-2}$ (ns^{-1}), respectively.

4. DISCUSSION

An analytical solution of the coherent density matrix equation has been derived for a typical two-level model, but the analytical approach would be hopeless for the N-level vibrational model. Moreover, it is difficult to predict the dynamics of the excitation process in the N-level ladder involving anharmonic-splittings of the UF_6 molecule. An appropriate formula of the dynamics without an approximation is not obtained, however, we will argue about the unique features of the enrichment factor as shown in Fig. 4(a) and 4(b), respectively.

When the Rabi frequency β is small and the relaxation rate Γ is large, the coherent oscillation period of the population becomes large compared to the relaxation time. In this incoherent pumping case any phase information about the individual probability amplitude is not important. We can estimate the dynamics of the N-level excitation using a rate-equation approximation. The simplified form of the transition probability in a separate two-level is given as follows(9):

$$W \propto \frac{\beta^2(\Delta\nu + \Gamma)}{(\Delta\nu + \Gamma)^2 + \Delta\omega^2} \tag{7}$$

where $\Delta\nu$ is the linewidth of the pumping laser and Γ is the irreversible decay rate to the background modes. $\Delta\omega$ represents the detuning contribution associated with the frequency difference between the laser and the split energy levels. Including the saturation effect with the Rabi frequency in the denominator of the transition rate in Eq.(7), one finds the enrichment factor:

$$\alpha \propto \frac{(\Delta\nu + \Gamma)^2 + \beta^2 + \Delta\omega_{238}^2}{(\Delta\nu + \Gamma)^2 + \beta^2 + \Delta\omega_{235}^2} \tag{8}$$

where $\Delta\omega_{235}$ and $\Delta\omega_{238}$ are the detuning terms of $^{235}UF_6$ and $^{238}UF_6$ molecules, respectively. It is understood that increase of either the laser linewidth on the irreversible decay rate causes the enrichmant factor to become independent on the detuning term. As the power broadening increases, the factor becomes independent of the laser frequency change and the excitation results in a small selectivity. The smooth dependency accounting for relaxation to the background modes in Fig. 4(a) is understood by this inference. On the contrary, in the narrow linewidth case the enrichment factor becomes very sensitive to the frequency change, because, $\Delta\nu$ and β are small in Eq.(8). In this case the sharp peaks and valleys are not explained by the above approximation.

When the power broadening becomes small, the detuning between the first two-levels is not compensated by the broadening and the excitation to the upper level is difficult. However, it should be noted that N photons whose summed frequency compensates the accumulated detuning up to the N-level can be absorbed at once. In this multiphoton resonance case, without any relaxation a solution of the population dynamics is given as follows(8):

$$\rho_{NN}(t) \simeq \sin^2[\beta^{(N)}t] \tag{9}$$

$$\beta^{(N)} = \frac{\beta_1\beta_2\cdots\beta_N}{(x-\omega_{21})(2x-\omega_{21}-\omega_{32})\cdots\{(N-1)x-\omega_{21}-\omega_{32}-\cdots-\omega_{NN-1}\}}$$

where $\beta^{(N)}$ is the multiphoton Rabi frequency. The multiphoton power broadening is defined by

$$(\Delta\Omega)^{(N)} = \frac{2\beta^{(N)}}{N} \tag{10}$$

Using Eq.(9), one finds the enrichment factor in the coherent and no-relaxation limit:

$$\alpha \propto \frac{\sin^2[\beta_{235}^{(5)}t]}{\sin^2[\beta_{238}^{(5)}t]} \tag{11}$$

The factor is calculated using Eq.(11) as a function of the laser frequency and is shown in Fig. 5. The multiphoton power broadening in Eq.(10) is much smaller than the two-level Rabi frequency, so that the absorption spectrum corresponding to this resonance becomes narrow. It is inferred that the sharp peaks and vflleys in Fig. 4(b) as well as in Fig. 5 result from both the narrow spectrum and the small isotope shift. From the fact that the enrichment factor sometimes decreases below a unity similarly in Fig. 4(b), we infer that the multiphoton resonance excitation of $^{238}UF_6$ with the complex anharmonic-splittings exceed that of $^{235}UF_6$. When the multiphoton power broadening exceeds the anharmonic detuning, the adjacent resonances become overlapped and the sharp peaks are smoothed out. This means that closely split anharmonic levels govern the behavior of the peaks in increasing the Rabi frequency. Therefore the different fluence dependency of the enrichment peaks in Fig. 4(b) is thought to correlate closely with the individual background of anharmonic-splittings.

Through a no-seed SRS(Stimulated Raman Scattering) process the 16μm photons are initiated by quantum noise which plays a dominant role in macroscopic fluctuations of the Stokes phase even in the pump-depleted region. The intrinsically quantum mechanical behavior has been shown to persist in the phase fluctuations(18). The Stokes pulse used in the IRMPD has a long duration time(50ns) compared to the depasing time(2ns). In this steady-state case($\Gamma\tau > 1$: Γ^{-1} is the dephasing time in the Raman medium and τ is the pulse width), the collisional damping causes the initial quantum fluctuation to decay exponentially in time. However, vacuum noise continuously reintroduces fluctuation in the Stokes field during propagation(19). Specifically, in the broadband pumping using the TEMA-CO_2 laser the noisy Stokes spectrum is an important subject, because the Raman generator possibly deteriorates the spectral stability as a finite-bandwidth noise amplifier.

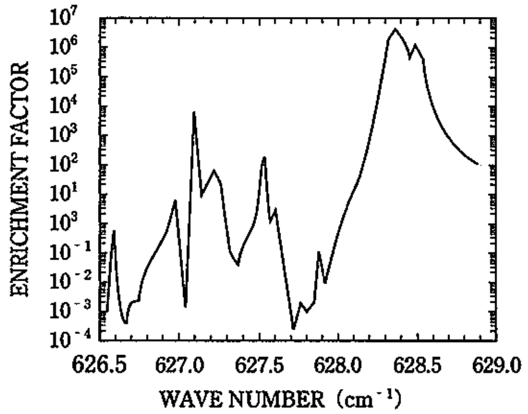

Fig. 5
In the coherent and no-relaxation limit the effect of multiphoton resonance on the enrichment factor is shown as a function of the laser frequency. The energy levels of anharmonic-splitting in Table. 1 are used and the laser fluence is given by ϕ=0.01 (J/cm^2)

5. CONCLUSION

It is concluded that spectral bandwidth less than 2GHz of the continuously tunable CO_2 laser pulse is necessary to acheive a more than 10 emrichment factor in UF_6 vibrational excitation considering the anharmonic-splittings. In the broadband ($\Delta\nu$ = 2GHz) pumping case, the enrichment factor is not depleted less than 1 in the entire frequency (626.5~628.9cm^{-1}) the fluence (< 0.45J/cm^2) region. A slight increase in the laser fluence up to 0.05J/cm^2 completey diminishes and enrichment factor. In the narrow-band ($\Delta\nu$ = 400MHz) pumping case, the enrichment factor becomes very sensitive to the frequency change. Precise mean-frequency control within a few gigahertz is necessary to achieve the sharp enrichment peak of the multiphoton resonance, so that shot by shot spectral fluctuations of the pulses due to the Stokes phase noise must be suppressed in order to avoid spoiling the enriched product.

The main excitation pathways to a high enrichment are not strongly dependent on the frequency of the n = 0 → 1 transition. Both stepwise excitations by near-resonant one-photon transitions in the vibrational ladder and multiphoton resonance to the N-photons final state determine the selective excitation channel. The former process becomes rapidly impossible as the laser intensity increases unless more than one-color photons are used, even in the discrete region. The latter depends on how many levels one assumes as the discrete region and has an appropriate amplitude of the enrichment factor in the practical fluence.

6. REFERENCES

(※) Suzuki, M., Miyamoto, Y., Hasegawa, M., and Shimazaki, Y. : J. Nucl. Sci. Technol., 31, 293(1994).
(1) Rabinowitz, P., Kaldor, A., Gnauck, A., Woodin, R. L., and Gethner, J. S. : Opt. Lett., 7, 212(1982).
(2) Takeuchi, K., Tashiro, H., Isomura, S., Oyama, T., Satooka, S., Midorikawa, K., and Namba, S. : J. Nucl. Sci. Technol., 23, 282(1986).
(3) Alcock, A. J., Leopold, K., and Richardson, M. C. : Appl. Phys. Lett., 23, 562(1973).
(4) Sorokin, P. P., Loy, M. M. T., and Lankard, J. R. : IEEE J . Quantum Elercton., QE-13, 871(1977).
(5) Midorikawa, k., Ohashi, k., Tashiro, H., Nagasaka, K., Toyoda, K., and Namba, S. : Rev. Laser Engineering (in Japanese), 16,, 563(1988).
(6) O'Neil, F. and Whitney, W. T. : Appl. Phys. Lett., 26, 454(1975).
(7) Kim, K. C. and Person, W. B. : J. Chem. Phys., 74, 171(1981).
(8) Bagratashivili, V. N., Letokhov V. S., Makarov, A. A., and Ryabov, E. A. : "Multiple Photon Infrared Laser Photophysics and Photochemistry', Harowood Academic, Amsterdem, (1985).
(9) Allen, L. and Eberly, J. H., "Optical Resonance an Two-Level Atoms", John Wiley & Sons, New York, (1975). reprinted by Dover, New York, (1987).
(10) Sargent, M. III, Scully, M. O., and Lamb, W. E., Jr., "Laser Physics", Addison-Wesley Publishing Co., Reading, MA, (1974).
(11) Stone, J., Thiele, E., and Goodman, N. F., J. Chem. Phys., 59, 2909(1973).
(12) Okamoto, T. and Nishimura, H. : JAERI-M89-098(in Japanese), (1989).
(13) Baker, R. : J. chem. Phys., 72,3686(1980).
(14) Halonen, L. and Child, M. S. : J. Chem. Phys., 79,

559(1983).
(15) Aldrige, J. P., et al. : J. Chem. Phys., 83, 34(1985).
(16) Krohn, B. J., McDowell, R. S., Patterson, C. W., Nereson, N. G., Reisfeld, M. J., and Kim, K. C. : J. Mol. Spectrosc., 132, 285(1988).
(17) Brenner, D. M., Spencer, M. N., and Steinfeld, J. I. : J. Chem. Phys., 78, 136(1983).
(18) MacPherson, D. C., Swanson, R. C., and Carlsten, J. L. : Phys. Rev. A 39, 3487(1989).
(19) Walmsley, I. A. : Opt. Lett., 17, 435(1992).

8. Characteristics of the 100 Hz Raman laser system developed at PNC for the MLIS process (※)

Y.Miyamoto, S.Kawakami, Y.Shimazaki and H.Tashiro*
Enrichment Technology Development Section
*The Institute of Physical and Chemical Research (RIKEN)

ABSTRACT

The para-H_2 Raman laser is known to be one of the most efficient Raman convertor, in which the quantum efficiency near the main spike of a TEA-CO_2 laser pulse reaches to 100%. PNC has developed a large-scale Raman laser system to be operated at a rate of 100 Hz for the engineering-test of the molecular laser isotope separation (MLIS). The Stokes energy was slightly degraded in accordance with the increase of the repetition rate and 0.35 J/Pulse was obtained at 100 Hz repetition without gas flowing system of para-H_2.

1. INTRODUCTION

A para-H_2 Raman laser pumped by TEA-CO_2 laser radiation provides a high-power, high-efficiency, tunable source in the infrared region from 13 to 18 μm. The para-H_2 Raman laser utilizes the stimulated rotational Raman scattering (SRRS) between J=0 and J=2 levels as shown in Fig. 1

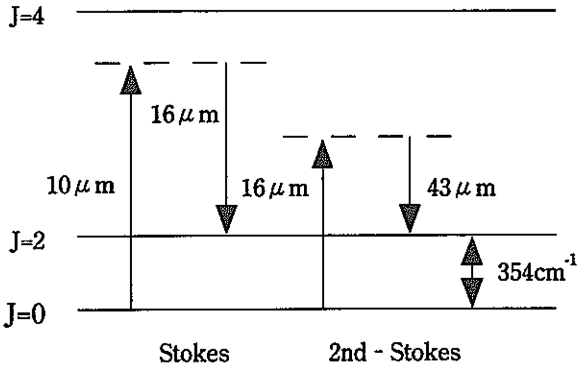

Fig. 1 Energy levels of para-H2 and related rotational Raman transition.

Since the potentiality of SRRS in H_2 for an efficient, high-energy, 16 μm source for the MLIS of UF_6 was pointed out by Byer in 1976(1), considerable effects in developing a high-power para-H_2 Raman laser have been made. With the aid of multiple-pass cell (MPC), the Raman power gain increased. It has been already established that the para-H_2 Raman laser is the best choice for the MLIS by the present art of technology. The MPC consists of the two concave mirrors as shown in Fig. 2, and the focused beam trace reflection points on the coupled mirrors(2). The para-H_2 Raman laser achieved generation of 1 J/Pulse by liquid-N_2 cool of H_2 gas(3), (4). Later, it was demonstrated that the sufficient output performance could be also obtained even in room-temperature operation(5).

Since 1988, PNC has been developing a 16 μm laser system that can be operated at 100 Hz for an engineering test aming the separation of a suitable quantity of $^{235}UF_5$. In this paper, we describe the design of the Raman laser. System performances such as optics damage at high-repetition rates, output efficiencies at 100 Hz and changes of para-H_2 gas temperature during operation are presented.

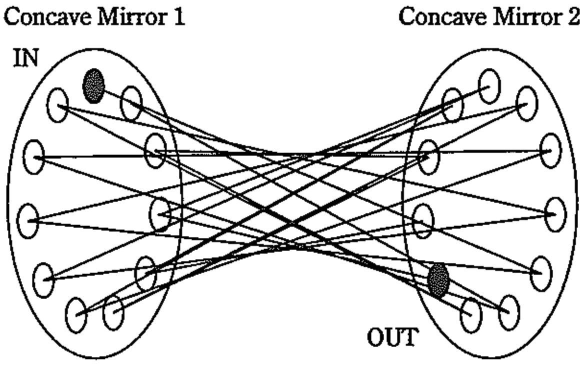

Fig. 2 Ray trace in a multiple-pass resonator.

2. TEMPERATURE DEPENDENCE OF THE PLANE WAVE RAMAN GAIN COEFFICIENT

It is known that the population density shift resulting from stimulated Raman transitions changes the diffractive index and also causes thermal expansion in the medium⁽⁶⁾. A low repetition rates, however, the diffractive index change has no serious influence on the Raman conversion because the condition of the medium recoverd before the forthcoming pulse. On the other hand, when the repetition rate becomes higher, the Raman conversion turns unstable, because the recoverly of medium condition is insufficient.

$$\alpha = \frac{4P_P G_S}{\lambda_P + \lambda_S} \tan^{-1}\left(\frac{L}{b}\right), \qquad (1)$$

The Stokes power gain per transit for a focused pump beam is given by

where P_P is the pump power, G_S the plane wave gain coefficient, L and b the mirror separation and the confocal parameter, respectively, and λ_P and λ_S the wavelengths of the pump and Stokes waves, respectively. The plane wave gain coefficient of pure rotational Raman scatterig in a diatomic gas is

$$G_S = \frac{4\lambda_S^2 \Delta N_{0-2}}{n_S^2 \hbar \omega_S \Delta \nu_R} \left(\frac{d\sigma}{d\omega}\right), \qquad (2)$$

where n_S is the refractive index at the Stokes frequency, ω_S and λ_S the Stokes frequency and wavelength. $\Delta\nu_R$ and $\Delta N_{0\text{-}2}$ are the Raman linewidth (FWHM) and the rotational inversion density of the Stokes transition, respectively.

$$\frac{d\sigma}{d\omega} = \frac{\omega_S^4 (J+1)(J+2)}{5c^4 (2J+1)(2J+3)} \gamma_{00}^2, \qquad (3)$$

The differential scattering cross section for counter-rotating circularly polarized beam is given by

$$\Delta N_{0-2} = \frac{g_{J\text{-}0}(1-\exp[-J(J+1)B_v/k_BT])}{\Sigma g_J \exp[-J(J+1)B_v/k_BT]} \cdot N, \qquad (4)$$

where γ_{00} is the molecular anisotropic polarizability. $\Delta N_{0\text{-}2}$ is given by Boltzmann distribution and written as

then

$$g_J = 2J + 1, \quad B_v = 60.8\text{cm}^{-1}.$$

$$\Delta\nu_R = \Delta\nu_R^{dif} + \Delta\nu_R^{col} = \frac{k_R^2 D_R}{2\pi} + B\rho, \qquad (5)$$

$\Delta\nu_R$ is given by the the sum of the pressure broadened width and the diffusion limited width. $\Delta\nu_R$ is written as where k_R is the angular frequency of the Raman shift, D_R diffusion constant, B the pressure broadened coefficient, and ρ the molecular density of the medium. Fig. 3 shows temperature dependence of the plane wave gain coefficient, the rotational inversion density of the Stokes transition, and the Raman linewidth using the equations (2), (4), and (5) at 1500 Torr. It is clear that the plane wave gain coefficient is reduced when the temperature of para-H_2 gas becomes higher. Therefore, the output Stokes energy is reduced at a high repetition rate generation, which causes a temperature rise of para-H_2 in the beam transit area and the reduction of the Stokes power gain coefficient.

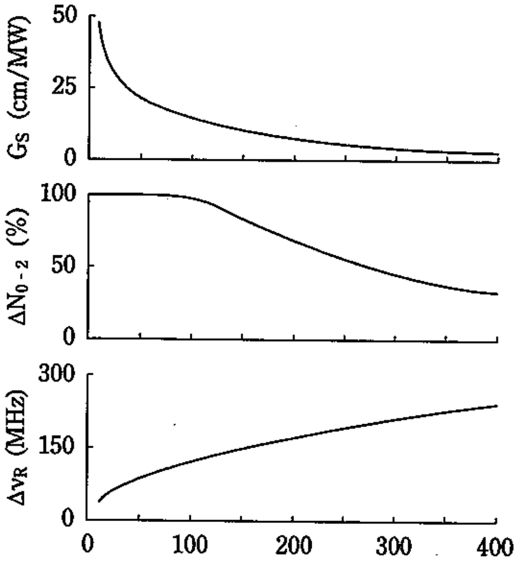

Fig. 3 Temperature dependence of the plane wave gain coefficient, the rotational inversion density of the Stokes transition and the Raman linewidth at 1500 Torr.

3. DESIGN REVIEW OF THE PARA-H_2 RAMAN LASER

Both KCl and ZnSe are competent optics materials of TEA-CO_2 lasers. However, ZnSe is mostly used, because KCl is deliquescent. The damage threshold of anti-reflection (AR) coat on ZnSe for a single TEA-CO_2 pulse was estimated to be about 10 J/cm^2 (7), (8). M.Rahe, et.al. appraised that the 50%-LIDT (laser induced damage threshold) and 0%-LIDT of Th_4/ZnS film that were coated on the ZnSe were 12.4±2.9 J/cm^2 and 8.9 J/cm^2, respectively(8). The damage threshold decreased by increasing repetition rates (9). LIDT of ZnSe and ZnS at 100 Hz became to 60% and 50%, respectively, in comparison with that at 1 Hz.

When the pump beam is inputted to an MPC, it is needed to match its focusing features to a stable mode of the MPC. A conventional type Raman laser(10) as shown in Fig. 4 had the high beam intensity on the entrance window, because the focusing mirror system was arranged outside the MPC and the beam diameter was small at the entrance window. This design easily causes damages of optics even at single shot operation. This problem was solved with the use of pre-chamber attached to the MPC, as shown in Fig. 5, which contained a beam focusing mirror system in it, resulting in the reduction of the intensity of the input beam at the entrance window. This improved design is the very effective to develop the high repetition rated para-H_2 Raman laser.

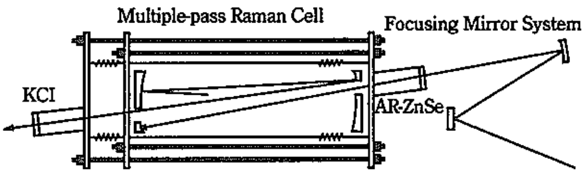

Fig. 4 Schematic diagram of the conventional type multiple-pass Raman cell.

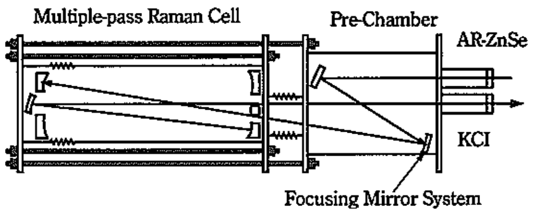

Fig. 5 Schematic diagram of the conventional type multiple-pass Raman cell.

4. EXPERIMENT

The experimental arrangement is shown in Fig. 6. The Raman laser system consisted of a master oscillator and power amplifiers (MOPA) chain of TEA-CO_2 lasers, an improved type MPC and detection equipments.

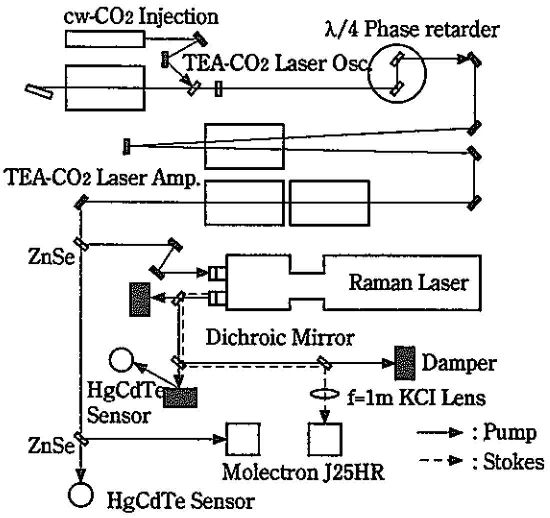

Fig. 6 Experimental configuration for 100 Hz Raman laser system

Laser pulses after passing through the amplifier section was introduced to a λ/4 phase retardor in order to convert polarization from linear to circular. The circular polarized beam was amplified to have sufficient energies for the Raman conversion by the TEA amplifiers. The amplified pump beam was inputted to the MPC and generated the Stokes beam by SRRS in para-H_2. The para-H_2 gas pressure was 1500 Torr at room temperature. The MPC had no gas flowing system.

The pump beam energy was measured by a Molectron J25HR. The beam transmitted partially through the ZnSe beam splitter was monitored as a reference. The input and depleted pump waveforms were measured by HgCdTe detectors. The output Stokes energy was measured by a Molectron J25HR. The Stokes beam was separated from the depleted pump beam with the aid of two 10/16 μm dichroic mirrors.

Fig. 7 shows the output Stokes energy as a function of repetition rate. Circles, triangles and squares indicated the Stokes radiation of which pump energies were 3.5, 4.0 and 4.5 J/Pulse, respectively. No degradation of pulse energies was found till 30 Hz. At the rates of 30 Hz - 100 Hz , however, energies per pulse were slightly degraded along with the increase of the repetition rate when no gas flowing system of para-H_2 was operated. The Stokes energy that was obtained at 100 Hz was 0.35 J/Pulse. Fig. 8 shows the depleted pump waveforms when the pump energy was 3.7 J/Pulse at 1, 25, 50, 75 and 100 Hz generation. It is clear that the depletion width became narrower and the efficiency of SRRS decreased with the increase of the repetition rate.

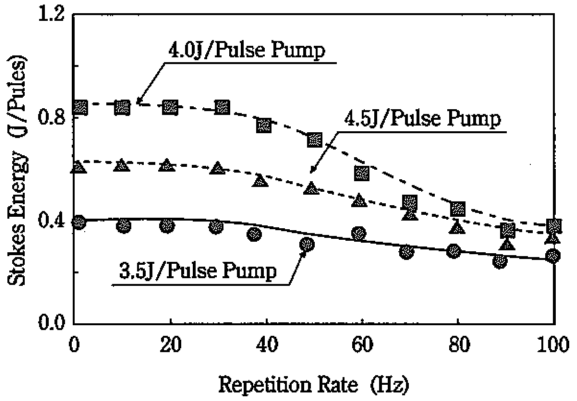

Fig. 7 Repetition rate dependence of the Stokes energy when no gas flowing system of para-H_2.

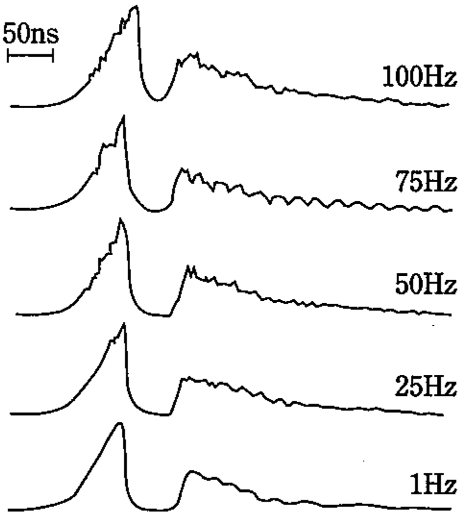

Fig. 8 Depleted pump waveforms at 3.7 J／Pulse input pump energy.

Table. 1 The para-H_2 gas temperature estimated from the reduction of the plane wave gain coefficient at several repetition rates.

Stokes Energy (J/Pulse)	Rep. rate (Hz)	Pump Energy (J/Pulse)	Energy ratio (%)	Gas Temp. (K)
0.42	1	3.5	—	290
0.42	70	4.0	114.3	315
0.41	80	4.5	128.5	335
0.68	1	4.0	—	290
0.68	50	4.5	112.5	210

The para-H_2 gas temperature was estimated from the reduction of the plane wave Raman gain coefficient at several repetition rates and pump energies, as illustrated in Table 1. This estimation was based on the equation (1) which denoted the Raman gain coefficient is in proportion to the product of the pump power and the plane wave Raman gain coefficient. In case that the pump energy was 3.5, 4.0 and 4.5 J/Pulse at 100 Hz, para-H_2 gas temperature was estimated to be 310, 330 and 345 K, respectively.

5. CONCLUSION

We designed an MPC with a pre-chamber system that contained a beam focusing mirror system in it. This improvement led us to the result the entrance optics were kept free from damages even at the 100 Hz operation. The Stokes energy was, however slightly degraded with the increase of repetition rates obtained energy was 0.35 J/Pulse at 100 Hz.

6. REFERENCES

(※) Y.Miyamoto, S.Kawakami, Y.Shimazaki, and H.Tashiro ; The 6th International Symposium on Advanced Nuclear Energy Research, Ⅲb－P4(1994).

(1) R. L. Byer ; IEEE J. Quantum Electron., 732(1976).

(2) D. R. Herriott and H. J. Schulte ; Appl. Opt., 4,883(1965).

(3) P. Rabinowiz, A.Stein, R. Brickman, and A. Kaldor; Opt. Lett., 3,147(1978).

(4) K. Midorikawa, H. Tashiro, Y. Aoki, K. Ohashi, K. Magasaka, K. Toyoda, and S. Namba ; J. Appl. Phys., 57, 1504(1985).

(5) K. Midorikawa, H. Tashiro, Y. Aoki, K. Ohashi, K. Nagasaka, K. Toyoda, and S. Namba ; Appl. Phys. Lett., 47, 1033(1985).

(6) V. Yu. Baranov, et.al. ; Sov. J. Quantum Electron., 18, 1272(1988).

(7) M. E. Innocenzi, et.al . ; Appl. Opt., 25, 658(1986).

(8) M. Rahe, et.al. ; SPIE Vol.1441 Laser-Induced Damage in Optical Materials, 133(1990).

(9) R. M. Wood ; "Laser Damage in Optical Materials", IOP Publishing Ltd., 122(1986).

(10) H. Tashiro ; OYO BUTSURI, 57, 1485(1988).

9. CURRENT STATUS OF PNC'S MLIS PROGRAM (※)

O.Suto, H.Yamaguchi, K.Tashiro, S.Kawakami and Y.Shimazaki
Nuclear Fuel Technology Development Division Power Reactor and Nuclear Fuel Development Corporation
Tokai-mura, Naka-gun, Ibaraki-ken, 319-11 Japan

ABSTRACT

According to the Atomic Energy Long-Term Program revised by the Japan Atomic Commission in 1987, PNC has started R&D on MLIS since 1988. The main target of our program is to attain a high enrichment factor under engineering conditions that has been already achieved under experimental conditions by the Institute of Physical and Chemical Research.

The test facility for enrichment tests under engineering conditions which consists of 100Hz laser systems at 16 μm and a UF_6 handling system has been developed and several tens of tests have been successfully carried out.

1. INTRODUCTION

Some uranium enrichment methods using lasers, which are more efficient than conventional commercialized techniques, have been actively investigated during the past 20 years in several countries. Enrichment costs using lasers could be lower than those of conventional methods because these methods can enrich natural uranium to nuclear reactor grade in a single enrichment stage.

One of these methods, the molecular laser isotope separation process (MLIS) is based on the isotope-selective photodissociation of gaseous UF_6 to solid UF_5, which can be removed from the gas flow by separators.

The MLIS process can be divided into three main areas:

- Cooling of UF_6 molecules mixed with carrier gases in supersonic nozzle expansion.
- Selective excitation and dissociation of UF_6 by laser radiation at 16 μm.
- Polymerization of UF_5 molecules to UF_5 particles and removal of UF_5 fine particles from the UF_6 gas.

From the standpoint of commercialization, MLIS has the great advantage that the feed material, UF_6, is used in the ccurrent nuclear fuel cycle. Thus, we have been developing this enrichment method.

In Japan, the Institute of Physical and Chemical Research (ICPR) initiated the basic research on the process in 1982. According to the Atomic Energy Long-Term Program revised by the Japan Atomic Energy Commission (JAEC) in 1987, the Power Reactor and Nuclear Fuel Development Corporation (PNC) has been involved in the R&D in cooperation with IPCR and several industrial partners since 1988. This R&D includes the design and construction of a test facility for enrichment tests under engineering conditions as well as the basic technology development for the scientific and technical understanding of this process.

This facility that consists of laser systems at 16 μm and a UF_6 handling system was completed at PNC Tokai-Works in 1990. The enrichment test was started in 1991 and recently, high isotopic selectivity has been demonstated. In the presentation, the current status of PNC's MLIS program will be discussed.(*)

2. DEVELOPMENT OF SUPERSONIC NOZZLES

We developed a supersonic nozzle that can cool the UF_6 gas to low temperature (less than 100K) during supersoinc expansion without condensation. Moreover, the UF_6 concentration in the supercooling area has to be high enough for commercialization.

However, we have to optimize a number of parameters such as nozzle shape, carrier gas, mixing ratio of UF_6 and carrier gas and inlet pressure for the development of supersonic nozzles. Thus, we first established rapid and reliable diagnostics methods of the characteristics of supersonic nozzles that are based on high resolution infrared spectroscopy in the ν_3 Q-branch region of UF_6 using tunable diode lasers.(1)

The UF_6 rotational temperature is estimated by comparing the shape of the observed absorption spectrum of the ν_3 Q-branch (Fig. 1) to the calculated spectrum (Fig. 2).

The UF_6 vibrational temperature is estimated by comparing the absorption ratio of the hot Q-branch and the fundamental Q-branch (Fig. 3) to the calculated value based on Maxwell-Boltzman statistics.

The UF_6 condensation is estimated by the saturation of the ν_3 Q-branch absorption as well at the light scattering method using an Argon-Ion laser.

We already succeeded in the development of the laval nozzle which can cool UF_6 to less than 60K without condensation (Fig. 4) and further, we have been improving the characteristics of the nozzle by using these diagnostics methods.

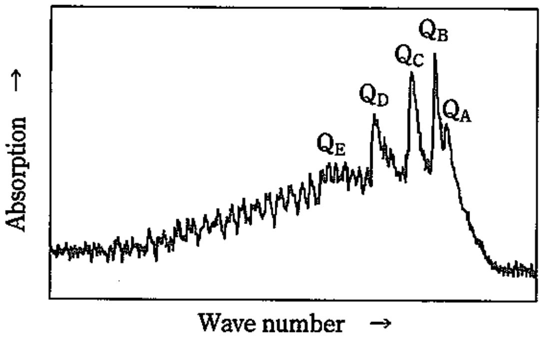

Fig. 1 Observed absorption spectrum of the ν_3 Q-branch of $^{238}UF_6$.

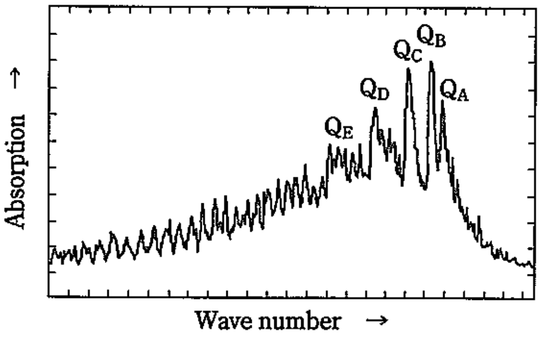

Fig. 2 Simulated absorption spectrum of the ν_3 Q-branch of $^{238}UF_6$.

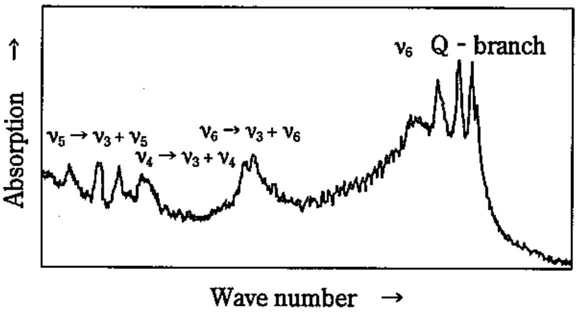

Fig. 3 Diode laser absorption scan in the region of the ν_3 Q-branch of UF_6.

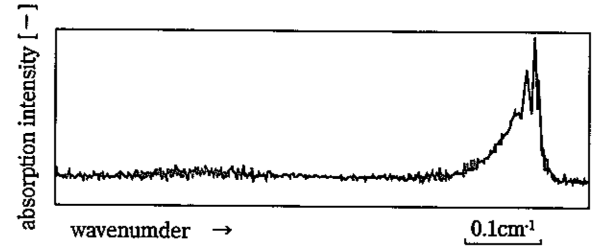

Fig. 4 Diode laser absorption scan in the ν_3 Q-branch of UF_6 in the nozzle expansion.

3. ENRICHMENT EXPERIMENT IN SUPERSONIC FREE JETS OF UF_6 WITH A MPI/TOFMS

Optimization of laser radiation parameters is extremely important in order to achieve a high enrichment factor. However, there are many parameters which include number of wavelengths, wavelength, bandwidth, frequency stability, delays, pulse shape and polarization. Besides there is on model which simulates the UF_6 multiphoton excitation exactly. One has to optimize these parameters by making a large number of enrichment experiments. However, it is very inefficient to investigate these optimum values by using the test facility because of its large consumption time.

We have established an efficient experimental method that is based on enrichment experiments in supersonic free jets followed by multiphoton ionization time-of-flight mass spectroscopy (MPI/TOFMS) of photodissociated UF_5. As shown in Fig. 5 and Fig. 6, 16μm laser pulses are focused into a pulsed free jet of UF_6 diluted with carrier gas, and UF_6 is photodissociated to UF_5. UF_5 is selectively multiphotoionized at the second harmonic frequency (λ=532nm) from a Nd:YAG laser into various ions, mainly U^{2+}. These ions are accelerated in the electric field and reach the detector, multichannel-photomultiplier (MCP). For each radiation, the TOFMS spectra, the radiation energies and the delays are recorded using digital storage oscilloscopes and then stored in a computer.

Since the enrichment factor can be estimated by averaging 1000 individual spectra, we can acquire the experimental results in a short time. The promising combinations of the laser radiation parameters resulting from these experiments are tried in the enrichment tests using the test facility and the cut, θ, as well as enrichment factor, α, are then estimated.

Although these experiments were just started, we have already achieved an enrichment factor high enough to produce the nuclear fuel. Hereafter, we will actively carry out the enrichment experiments in supersonic free jets to optimize the laser radiation parameters.

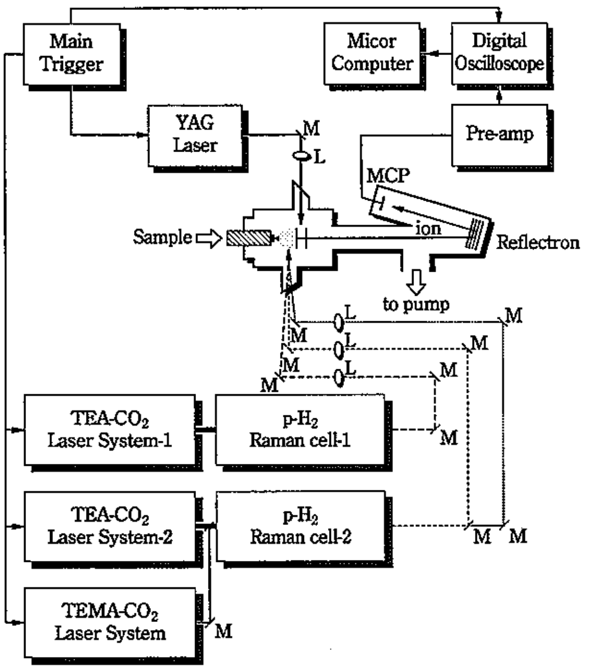

Fig. 5 Schematic diagram of enrichment experiments in supersonic free jets of UF_6 with a MPI/TOFMS.

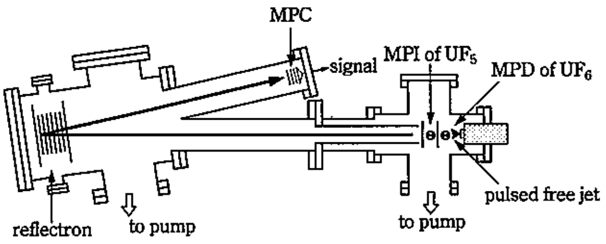

Fig. 6 Schematic diagram of MPI/TOFMS.

4. ENRICHMENT TESTS USING THE FACILITY

The test facility for enrichment tests under engineering conditions, which consists of laser systems at 16 μm (Fig. 7) and a UF_6 handling system (Fig. 8), was completed at the PNC Tokai-Works in 1990.⑵

The laser systems comprise two line-tunable TEA CO_2 laser chains, one continuous-tunable TEMA CO_2 laser chain and two multiple pass cells filled with para-hydrogen gas to convert the CO_2 laser radiation to 16 μm by Raman scattering. The typical line-tuned 16 μm pulse energy is about 600 mJ and can be delivered stably. A weak TEMA CO_2 laser pulse is also converted by Raman scattering with four-wave mixing and its continuously tuned 16 μm pulse energy is about 40 mJ.

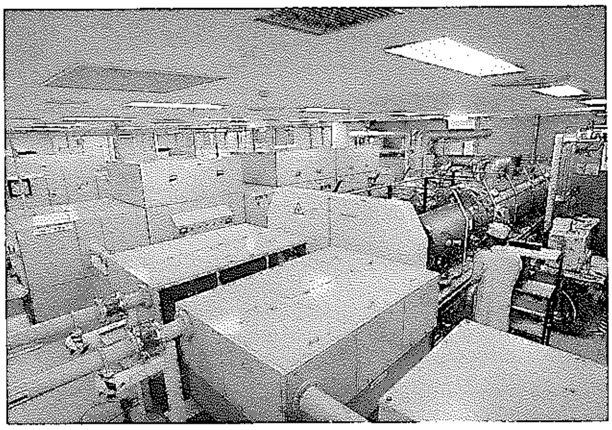

Fig. 7 16 μm laser systems.

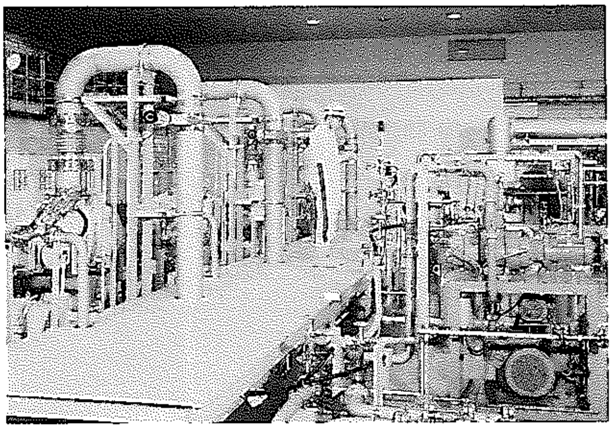

Fig. 8 UF_6 handling system.

The handling system is a closed loop apparatus mainly comprising four sets of three roots pumps, supersonic laval nozzles (a 10 cm wide continuous flow nozzle and a 25 cm wide pulsed flow nozzle with piezoelectric drivers(Fig. 9)) and two sets of UF_5 separators. Its throughputs are several kilograms of UF_6 per hour.

The enrichment test was started in 1991. First a series of tests have been done using two line-tuned 16μm laser beams and several tens of milligrams of enriched UF_5 powder has been recovered by the low pressure multi-nozzle impactor (Fig. 10).

Recently, we started the second stage enrichment tests using the continuously tunable TEMA CO_2 laser chain as well as two line-tunable TEA CO_2 laser chains. Even though only several tests have been carried out, we have already confirmed an increase in selectivity.

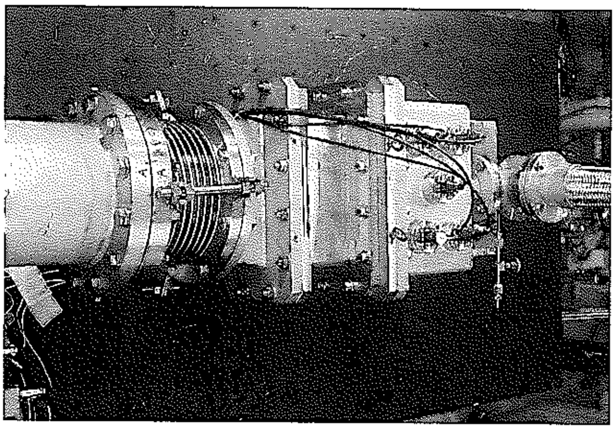

Fig. 9 Supersonic pulsed flow nozzle with a 25 cm wide slit.

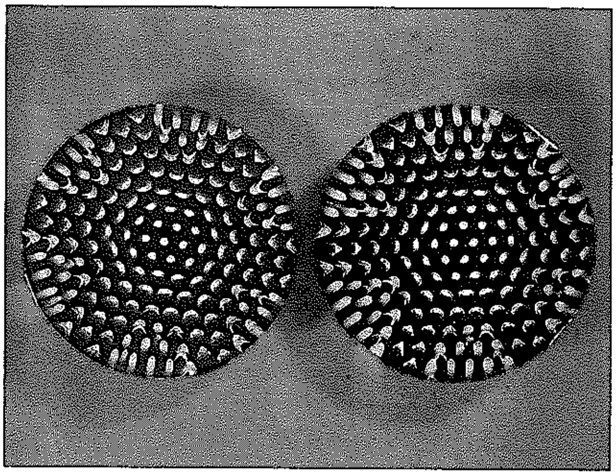

Fig. 10 Enriched UF_5 powder recovered by the low pressure multi-nozzle impactor.

5. FUTURE WORK

The evaluation of the uranium enrichment technologies , MLIS as well as AVLIS (Atomic Vapor Laser Isotope Separation) and GCP (Gas Centrifuge Process), is to be made around the year 2000 by JAEC.

We believe that the technologies and the description of the test facility presented in this paper enable us to optimize various parameters and achieve a high enough α and θ for commercialization till the C&R.

6. REFERENCES

(※) O. Suto et al. : Proceedings of the 6th Internationl Symposium on Advanced Nuclear Energy Research (1994).

(1) O. Suto et al.: Proceedings of the Third International Workshop on Separation Phenomena in Liquids and Gases, p77(1992).

(2) Y. Shimazaki et al.: Proceedings of the International Symposium on Isotope Separation and Chemical Exchange Uranium Enrichment, p144(1991).

10. Isolation of an ESR-Active Metallofullerene of $La@C_{82}$ (※)

K. Yamamoto, H. Funasaka and T. Takahashi

Innovative Technology Development Section

ABSTRACT

The ESR active lanthanofullerene, $La@C_{82}$, has been isolated from various hollow fullerenes by an efficient single stage chromatographic separation process. Pyrenylethyl-silica was used as a stationary phase with toluene as an eluent. Lanthanum-containing fullerenes were prepared by the arc heating of metal-impregnated graphite rods in a He atmosphere. FAB mass analysis of the isolated sample confirmed the isolation of $La@C_{82}$. ESR absorption spectra of the present sample prove the separation of a $La@C_{82}$ isomer with a 1.15-G hypefine splitting. The UV-visible-near-IR absorption spectra of the sample reveal near-IR absorption peaks, which are characteristic of the fullerene radical anions.

1. INTRODUCTION

Since the first macroscopic preparation of a lanthanum fullerene,(1) several metallofullerenes, including $La@C_{82}$,(1)-(8) $Y@C_{82}$,(3)-(6), (9)-(11) and $Sc@C_{82}$, (5), (12), (13) have been produced, extracted and characterized by many researchers. Because all of the species considered as metallofullerene have been obtained in mixtures together with empty all-carbon fullerenes, species-specific detection techniques such as ESR, XPS, EXAFS and mass spectrometry, have been used for characterizing the metallofullerenes. Moreover, due to a scarcity of metal-containing fullerenes in soot,(2) ultrasensitive detection techniques, especially ESR and mass spectrometry, have commonly been used in previous reports.

In the case of soluble lanthanum-containing fullerenes, mass spectrometry revealed that the available samples were mixtures of metallofullerenes with different numbers of carbons and/or metals, such as $La@C_{76}$, $La@C_{80}$, $La@C_{82}$, $La@C_{84}$, $La@C_{90}$, and $La_2@C_{80}$(4), (6), (7), (14), (15). Moreover, ESR measurements revealed that there coexists isomers of metallofullerenes, such as $La@C_{82}$, $Y@C_{82}$, and $Sc@C_{82}$, with different g-values as well as different hyperfine coupling constants.(5), (6) This may correspond to the fact that empty fullerenes such as C_{78}, C_{82} and C_{84} consist of the corresponding mixtures of structural isomers.(16), (17) Because pure metallofullerene samples were not available at that time, previous metallofullerene studies simply depended on the assumption that metal-containing species appearing both in the mass spectra and in the other species-specific measurements corresponded to each other. For this reason, purified samples are indispensable for proving this assumption, and moreover, for further metallofullerene studies.

The separation and isolation of the metallofullerenes from various hollow fullerenes was accomplished for the first time for the discandium fullerenes, $Sc_2@C_{74}$, $Sc_2@C_{82}$, and $Sc_2@C_{84}$, using two-stage high performance liquid chromatography (HPLC).(18) However, because these isolated discandium fullerenes are ESR silent, laser-desorption time-of-flight mass analyses alone were used for confirming their isolation.(18) Although these discandium fullerenes are also thought to have more than two structural isomers, respectively, isomeric purification of the discandium fullerenes is not clear.

In this study, we report the isolation of $La@C_{82}$, a ground state doublet, paramagnetic lanthanofullerene, using an efficient single-stage HPLC system. Its isolation from the other fullerene species was confirmed by fast atom bombardment (FAB) mass spectrometry as well as electron spin resonance (ESR) measurements. These measurements indicated that the isolated sample was a lanthanofullerene, $La@C_{82}$, with a hyperfine coupling constant of 1.15 G.(5), (6) Absorption spectra of the isolated $La@C_{82}$ revealed wide absorption bands ranging over the near-IR region, which were not seen for the corresponding empty C_{82} fullerene and consistent with its open shell electronic structure, described formally as $La^{3+}@C_{82}{}^{3-}$. (2), (3)

2. EXPERIMENTAL SECTION

Soot containing metallofullerenes was generated by evaporating metal-impregnated graphite rods using methods that have been described in detail.(1), (2), (4)-(7), (14) Graphite rods (Nippon Carbon Co., 13-mm diameter, EG-38H, 99.998%) were drilled out (7-mm diameter) and filled with a mixture of La_2O_3(Chori Co., 99.9%), graphite powder(Soekawa Chemical Co., 99.9%) and prepowder asphalt(Showa Shell Co.) with a ratio of 3 : 5 : 2 by weight. Before use, the rod was cured at 300℃ for 2 h and carbonized at 1000℃ for 1 h in flowing nitrogen. The resulting rod was 1-2 atom % lanthanum. The metal-impregnated graphite rod was used as the anode in a contact arc reactor(1), (14), (19)(Vacuum Metallurgical Co., UFP/SD1) at 250 A in a He(45 Torr) static atmosphere.

The resulting soot was collected and extracted for 48 h in 1,2,4-trichlorobenzene(TCB, Kanto Chemical Co., 99.0%) using a Soxhlet extraction apparatus. The extracts were dissolved in toluene prior to HPLC separation. The toluene solution of the extracts (5-ml injection volume, 2.5 mg/ml typical concentration) was separated using an HPLC system (Tosoh Co., HLC-8070) with a 2-(1-pyrenyl) ethylsilylated sillica column(20) (COSMOSIL 5PYE, 20mm i. d., 250mm length, Nacalai Tesque Co.) with toluene eluent (flow rate, 10 mL/min). In this HPLC separation process (330 nm UV detection), the peak dut to La@C_{82} was observed between the C_{84}+C_{86} and C_{88} peaks. By collecting the corresponding fraction, we obtained the pure La@C_{82} species.

The positive and negative ion fast atom bombardment (FAB) mass spectra of the isolated product were measured in a m-nitrobenzyl alcohol (m-NBA) matrix on a JMS-SX102A mass spectrometer (JEOL Co., Ltd.). A xenon beam with an energy of 6 kV was used. Some of mass spectra were measured for ^{13}C-enriched (^{13}C, 1.8%) samples.

The isomeric purification of lanthanofullerene was confirmed by ESR spectra. Both crude extracts and isolated La@C_{82} were dissolved in TCB and degased. ESR measurements were performed using a conventional X-band ESR spectrometer (Bruker ESP 300) at room temperature.

Absorption spectra for the La@C_{82} were obtained by 10mm quartz cell with Hitachi U-3410 UV-visible-near-IR spectrometer. Carbon disulfide(CS_2)was used as a solvent.

3. RESULTS AND DISCUSSION

Fig. 1A shows an HPLC profile of the crude extract of the fullerene soot redissolved in toluene. The most abundant fullerene in the mixture is C_{60}(75% relative integrated intensity at 330 nm), followed by C_{70}(15%), C_{76}(1.5%), C_{78}(2.5%), C_{82}+C_{84}+C_{86}(4%), La@C_{82}(0.5%), and C_{88}(0.5%). The scarcity of the metallofullerenes in the extracts was seen in the chromatogram. The estimated amount of La@C_{82} in each run(5 ml injection) was 0.1 mg. In this fullerene composition(major component of the extracts was C_{60}), the obtained amount of the metallofullerene was restricted by a solubility of C_{60} in toluene. The distribution of the hollow all-carbon fullerenes such as C_{60}, C_{70}, C_{76}, and C_{78} resembles that in the extracts of pure carbon soot. When pure carbon electrodes were used for producing fullerenes, no peaks were observed between the C_{84}+C_{86} and C_{88} peaks. All of the peak assignments have been performed by mass spectroscopic analyses of the corresponding fraction. It should be noted that our HPLC system could easily separate the new stable fullerenes, C_{86} and C_{88}. Their separation and identification will be published elsewhere.(21)

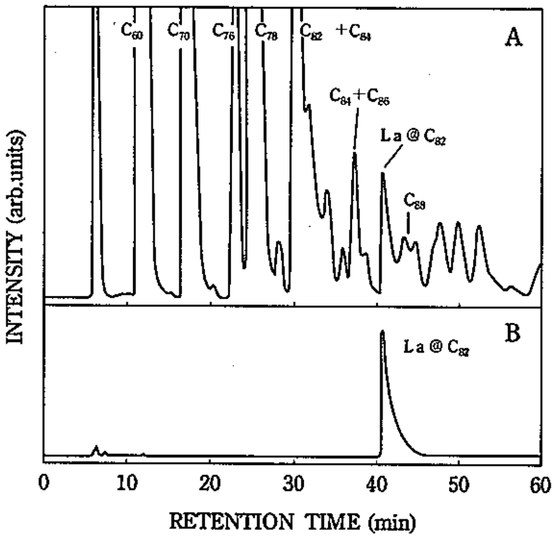

Fig. 1 (A) An HPLC trace for the redissolved crude extract of the metallofullerene soot. Peaks due to empty fullerenes such as C_{60}, C_{70}, C_{76}, C_{78} and C_{82}+C_{84} are prominent and out of scale. La@C_{82} peak (retention time : 40 min) is seen between peaks of C_{84}+C_{86} and C_{88}. (B) A repeatedly isolated HPLC trace for La@C_{82}. Besides solvent impurities near 6 min , only one peak is shown in (B).

Fig. 1B shows an HPLC trace of the purified metallofullerene, La@C_{82}.(22) From the HPLC profile of the crude extract shown in Fig. 1A, the possible slight contaminants were C_{84} and C_{86}. An additional purification procedure resulted in empty-fullerene-free La@C_{82}(99% maximum purity from relative integrated intensity of the HPLC trace) as shown in Fig. 1B. This fraction is yellow in a dilute solution and dark-yellow in a dense solution of toluene and TCB. Fig. 2 shows the positive ion FAB mass spectrum for this re-chromatographed fraction. Molecular ion peaks ascribable to La@C_{82} for the product are observed at 1123-1126 amu. The obtained ion-intensity ratio agrees well with the ^{13}C isotope distribution,(23) which was also verified for ^{13}C enriched samples. For every mass spectral signals the distribution is used as a criterion for the peak assignment. Besides

La@C_{82} peaks, some series of peaks arising from the m-NBA matrix are seen in Fig. 2.

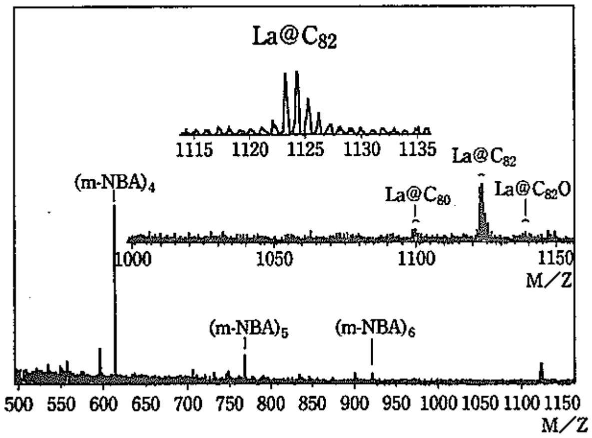

Fig. 2 FAB mass spectra of La@C_{82} in m-NBA matrix from 500 to 1160 amu and expanded views of the 1000-1160 amu and 1115-1135 amu regions. ^{139}La@$^{12}C_{82}$ (1123 amu), ^{139}La@$^{13}C^{12}C_{81}$ (1124 amu), and ^{139}La@$^{13}C_2{}^{12}C_{80}$ (1125 amu) are the main spectral peaks. Peaks around 613, 766 and 919 amu are matrix (m-NBA) tetramer, pentamer and hexamer. Trace amont of peaks ascribable to La@C_{80} and La@C_{82}O are also observed. See text.

No protonated fullerene species is seen in the mass spectra, which was also the case in the FAB mass spectra for the all carbon fullerenes(24) and scandium containing fullerenes.(12) The all-cardon species such as C_{60}, C_{70}, C_{76}, C_{78}, C_{82}, and C_{84} are not clearly observed in the mass spectrum, although the background contains a continuous distribution of peaks every amu at a several percent of the La@C_{82} signal (the S/N ratio of the mass spectral data is 5.2), which makes it impossible to analyze for trace impurities. Nevertheless the predominance of La@C_{82} among all-carbon fullerenes in Fig. 2 is consistent with the HPLC profile shown in Figure 1B. Moreover, the lanthanum containing fullerene shown in Figure 2 is La@C_{82}. In contrast, preliminary negative ion FAB mass spectra for this fraction (not shown) failed to detect signals ascribable to fullerenes. Mass spectra of the crude extract showed peaks ascribable to La@C_n (n=74, 76, 80-112), among them La@C_{82} was the most abundant. These results mean that the isolation of La@C_{82} from both empty fullerenes and other metallofullerenes is successful in the present HPLC system. It should be emphasized that there are no C_{82} ions fragmented from La@C_{82} in the mass spectra, suggesting that the La atom is strongly bound to the cage, although very weak peaks such as La@C_{80} and La@C_{78} by successive C_2 losses are accompanied. Essentially the same stability of endohedral fullerenes with respect to fragmentation has been reported extensively with FT-ICR mass spectrometry.(25) Moreover exohedral metallofullerenes are more reactive than endohedral fullerenes.(10) Therefore, observed stability for metal-elimination in the FAB mass measurement is also ascribable to the intrinsic stability of the endohedral metal-containing fullerenes. The FAB mass analyses of the exohedral fullerene derivatives, such as $C_{70}O$,(26) $C_{60}(C_6H_4)_4$,(27) or fullerene silirane derivatives(28) usually show strong fragmentation peaks such as C_{60} and C_{70}, which arise from a loss of exohedral functional group(s). It should be emphasized that there are lanthanofullerene oxide peaks of La@C_{82}O in the mass spectrum. Freshly separated sample did not show such peaks, but their intensity seems to increase as the sample exposure to the air (i. e., oxygen) increases.

The X-band ESR spectrum of the crude mixture of the lanthanum-containing fullerenes in TCB is shown in Fig. 3A, which is the same sample shown in Figure 1A. The two dominant ESR hyperfine patterns for the lanthanofullerenes were essentially the same as those previously reported.(5),(6) The main eight equally spaced lines with a hyperfine coupling constant (HFCC) of 1.15 G (denoted as I) are followed by another set of ESR lines (HFCC=0.83 G, denoted as II) of weaker intensity, as denoted by the arrows in Figure 3A. From the similarity in spectral features betweem the main and the second octets, I and II, both of them were linked to the special abundant mass spectral peak, La@C_{82}.(5),(6) Suzuki et al.(5) have assigned both of the octets to La@C_{82} with different cage structures. Hoinkis et al.(6) pointed out the second possibility that there is only one C_{82} cage structure with different La atom positions. In either of the two interpretations, the octer II corresponds to a molecular isomer of octet I. The third explantion proposed by Hoinkis et ai.(6) is that adducts are formed involving La@C_{82}, solvent molecules, or hollow fullerenes.(3),(4),(6) However, there is the fourth explanation that the octet II originates from another lanthanofullerene with a different carbon number.(7)

Fig. 3B shows the ESR spectrum of the isolated La@C_{82} fraction. Interestingly, the octer II is completely absent and only the octet I is seen in the spectrum. This indicates that the separation of molecule exhibiting the octet I signal is complete in the present HPLC process. From our mass spectrometric measurement of the isolated sample described above, this species has proved to be La@C_{82}. From now on we denote this species as La@C_{82}(octet I). For the octer I, g-value and HFCC are identical with those in Fig. 3A. No dependence of the signal on solvents (such as toluene,(5),(6) carbon disulfide,(5) and TCB) has been observed. Moreover, by mixing hollow fullerenes such as

C$_{60}$ with La@C$_{82}$(octet I), no change was observed in the ESR spectra.

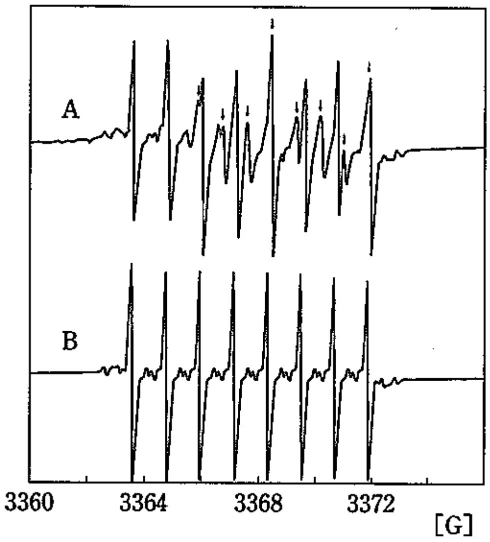

Fig. 3 ESR spectra of (A) extracted lanthanofullerene mixture (which corresponds to Fig. 1A) and (B) isolated La@C$_{82}$ fraction of sample (A) (which corresponds to Fig. 1B). Both spectra were measured at room temperature in 1,2,4 - trichlorobenzene. In (A), two octets denoted as I and II (denoted by arrows) are seen. The isolation of La@C$_{82}$ was performed on a 2-(1-pyrenyl)ethylsilylated silica column with toluene as an eluent. It is noteworthy that octet II is absent in (B).

On the other hand, the octet II was absent in all fractions eluted from the HPLC column. A similar disappearance of the octet II signal was observed for the column chromatographed sample.(7), (31) In order to further investigate this phenomena, a preliminary anaerobic HPLC separation was performed for the crude fullerene mixtures including the octets I and II. By using degassed toluene as an eluent, we found that the octet II eluted after La@C$_{82}$(octet I).(29) This result means that during our aerobic HPLC separation, the octet II species reacted with oxygen, froming an ESR-silent species. This interpretation is consistent with the previously reported properties that the octet II is very reactive and air-sensitive.(7) From both the FAB mass and ESR spectra of the La@C$_{82}$ fraction (Figs. 2 and 3B), we conclude that La@C$_{82}$ (octet I) is surely isolated by our HPLC system.

Fig. 4 shows the electronic absorption spectrum for the isolated La@C$_{82}$ (octet I) in carbon disulfide. The spectral features are quite characteristic as compared, for example, with the corresponding empty C$_{82}$ fullerene.(30) The salient features are as follows : (1) the strong absorption peaks at 637, 1010 and 1428nm(broad) are observed in the La@C$_{82}$(octet I) spectrum ; (2) the broad absorption profile continues down to 2300 nm. As previously reported,(30) the absorption spectrum of C$_{82}$ continues down to 1100 um, and shows absorption peaks at 580 and 680 nm. The near-IR region beyond 1100 nm for C$_{82}$ was found to be featureless in our study. Independently Kikuchi et al. have isolated the same La@C$_{82}$ isomer(31) and reported the same absorption spectra as in Fig. 4. It should be emphasized that Fig. 4 is much different from the absorption spectra for another reported metallofullerene, Sc$_2$@C$_{84}$,(18) which shows no ESR signals nor near-IR absorption at wavelength above 800 nm. To understand the absorption spectra of La@C$_{82}$(octet I) qualitatively, one should consider the absorption bands for fullerene radical anions. The anionic forms of C$_{60}$ and C$_{70}$ (i. e. C$_{60}^{n-}$and C$_{70}^{n-}$ where n=1-4) show characteristic near-IR absorption bands,(32), (33) that are not observed for neutral C$_{60}$ and C$_{70}$. For example, C$_{60}^{3-}$ shows absorption bands in the near-IR and visible regions with peaks at 780, 850, 1000 and 1370 nm.(32) Note that the magnetic ground state of C$_{60}^{3-}$ is a doublet.(34) C$_{70}^{3-}$ shows absorption bands in the near-IR and visible regions with peaks at 760 and 1170 nm.(33) From the previous experimental finding that La@C$_{82}$ is paramagnetic and its open shell electronic structure(i. e. doublet) is described formally as La^{3+}C$_{82}^{3-}$, (2), (3) the absorption features shown in Fig. 4 are considered as a spectral superposition of a singlet La^{3+} and a doublet C$_{82}^{3-}$ to a first-order approximation. Note that some C$_{60}^{-}$ salts in benzonitrile have similar near-IR spectra ascribable to C$_{60}^{\cdot -}$(35) We may attribute the broad absorption profile continuing down to 2300 nm to the lower molecular symmetry (C$_{3v}$/C$_s$, C$_{2v}$/C$_1$, or C$_2$) of C$_{82}$ (17), (36) as compared with C$_{60}$(I$_h$) and C$_{70}$(D$_{5h}$), although the carbon cage symmetry of La@C$_{82}$(octet I) is not clear at present time.

There have been several theoretical investigations for both fullerene anions(37), (38) and lanthanofullerenes, LaC$_{60}$(39) and LaC$_{82}$.(36), (40) Early Huckel MO calculations for the electronic structure of fullerene anions predicted the magic number stability of fullerene dianions including C$_{82}^{2-}$ from its estimated HOMO-LUMO energy gaps.(37), (38) Restricted open-shell Hartree-Fock self-consistent-field MO calculations of C$_{60}$ containing a central La atom found that the two metal valence electrons transfer to the cage LUMO, but electronic ground stateis qartet.(39) These electron transfer to the fullerene cages is expected to show the charge-transfer bands in the near-IR region, which cause red-shift of the absorption bands. More advanced electronic structure calculations on La@C$_{82}$ have been performed by two groups. Laasonen et al. performed fully optimized ab initio calculations for La@C$_{82}$ by the local density approximation of the density functional theory.(40) They found that certain off-center metal position is more stable and the three metal valense electrons transfer to the cage, forming $La^{3+}@C_{82}^{3-}$, which is consistent with the experimental results.(2), (3) They also found that La does not simply behave as an electron donor but actually forms a strong bond with the C atom of the cage. Their estimated HOMO-LUMO gap at the configuration is about 0.4 eV. Since their calculations include excited states, it may correspond to our absorption onset of 0.54 eV (2300 nm). Nagase et al. found similar results by unrestricted Hartree-Fock calculations.(36)

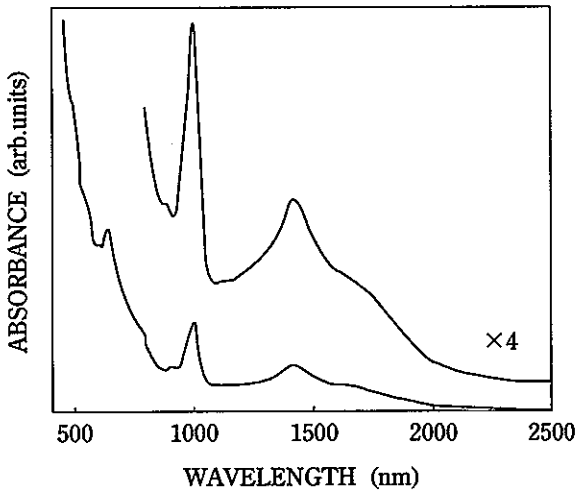

Fig. 4 UV-visible-near-IR absorption spectrum from 400 to 2500 nm for the isolated $La@C_{82}$ (octet I) in CS_2 at room temperature. The feature at 800 nm corresponds to an instrument detector change. Characteristic absorption features appear in the near-IR region, which are not observed in the corresponding C_{82} spectrum.

In conclusion, by taking abvantage of the well-separated retention times of the hollow fullerenes and lanthanofullerenes, an ESR-active $La@C_{82}$ isomer has been separated efficiently on a 2-(1-pyrenyl) ethylsilylated silica column. FAB mass analyses as well as ESR spectra prove its successful isolation. Its UV-visible-near-IR absorption spectra reveal near-IR absorption peaks down to 2300 nm, which is consistent with its open shell electronic structure.

4. ACKNOWLEDGMENT

We express thanks to Mr. Kenji Sugiyama (PNC), Koji Sakurai(Zuiho Sangyo Co.), Toshiaki Ishiguro (Genshiryoku Gijyutsu Co.) and Yoshiharu Kano (Genshiryoku Gijyutsu Co.) for their experimental help. We would also thank Dr. Achiba for sending us a preprint of ref. 31

5. REFERENCES AND NOTES

(※) Yamamoto, K. ; Funasaka, H. ; Takahashi, T. J. Phys, Chem. 1994, 98, 2008.

(1) Chai, Y. ; Guo, T. ; Jin, C. ; Haufler, R. E. ; Chibante, L. P. F. ; Fure, J. ; Wang, L. ; Alford, J. M. ; Smalley, R. E.
J. Phys. Chem. 1991, 95, 7564.

(2) Johnson, R. D. ; de Vries, M. S. ; Salem, J. ; Bethune, D. S. ; Yannoni, C. S.
Nature 1992, 355, 239.

(3) Weaver, J. H. ; Chai, Y. ; Kroll, G. H. ; Jin, C. ; Ohno, T. R. ; Haufler, R. E. ; Guo, T. ; Alford, J. M. ; Conceicao, L. P. F. ; Chibante, L. P. F. ; Jain, A. ; Palmer, G. ; Smalley, R. E. Chem. Phys. Lett. 1992, 190, 460.

(4) Ross, M. M. ; Nelson, H. H. ; Callahan, J. H. ; McElvany, S. W. J. Phys. Chem., 1992, 96, 5231.

(5) Suzuki, S. ; Kawata, S. ; Shiromaru, H. ; Yamauchi, K. ; Kikuchi, K. ; Kato, T. ; Achiba, Y.
J. Phys. Chem. 1992, 96, 7159.

(6) Hoinkis, M. ; Yannoni, C. S. ; Bethuno, D. S. ; Salem, J. R. ; Johnson, R. D. ; Crowder, M. S.; de Vries, M. S. Chem. Phys. Lett. 1992, 198, 461.

(7) Bandow, S, ; Kitagawa, H. ; Mitani, T. ; Inokuchi, H. ; Saito, Y. Yamaguchi, H. ; Hayashi, N. ; Sato, H.; Shinohara, J. Phys. Chem. 1992, 96, 9606.

(8) Funasaka, H. ; Yamamoto, K. ; Sakurai, K. ; Ishiguro, T. ; Sugiyama, K. ; Takahashi, T. ; Kishimoto, Y. Fullerene Sci. Technol. 1993, 1, 437.

(9) Shinohara, H. ; Sato, H. ; Saito, Y. ; Ohkohchi, M. ; Ande, Y. J. Phys. Chem. 1992, 96, 3571.

(10) McElvany, S. W.
J. Phys. Chem. 1992, 96, 4935.

(11) Soderholm, L. ; Wurz, P. ; Lykke, K. R. ; Parker, D. H. ; Lytle, F. W.
J. Phys. Chem. 1992, 96, 7153.

(12) Shinohara, H. ; Sato, H. ; Ohkohchi, M. ; Ando, Y. ; Kodama, T. ; Shida, T. ; Kato, T. ; Saito, Y.
Nature 1992, 357, 52.

(13) Yannoni, C. S. ; Hoinkis, M. ; de Vries, M. S. ; Bethune, D. S. ; Salem, J. R. ; Crowder, M. S. ; Johnson, R. D.
Science 1992, 256, 1191.

(14) Alvarez, M. M. ; Gillan, E. G. ; Holczer, K. ; Kaner, R. B. ; Min, K. S. ; Whetten, R. L.
J. Phys. Chem. 1991, 95, 10561.

(15) Yeretzian, C. ; Hansen, K. ; Alvarez, M. M. ; Min, K. S. ; Gillan, E. G. ; Holczer, K. ; Kaner, R. B. ; Whetten, R. L. Chem. Phys. Lett. 1992, 196, 337.

(16) Diederich, F. ; Whetten, R. L. ; Thilgen, C. ; Ettl, R. ;

Chao, I. ; Alvarez, M. M.
Science 1991, 254, 1768.

(17) Kikuchi, K. ; Nakahara, N. ; Wakabayashi, T. ; Suzuki, S. ; Shiromaru, H. ; Miyake, Y. ; Saito, K. ; Ikemoto, I. ; Kainosho, M. ; Achiba, Y.
Nature 1992, 357, 142.

(18) Shinohara, H. ; Yamaguchi, H. ; Hayashi, N. ; Sato, H. ; Ohkohchi, M. ; Ando, Y. ; Saito, Y.
J. Phys. Chem. 1993, 97, 4259.

(19) Haufler, R. E. ; Chai, Y. ; Chibante, L. P. F. ; Conceicao, J. ; Jin, C. ; Wang, L. ; Maruyama, S. ; Smalley, R. E.
Mat. Res. Soc. Symp. Proc., 1990, 206, 627.

(20) Kimata, K., ; Hosoya, K. ; Akai, T. ; Tanaka, N.
J. Org. Chem., 1993, 58, 282.

(21) Yamamoto, K. ; Funasaka, H. ; Takahashi, T.
Manuscript in preparation.

(22) Although its elution was slightly later that in the case of the fullerene mixture as shown in Figrure 1A, both peaks corresponded to each other, which was caused by the slight decrease of the column temperature.

(23) Shinohara, H. ; Sato, H. ; Saito, Y. ; Izuoka, A. ; Sugawara, T. ; Ito, H. ; Sakurai, T. ; Matsuo, T.
Rapid Commun. Mass Spectrom. 1992, 6, 413.

(24) Shinohara, H. ; Sato, H. ; saito, Y. ; Takayama, M. ; Izuoka, A. ; Sugawara, T.
J. Phys. Chem. 1991, 95, 8449.

(25) Wiess, F. D. ; Elkind, J. L. ; O'Brien, S. C. ; Curl, R. F. Smalley, R. E.
J. Am. Chem. Soc. 1988, 110, 4464.

(26) Diederich, F. ; Ettl, R. ; Rubin, Y. ; Whetten, R. L. ; Beck, R. ; Alvarez, M. ; Ans, S. ; Sensharma, D. ; Wudl, F. ; Khemani, K. C. ; Koch, A.
Science 1991, 252, 548.

(27) Tsuda, M. ; Ishida, T. ; Nogami, T. ; Kurono, S. ; Ohashi, M. Chem. Lett. 1992, 2333.

(28) Akasaka, T. ; Ando, W. ; Kobayashi, K. ; Nagase, S.
J. Am. Chem. Soc 1998, 115, 1605.

(29) Due to the reaction with a trace amount of oxygen in solution, signal intensity of the octet II was not so strong, therefore, the main component of this fraction was hollow fullerenes such as C_{88}. The successful isolation of the octet II probably has more to do with its higher aerobic sensitivity.

(30) Kikuchi, K. ; Nakahara, N. ; Wakabayashi, T. ; Honda, M. ; Matsumiya, H. ; Moriwaki, T. ; Suzuki, S. ; Shiromaru, H. ; Saito, K. ; Yamauchi, K. ; Ikemoto, I. ; Achiba, Y.
Chem. Phys. Lett. 1992, 188, 177.

(31) Kikuchi, K. ; Suzuki, S. ; Nakao, Y. ; Nakahara, N. ; Wakabayashi, T. ; Shiromaru, H. ; Saito, K. ; Ikemoto, I. ; Achiba, Y.
Chem. Phys. Lett. in press.

(32) Lawson, D. R. ; Feldheim, D. L. ; Foss, C. A. ; Dorhout, P. K. ; Elliot, C. M. ; Martin, C. R. ; Parkinson, B.
J. Electrochem. Soc. 1992, 139, L68.

(33) Lawson, D. R. ; Feldheim, D. L. ; Foss, C. A. ; Dorhout, P. K. ; Elliot, C. M. ; Martin, C. R. ; Parkinson, B.
J. Phys. Chem. 1992, 96, 7175.

(34) Dubois, D. ; Jones, M. T. ; Kadish, K. M.
J. Am. Chem. Soc. 1992, 114, 6446.

(35) Stinchcombe, J. ; Penicaud, A. ; Bhyrappa, P. ; Boyd, P. D. W. ; Reed, C. A.
J. Am. Chem. Soc. 1993, 115, 5212.

(36) Nagase, S. ; Kobayashi, K. ; Kato, T. ; Achiba, Y.
Chem. Phys. Lett. 1993, 201, 475.

(37) Manolopoulos, D. E. ; Fowler, P. W.
Chem. Phys. Lett. 1991, 187, 1.

(38) Flowler, P. W. ; Manolopoulos, D. E.
Nature 1991, 355, 428.

(39) Chang, A. H. ; Ermler, W. C. ; Pitzer, R. M.
J. Chem. Phys. 1991, 94, 5004.

(40) Laasonen, K. ; Andreoni, W. ; Parrinello, M.
Science 1992, 258, 1916.

11. INCINERATION OF RADIOACTIVE FISSION PRODUCTS AND TRANSURANICS BY MUONCATALYZED FUSION (※)

H. HARADA, H. TAKAHASHI*, ARNOLD L. ARONSON*, T. KASE, K. KONASHI†, N. SASAO**

Innovative Technology Development Section
* Brookhaven National Laboratory, Upton, New York 11973 USA
**Power Reactor and Nuclear Fuel Development Corporation

ABSTRACT

A system of nuclear transmutation is presented in which fission products and transuranics (TRU) are incinerated using 14-MeV neutrons produced by muoncatalyzed fusion (μCF) and a subcritical core composed of fission products and TRU. The 14-MeV neutrons produced by μCF are used to transmute ^{90}Sr (fission product) by the (n, 2n) reaction. The outcoming neutrons from the ^{90}Sr cell transmute TRU through fission reactions and ^{99}Tc through (n, γ) reactions. This fission energy is converted into electric energy to supply 4GeV-25 mA deuteron beam power, which is used to produce μ^- mesons. We also evaluate the production of tritium that is consumed as a fuel for μCF. The feasibility of the system was analyzed by the MCNP Monte Carlo neutron transport code. The results show that this system can be subcritical and can transmute fission products and TRU with an incineration half-life of ~ 1 yr and that deuteron beam energy and tritium fuel required to operate the system can be supplied within the system cycle itself.

1. INTRODUCTION

Methods of incinerating radioactive wastes—fission products and transuranics (TRU)—have been vigorously investigated in the last decade.(1)~(3) The neutron capture reaction and the fission reaction have received the greatest attention as ways to incinerate fission products and TRU, respectively.

Recent measurements showed that the thermal neutron capture cross sections of ^{90}Sr and ^{137}Cs were 15.3 mb (Ref. 4) and 0.25 b (Ref. 5), respectively. If a fission reactor, similar to that proposed by Taube[1], were used to transmute these nuclei, with the requirement of an incineration half-life of 2 yr, the thermal neutron flux in the device would have to be as high as 6.5×10^{17} and 4.0×10^{16} n/cm$^2\cdot$s for ^{90}Sr and ^{137}Cs, respectively. Such a high flux is beyond the technology of current reactors.

To overcome this difficulty, it was proposed(6),(7) that the (n, 2n) reaction triggered by 14-MeV neutrons should be used to incinerate ^{90}Sr and ^{137}Cs ; the (n, 2n)cross section is typically 2 b for fission products at 14-MeV neutrons. However, Kase et al.(8) calculated that the electric energy required to transmute one ^{137}Cs with a 14-MeV neutron produced by μCF was high as 195 MeV ; a more pessimistic result of 300 MeV was reported by Petrov.(9)

To overcome such a huge input energy, we examined a system that included a subcritical core composed of fission products and TRU, where 14-MeV neutrons produced by the μCF reaction transmute ^{90}Sr or ^{137}Cs (FP-1)[a], and outcoming neutrons from the fission products cell induce a fission reaction in the TRU cell. This hybird core, composed of fission products and TRU, has the advantage that the output of thermal energy by the fission reaction could be used as the input of electric energy to the driver that produces μ^- mesons. Furthermore, excess neutrons could be used to transmute ^{99}Tc and other

---

†Current address : Institute for Material Research, Oarai, Ibaraki-ken, 311-13 Japan.

[a] Radioactive fission product nuclides can be divided into two groups for incineration studies. The first group comprises ^{85}Kr (11 yr), ^{90}Sr (29 yr), and ^{137}Cs (30 yr). The thermal neutron capture cross sections of these nuclei are <1 b:unmeasured for ^{85}Kr, 15.3 mb for ^{90}Sr, and 0.25 b for ^{137}Cs. The second group is ^{93}Zr (1.5×10^6 yr), ^{99}Tc (2.1×10^5 yr), ^{129}I (1.6×10^7 yr), and ^{135}Cs (2×10^6 yr). The thermal neutron capture cross sections of these nuclei are >1 b:1~2 b for ^{93}Zr, 19 b for ^{99}Tc, 18 b for ^{129}I, and 5.8 b for ^{135}Cs. The half-life of eash nuclide is shown in parentheses.

elements (FP-2)[a] by the (n, γ) reaction and produce the tritium fuel for μCF by the ^{6}Li (n, α) reaction. In addition, this system has a safety advantage because it can be run subcritically.

To evaluate the feasibility of this system as an incinerator, we calculated the neutronics of the system and performed a paramenter search to optimize the system's dimensions using the MCNP Monte Carlo neutron transport program.(10) The results show that this system works effectively as an incinerator for both fission products and TRU and that both the electrical energy and tritium fuel required to operate the system can be produced within the system itself.

Table. 1 Atomic Fraction of TRU in the Subcritical Core

Nuclide	Atomic Fraction (%)
^{237}Np	21.0
^{241}Am	24.0
^{243}Am	4.3
^{244}Cm	0.9
^{238}Pu	0.8
^{239}Pu	29.0
^{240}Pu	13.4
^{241}Pu	4.4
^{242}Pu	2.3

2. INCINERATION SYSTEM AND ANALYSIS PROCEDURE

Fig. 1 is a conceptual picture of the incineration system briefly described in Sec. 1. By bombarding a beryllium target with a 4 GeV-25 mA deuteron beam, negative pions are produced at a rate of $1.5\times10^{17}s^{-1}$. The pions decay to muons, which are used for the μCF reaction. The muon beam enters a gas target composed of D_2, T_2, and deuterium-tritium (D-T) molecules that are compressed to a pressure of 1000 atm, and it induces μCF reaction. The 14-MeV neutrons produced by this μCF reaction then are used to incinerate FP-1, ^{90}Sr, etc., by the (n, 2n) reaction. Outcoming neutrons are used to incinerate TRU, ^{237}Np, etc., by the fission reaction and FP-2, ^{99}Tc, etc., by the neutron capture reaction. The thermal energy produced by the fission reaction is converted into electrical energy, which is used as the input energy of the deuteron accelerator. If fission energy could supply 100% of the input energy to the accelerator, no external source of electric power would be required to incinerate fission products and TRU. The ^{6}Li-Al alloy(11) was included in the core to produce tritium fuel by the ^{6}Li(n, α) T reaction.

It was estimated[12] that one muon is produced with a beam energy of 4.5 GeV, and 20% of the muon beam is lost at the window of the gas target ; the μCF reaction is repeated 175 times for every μ^- entering the target. Based on this assumption, the electrical energy required to produce one 14-MeV neutron is 64 MeV ; the efficiency of transfer from electric power to deuteron beam energy was assumed to be 50%. Neutron yields (14 MeV) are $3.1\times10^{19}s^{-1}$ when a 4 GeV-25 mA deuteron accelerator is used. To decrease the loss of muons at the window of the gas target, the momentum of the muons should be made monochromatic as well as possible. This will be partially done by separating muons according to their momentums and slowing down the muons of large momentum.

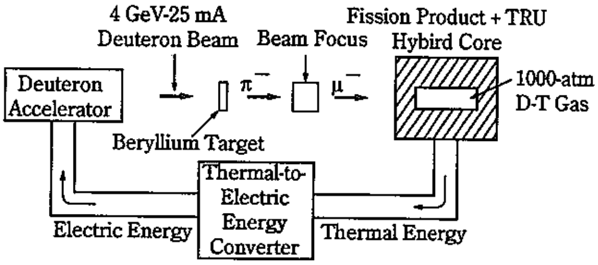

Fig. 1 A conceptual picture of the incineration system, which is composed of a 4 GeV-25 mA deuteron accelerator and a fission product-TRU hybird core.

Fig. 2 shows the r-z cross section of the subcritical core composed of fission products and TRU. The stainless steel cylinder at the center of the core has the following dimensions : thickness of 1cm, an inner radius of 2.5cm, and an inner length of 34cm ; the cylinder contains D_2, T_2, and D-T gases under a pressure of 1000 atm. The cell around the cylinder contains as a representative FP-1 ^{90}Sr, which has the smallest (n, γ) cross-sectional value among radioactive fission products ; ^{137}Cs can be transmuted more easily than ^{90}Sr. The cell is covered with 1cm of stainless steel, has an inner radius of 19cm and an inner length of 40cm, and contains 114kg of ^{90}Sr metal with a density of 2.6g/cm^3. According to out preliminary investigation, the probability of the ^{90}Sr(n, 2n) reaction occurring is decreased by 12% by scattering from 1-cm-thick stainless steel.

The cell around the ^{90}Sr cell contains TRU, which is composed of ^{237}Np, ^{241,243}Am, ^{244}Cm, and $^{238\text{-}242}$Pu. Table 1 shows the fraction of each element that was obtained by mixing plutonium and minor actinides with a 1 : 1 ratio. By incinerating the minor actinide with plutonium fissile material and choosing a suitable plutonium/minor actinide ratio, the increase of reactivity as a result of burunp of ^{237}Np can be suppressed, and reactivity can be maintained almost constant during the burnup cycle. For a neutron spectrum close to that of a fast reactor, the plutonium/minor actinide ratio is 0.5 to 1.0 (Ref. 13). Outcoming neutrons from the ^{90}Sr cell induce fission reactions and neutron capture reactions in the TRU cell. Neutrons emerging from the TRU cell are thermalized by the D_2O moderator and are then used to transmute ^{99}Tc, which is a representative FP-2, by the ^{99}Tc(n, γ) ^{100}Tc reaction and, furthermore, to produce tritium by the ^{6}Li (n, α) T reaction. Fig. 3 shows neutron spectra in the ^{90}Sr, TRU, and ^{99}Tc cells, which indicate the system performance. In the ^{90}Sr cell, there is a strong peak of 14-MeV neutrons. The neutron spectrum in the TRU cell looks like that of a fast reactor.

Although the TRU cell is so small that the core is subcritical, the heat per unit volume generated in the TRU cell is greater than that in the core of a 1-GW(thermal) commercial reactor because high-flux 14-MeV neutrons continually enter the TRU cell. Therefore, a helium-cooled particle fuel was used in the design of the TRU cell ; this fuel has a high heat transfer efficiency because of its large surface-to-volume ratio. We adapted the fuel concept designed by Todosow et al.,(14) which is show in Fig. 4.

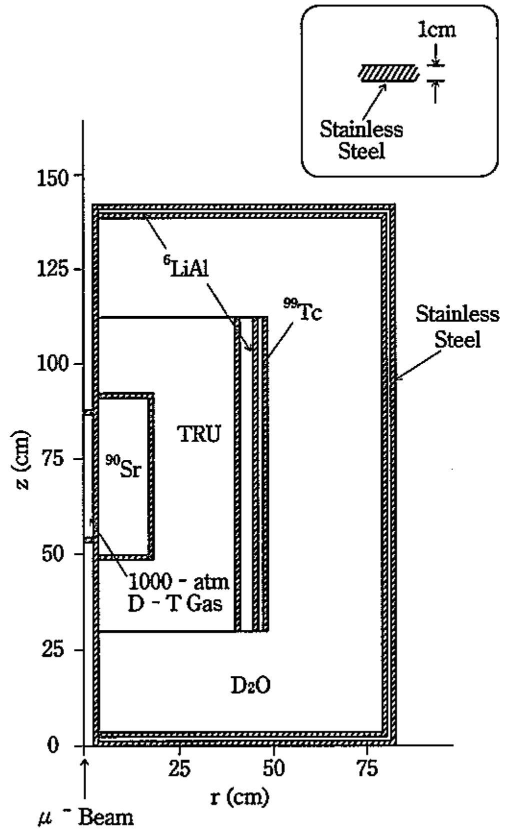

Fig. 2 The r-z cross section of the subcritical core composed of fission products (^{90}Sr and ^{99}Tc) and TRU. Lithium-6 is used to produce tritium fuel for the μCF reaction through the ^{6}Li(n, α) T reaction.

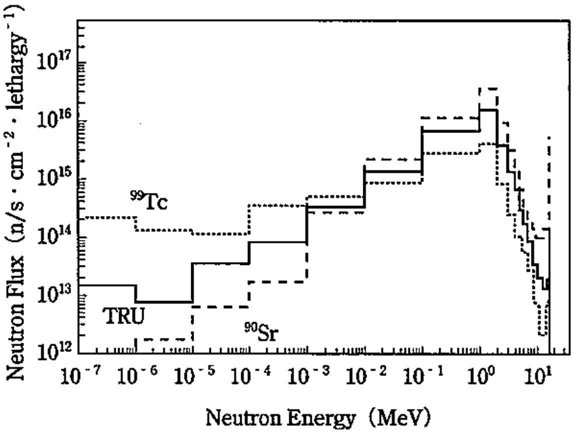

Fig. 3 Histograms of neutron fluxes per lethargy in the ^{90}Sr (dashed line), TRU (solid line), and ^{99}Tc (dotted line) cells.

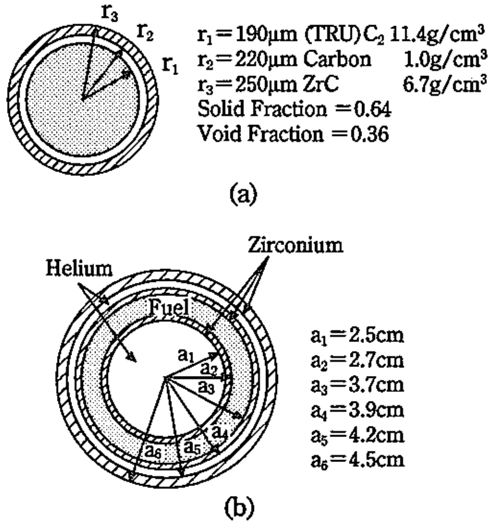

Fig. 4 (a) Cross section of a particle fuel : TRU carbide is covered with 30μm of carbon and 30μm of ZrC. The radius of each material is shown.
(b) The z cross section of a fuel rod : The particle fuel in Fig. 4a is set in a fuel cell. The fuel is cooled by helium gas, and the wall material is zirconium. The radius of each cell is shown.

To calculate the neutronics of this core, we used the MCNP code.(10) For the nuclear cross sections required in MCNP, the ENDF/B-VI nuclear data library(15) was used ; the (n, γ) cross section of ^{90}Sr in the thermal energy region was modified to reflect the recent experimental data,[4] and the (n, 2n) cross section of ^{90}Sr, which was calculated using an optical potential and a statistical model, was added to the library.(16) From these nuclear data, the probabilities of (n, 2n), (n, f), and (n, γ) reactions occurring were calculated for each nuclide.

The dimensions of the ^{90}Sr cell in Fig. 2 were determined based on the incineration half-life $T_{1/2}$ and the ^{90}Sr (n, 2n) reaction probability P. Fig. 5 shows $T_{1/2}$ and P as a function of the inventory of the ^{90}Sr cell. Although $T_{1/2}$ increases linearly as a function of inventory, P shows a tendency to saturate at an inventory of ~120kg. Therefore, the weight of ^{90}Sr was fixed as 114kg for a configuration in which the conditions of $T_{1/2} \approx 1.6$ yr and P ≈ 31% can be achieved. The tendency of P to saturate can be explained by the downscattering of 14-MeV neutrons in the ^{90}Sr cell.

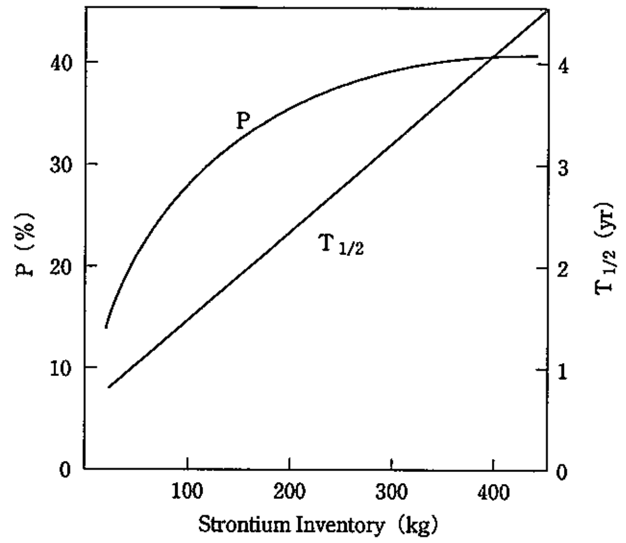

Fig. 5 The incineration half-life $T_{1/2}$ and the (n, 2n) reaction probability for ^{90}Sr.

3. RESULTS AND DISCUSSION

Table. 2 shows the probabilities of the (n, 2n), (n, γ), and (n, f) reactions for each nuclide in the core for the input of a 14-MeV neutron. The number of total neutrons generated by the (n, 2n) and (n, f) reactions was 4.2, and the number of leakage neutrons from the core was 0.11 per 14-MeV neutron.

The incineration half-life for each nuclide was calculated from three quantities:

1. the inventory of each nuclide in the core, shown in column 2 of Table. 2
2. the 14-MeV neutron generation rate; i.e., 3.1×10^{19} n/s
3. the sum of reaction probabilities for each nuclide, shown in column 6 of Table. 2.

The calculated incineration half-lives for each nuclide are shown in column 7 of Table. 2. In calculating the fission product half-lives, generation of these nuclei by the TRU(n, f) reaction was not taken into account. For reference, the incineration half-lives of the structural materials are also shown. The TRU(n, γ) or (n, 2n) reaction produces more TRU and therefore dose not effectively reduce the amount of TRU. Therefore, the TRU incineration half-lives, calculated by using only the (n, f) reaction rate, are shown in parentheses in column 8 of Table. 2.

Table. 2 Reaction Probability and Incineration Half-Life for Each Nuclide

Nuclide	Inventory (kg)	Reaction Probability per 14-MeV Neutron				Half-Life (yr)
		(n,2n) (%)	(n, γ) (%)	(n,f) (%)	Total (%)	
^{237}Np	72.2	0.00	28.73	9.62	38.35	0.34(1.35)[a]
^{241}Am	83.9	0.00	40.07	15.54	55.61	0.27(0.96)
^{243}Am	15.2	0.00	4.66	2.27	6.93	0.39(1.18)
^{244}Cm	3.0	0.00	0.53	0.51	1.04	0.51(1.03)
^{238}Pu	2.7	0.00	0.68	0.90	1.58	0.31(0.54)
^{239}Pu	100.4	0.00	16.80	59.61	76.41	0.23(0.30)
^{240}Pu	46.5	0.00	0.90	8.31	9.21	0.90(1.00)
^{241}Pu	15.5	0.00	0.27	10.95	11.22	0.24(0.25)
^{242}Pu	8.1	0.00	0.16	1.02	1.18	1.21(1.40)
TRU(sum)	347.5	0.00	92.80	108.73	201.53	0.31(0.57)
Carbon[b]	72.7	0.00	0.54	0.00	0.54	47 000
Zirconium[b]	831.9	5.04	10.23	0.00	15.27	25.52
^{90}Sr	113.9	31.69	1.78	0.00	33.47	1.62
^{90}Tc	277.9	0.34	72.60	0.00	72.94	1.64
Tritium	0.1	0.20	0.00	0.00	0.20	6.41
Deuterium	446.0	3.14	0.62	0.00	3.76	25 000
^{16}O	1783.8	0.00	1.07	0.00	1.07	45 000
^{6}Li	6.7	0.00	97.85[c]	0.00	97.85	0.49
^{27}Al	272.0	0.00	1.13	0.00	1.13	380
Chromium[b]	175.3	0.90	10.10	0.00	11.00	13.10
Iron[b]	1259.3	2.99	54.94	0.00	57.93	16.65

[a] Incineration half-Life determined by (n, f) reaction rate is given in parentheses.
[b] Average of natural abundance was adapted for nuclear data.
[c] (n, α) reaction probability.

Strontium-89, generated by the ^{90}Sr(n, 2n) reaction, decays to ^{89}Y(stable nuclei) with a half-life of 50 days. Therefore, the amount of ^{89}Sr and ^{89}Y increases in the ^{90}Sr cell during irradiation by 14-MeV neutrons. However, to use 14-MeV neutrons effectively, we need to remove ^{89}Y. Figure 6a shows the amounts of ^{90}Sr, ^{89}Sr, and ^{89}Y as a function of irradiation time, where yttrium is not separated from strontium. The amount of ^{90}Sr at t=0 was normalized as 100. In contrast, Fig. 6b shows these amounts in the case where yttrium is separated from strontium every 30 days. By separating these elements, >90% of the ^{90}Sr could be maintained in the ^{90}Sr cell.

Technetium-99 is mainly transmuted by the (n, γ) reaction to ^{100}Tc, which decays to ^{100}Ru (stable nuclei) with a half-life of 16 s. To maintain the percentage of ^{99}Tc in the technetium cell at > 90%, ruthenium must be separated out every 90 days.

Table. 3 shows the amount of each nuclide transmuted per year in this system. This system, using a 100-MW (electric) driver, supports the yearly discharge from approximately one 3000-MW (thermal) light water reactor. The fission reaction rate changes as a function of time because the (n, γ) reaction and β^- decay cause the percentage of each TRU nuclei to change. Therefore, the incineration half-life of each nuclide also changes with time. To quantitate the time dependence of the incineration half-lives, the time-dependent TRU component should be included in the calculation of neutron transport.

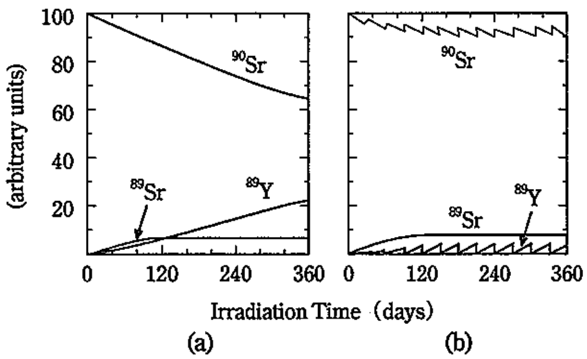

Fig. 6 The time depenence of the amounts of ^{90}Sr, ^{89}Sr, and ^{89}Y (a) in the case in which yttrium is not separated from strontium and (b) in the case in which yttrium is separated from strontium every 30 days. The amount of ^{90}Sr at t=0 was normalized as 100.

Table. 3 Reduction by Incineration per Year for Each Fission Product and TRU

Waste	Reduction by Incineration (kg/yr)^{a}
^{237}Np	29.0
^{241}Am	43.1
^{243}Am	6.8
^{244}Cm	1.5
^{238}Pu	2.0
^{239}Pu	90.4
^{240}Pu	23.3
^{241}Pu	14.5
^{242}Pu	3.2
TRU (sum)	244.5
^{90}Sr	39.6
^{99}Tc	95.8

[3] To calculate this quantity for elements of TRU, we used the incineration half-life including only the cont-ribution of the fission reaction.

In the core shown in Fig. 2, the number of fission reactions is 1.08 per 14-MeV neutron, which corresponds to a thermal energy of 210 MeV. This energy can be converted into 70 MeV of electrical energy when the efficiency of the thermal-to-electric conversion is 1/3. Because the electrical energy required to generate one 14-MeV neutron is 64 MeV, this system is energetically complete and closed within itself.

Even if the driver efficiency or μCF repetition number is not as high as was assumed in Sec. 2, we can maintain the condition of energy closeness by increasing the amount of TRU, which increases the number of fission reactions. However, there are two disadvantages when the amount of TRU increases : The incineration half-life for TRU becomes longer, and the multiplication factor of the core becomes larger.

We calculated the multiplication factor k_{eff} of the core by MCNP, using fission neutrons as the initial input of neutrons instead of 14-MeV neutrons. Fig. 7 shows k_{eff} as a function of the TRU inventory. In the calculation, the diameter of the TRU cell is of the same value as the length of the TRU cell in the z direction. As the volume of the TRU cell was changed, the volumes of the outer cells also changed because the thickness of the outer cell was fixed. A core with dimensions as shown in Fig. 2 has a k_{eff} of 0.68, which is much smaller than the critical k_{eff} of 1.0. The inventory of TRU should not be larger than 1800kg because k_{eff} then becomes 1.0. When the fraction of plutonium in the TRU is decreased, the k_{eff} value decreases ; a greater TRU inventory will be allowed.

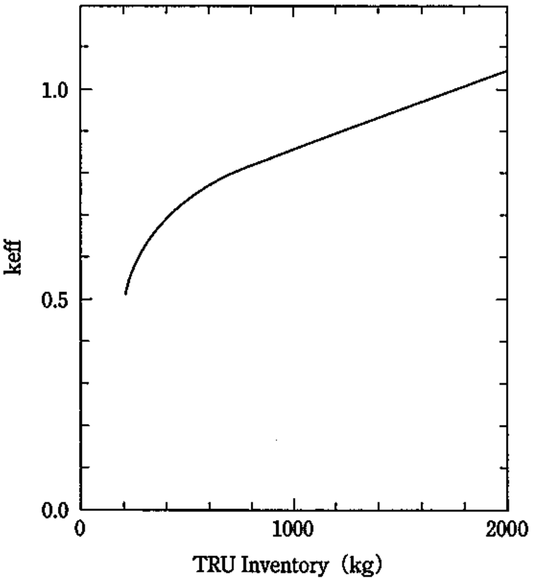

Fig. 7 The keff of the core as a function of the TRU inventory.

The inventory of ^{6}Li was divided between two cells. The inner ^{6}Li cell surrounding the TRU cell mainly prevents thermalized neutrons from penetrating into the TRU cell. The outer ^{6}Li cell mainly produces tritium that is used as fuel for the D-T fusion reaction. The ^{6}Li-Al alloy was used as the material to contain ^{6}Li, in this way achieving a high density of ^{6}Li (Ref. 11) ; this allows for a compact core design. For the core design shown in Fig. 2, the probability of tritium production was 0.98 per 14-MeV neutron ; therefore, almost all the tritium consumed by the μCF reaction can be supplied within the system.

Heat production was calculated in the ^{90}Sr and TRU cells, where high heating density is expected. The average heat density in the ^{90}Sr cell was only 0.23 kW/cm^3, mainly produced by β and γ heating. The average heat density in the TRU cell was 2.6 kW/cm^3, mainly produced by fission reactions. This heat density is less than the 5 to 10 kW/cm^3 allowed by direct cooling of BISO/TRISO type fuel particles by radial flow of pressurized helium gas through the fuel bed.[14]

4. SUMMARY

We studied the feasibility of using an incineration system in which 14-MeV neutrons produced by the μCF reaction are used to trigger incineration reactions ; a subcritical core, composed of fission products and TRU, is used as a target. For our calculations, ^{90}Sr and ^{99}Tc were chosen as representative fission products. In the system, a 14-MeV neutron transmutes ^{90}Sr by the (n, 2n) reaction ; transmutation of ^{90}Sr would be difficult if the (n, γ) reaction were used because the cross section of ^{90}Sr(n, γ) is very small. Outcoming neutrons transmute TRU by a fission reaction. Further-more, fission neutrons are used to generate tritium and to incinerate ^{99}Tc : Tritium is used as a fuel for the μCF reaction and ^{99}Tc is a representaive fission product whose (n, γ) cross section is >1 b.

The MCNP calculation shows that this system will efficiently incinerate both fission products and TRU. When a 4 GeV-25 mA deuteron accelerator is used to produce μ^- mesons, the incineration half-lives of ^{90}Sr, ^{99}Tc, and TRU are 1.6, 1.6, and 0.6 yr, respectively. The incineration amounts of these nuclei are 40, 96, and 245 kg/yr, respectively.

All electric energy needed to generate μ^- mesons can be supplied from fission energy. Therefore, this system dose not require any energy from outside. This system can also produce enough tritium to be consumed by the μCF reaction. The multiplication coefficient of the subcritical core is 0.68 ; the system is much safer than an incineration system with only a fission reactor that is operated under critical conditions.

The time dependence of the core components should be included in future studies to obtain a more accurate evaluation of the proposed system.

5. ACKNOWLEDGMENTS

We wish to thank A. D. Woodhead for her editorial work. This work was supported by the Power Reactor and Nuclear Fuel Development Corporation in Japan and the U. S. Department of Energy at Brookhaven National Laboratory, under contract DE-AC02-76CH00016.

6. REFERENCES

(※) H. HARADA, H. TAKAHASHI, A. L. ARONSON, T. KASE, K. KONASHI, and N. SASAO, Fusion Technology, 24, 161(1993).

(1) M. TAUBE, "The Transmutation of Strontium-90 and Cesium-137 in a High-Flux Test Reactor with a Thermalized Central Regoin, " Nucl. Sci. Eng., 61, 212 (1976).

(2) P. DE FELINE, R. OCONE, and A. RANDI, "High Energy Proton Interaction with Sr and Cs : A Contribution to the Waste Transmutation Study," Nucl. Instrum. Methods, 212, 359 (1983).

(3) A. D. ARTHUR, "A New Concept for Accelerator-Driven Transmutation of Nuclear Waste, " Fusion Technol., 20, 641 (1991).

(4) H. HARADA, T. SEKINE, Y. HATSUKAWA, N. SHIGETA, K. KOBAYASHI, T. OHTUKI, and T. KATOH, "Measurement of the Themal Neutron Cross Section of the ^{90}Sr(n, γ) ^{91}Sr Reaction," J. Nucl. Sci. Technol., 31, 173 (1994).

(5) H. HARADA, H. WATANABE, T. SEKINE, Y. HATSUKAWA, K. KABAYASHI, and T. KATOH, "Measure-ment of Thermal Neutron Cross Section of ^{137}Cs (n, γ) ^{138}Cs Reaction," J. Nucl. Sci. Technol., 27, 577 (1990).

(6) H. TAKAHASHI, "The Role of Accelerators in the Nuclear Fuel Cycle," Proc. 2nd Int. Symp. Advanced Nuclear Energy Research, Mito, Japan, January 24-26, 1990, p. 77 (1990).

(7) Y. GONO, Unpublished (1989).

(8) T. KASE, K. KONASHI, N. SASAO, H. TAKAHASHI, and Y. HIRAO, "Transmutation of ^{137}Cs Using Muon-Catalyzed Fusion," Muon Cat. Fusion Reaction, 5/6, 521 (1990/1991).

(9) Yu. PETROV, Private Communication (1991).

(10) J. F. BRIESMEISTER, "MCNP : A General Purpose Monte Carlo Code for Neutron and Photon Transport," Version 3A, LA-7369-M, Los Alamos National Laboratory (1986).

(11) J. POWELL et al., Private Communication (1991).

(12) H. TAKAHASHI, "Muon Catalyzed Fusion in Plasma State and the High Intensity dt Fusion Neutron Source," Proc. 5th Int. Conf. Emerging Nuclear Energy Systems, Karlsruhe, Germany, July 3-6, 1989, p. 261.

(13) H. TAKAHASHI, "OMIC Energy Industry Radioactive Wastes Handling Problems," p. 26, Moscow Radio Technical Institute of the USSR Academy of Sciences (1991).

(14) M. TODOSOW, H. LUDWIG, H. TAKAHASHI, and J. POWELL, "High Flux Particle Bed Reactor

Systems for Rapid Transmutation of Actinides and Long-Lived Fission Products," Fusion Technol., 20, 678(1991).

(15) P. F. ROSE, Ed., "ENDF/B-VI Summary Documentation," BNL-NCS-17541, Brookhaven National Laboratory (1991).

(16) J. KASAGI, Private Communication (1989).

12.　光溶液化学…光照射原子価調整によるTRU元素の分離(※)

和田幸男，森本恭一，五位渕孝幸，富安　博*
先端技術開発室　Innovation Technology Development Section
*東京工業大学、原子炉工学研究所　Tokyo Institute of Techology, Research Laboratory for Nuclear Reactors

Photo-Solution Chemistry……Separation of TRU Elements by Adjusting Valencies with Photon Irradiation

Y.Wada, K.Morimoto, T.Goibuchi, H.Tomiyasu*

A photochemical method of removing Np from mixture nitric acid solutions of Pu and Np has been studied in connection with the Purex reprocessing. Their valencies and concentrations of Pu and Np at initial sample conditions were adjusted to Pu（Ⅲ）, Np（Ⅴ）and to 1×10^{-4}, 1×10^{-3} M(M=mol·dm^{-3}), respectively. Experiments were carried out under various conditions of which parameters were irradiation rates of Hg lamp and concentrations of HNO_3. When the irradiation rate was 0.015W and the acidity was 3N HNO_3, Pu(Ⅲ) was rapidly oxidized to Pu(Ⅳ) and more than 95% of it remained in the same valency even after the continuous further irradiation. On the other hand, Np(Ⅴ) did not change. From these results, the mechanism for the photochemical reactions of Pu and Np was discussed with the standpoint of thermodynamical considerations.

1.　緒　言

現在の再処理工程技術は、ピューレックス法を採用しており、目的元素（PU, U）をTBP/n－ドデカン溶媒に抽出されやすい原子価または水溶液中に留まりやすい原子価に化学試薬を用いて調整し、分離、精製している。しかし一方では、使用する化学試薬による工程廃液の低減化および長寿命核種（TRU, I, Tc等）の回収および共抽出のための選択的原子価制御及び工程の簡素化等の改良再処理技術が近年求められている。

これらの課題を解決する一つの方法として、光溶液化学法が1970年代から主に米国で検討されてきた(1)~(6)。そこで本研究では、TRU核種の光酸化還元（redox）反応挙動とその反応メカニズムの解析及び再処理工程への適用性評価を行った。

2.　原　理

光照射による目的元素の酸化還元反応は、以下に示す反応

① 光分解生成物（NO_2^-, HNO_2等）
② 光励起溶媒イオン分子種（$^*NO_3^-$等）
③ 目的元素の光励起イオン種
（*Pu (Ⅲ,Ⅳ,Ⅵ), *U (Ⅳ,Ⅵ), *Np (Ⅲ,Ⅳ,Ⅵ)）

と

目的元素又は他の共存する、酸化体及び還元体との反応が考えられる。従来の光溶液化学研究では、①の亜硝酸と目的元素の反応及び光照射下のアルコール等の共存系での生成U(Ⅳ)によるPu(Ⅳ)→Pu (Ⅲ)の還元など、間接的な目的元素の酸化還元反応が主な研究項目であった(6)。

一方、我々の研究では①の他に②と③の反応も大きく光酸化還元反応に関与しているものと考え、そのメカニズムを考察した。それは、溶液中での光励起イオン種のもつ化学反応性が増し、酸化還元反応をより容易に起こすものとの考え方による。

3.　実　験

実験は、試験溶液を再処理工程条件に模擬して、分配工程のPu逆抽出工程溶液中の原子価状態、Pu (Ⅲ), Np (Ⅴ)にあらかじめ、HAN（ヒドロキシルアミン）およびヒドラジンを用いて調整した。この試験溶液の2mlに水銀ランプ光の全波長光を一定時間照射した。この試料のPuとNpの原子価変化を抽出クロマトグラフィー(7)－α放射能分析法により定量した。この分析概念を図1に示す。実験のパラメータとしては、硝酸濃度、0.17N, 1N, 3N, と光照射強度（ワット, W）, 0.015W, 0.5W,をとり、各パラメータ水準におけるPuとNpの光酸化還元反応挙動を調べた。

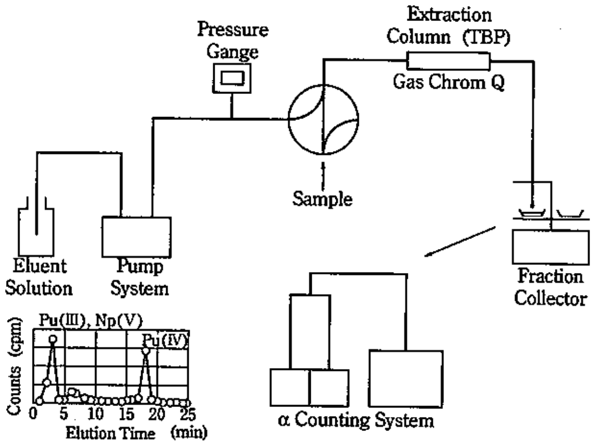

図１　抽出クロマトグラフ－α放射能分析システム

4. 実験結果

図2, 3及び4は、光照射強度が0.015ワット(W)で試料酸濃度をパラメータにしたときのPuの光酸化還元反応挙動結果を示す。光照射強度が一定のとき、硝酸濃度の上昇により、Pu (Ⅲ)→Pu(Ⅳ)の酸化反応速度が急速に増加することがわかる。

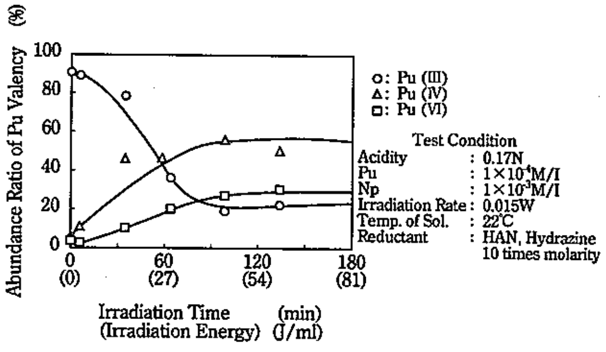

図２　光照射によるPuの酸化還元反応

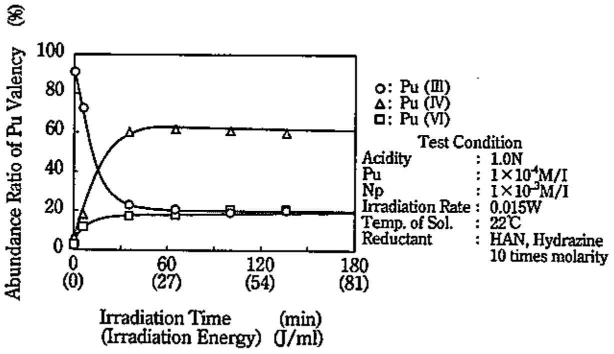

図３　光照射によるPuの酸化還元反応

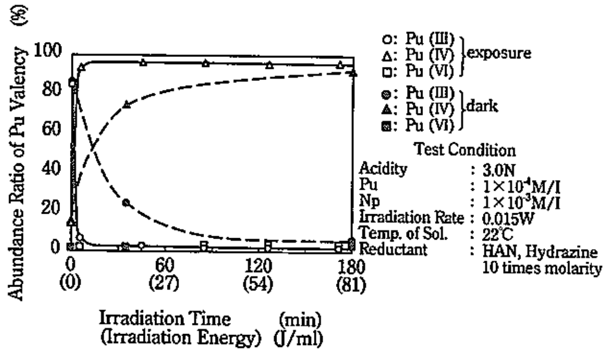

図４　光照射によるPuの酸化還元反応

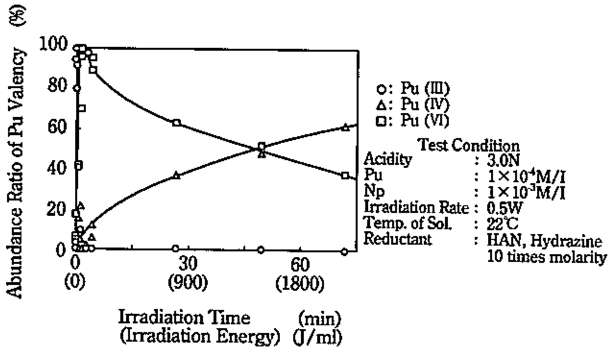

図５　光照射によるPuの酸化還元反応

図5は、図4と同じ3N硝酸溶液で、光照射強度が約30倍、0.5Wのとき結果を示す。光照射強度の増加により、Pu (Ⅲ)→Pu(Ⅳ)→Pu (Ⅵ)の酸化反応がより速く進ことを示している。特に、図4に示す照射条件は、ほぼ完全に相互分離に必要な条件、Pu(Ⅳ)とNp(Ⅴ)に調整できたこと示している。

5. 考　察

今までに、無機酸溶液中に溶解している元素の光溶液化学反応メカニズムを考察した例は少ない。そこで我々は、硝酸濃度及び光照射強度の変化により、なぜ前述したような結果が得られたか、その光酸化還元反応メカニズムを検討した。この基本となる考え方は、光吸収励起エネルギーの化学反応性への寄与として、標準酸化還元電極電位の変化を考えた。

すなわち、光吸収励起分子種は、その励起エネルギー分だけその電位が変化し、分子種の持つ酸化力又は還元力が増大する⑻。この考え方の概念を図6に示す。これらの光励起分子種は、基底状態の同一の分子種とは、全く異なる酸化還元電位を持つことなり、あたかも全く別の、非常に強い酸化体又は還元体のように作用することとなる。そのため、光を吸収する分子種の濃度及び吸収する光の照射強度が、直接全体の反応速度に影響を及ぼすことになる。

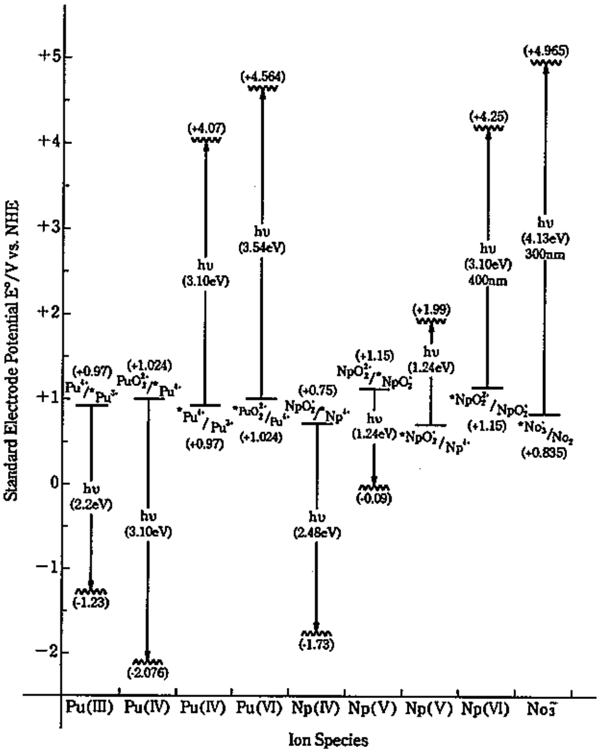

図６　光励起による標準酸化還元電極電位の変化

特に本研究においては、溶液中の硝酸濃度が液中の溶質に比べ10－100倍大きいため、硝酸の光吸収励起分子種、$^*NO_3^-$の強力な酸化体としての影響が大きかったものと思われる。このような考えかたに基ずいて、HANとヒドラジンの還元剤を含むPu(Ⅲ)硝酸溶液中における、光酸化還元機構図を図7に示す。この反応機構図中の主要な酸化還元反応式から、各原子価への反応速度式を求め、図に表すと図8のようになる。

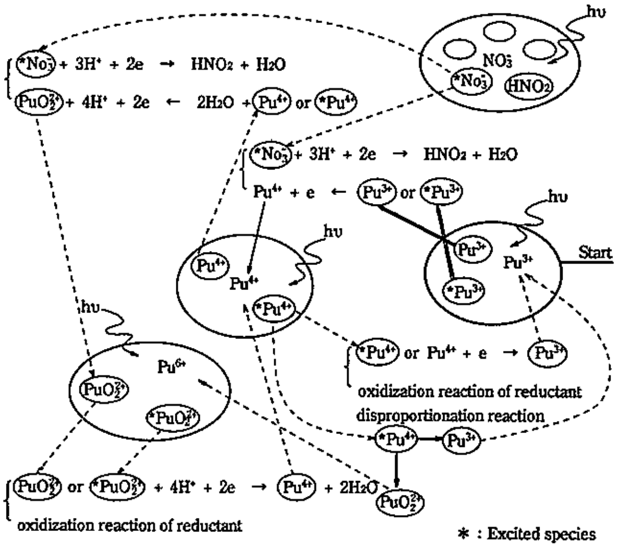

図７　光照射によるPuの酸化還元反応機構

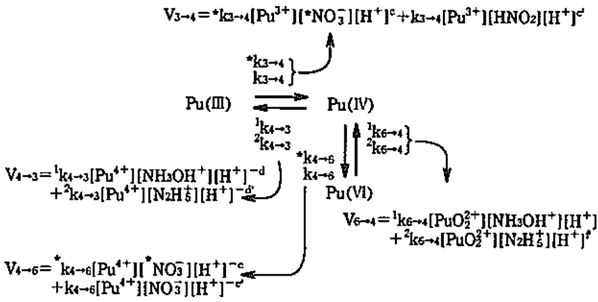

図８　硝酸溶液中のPuの光酸化還元反応速度式

これらの光反応速度式から、光酸化還元実験結果の反応メカニズムを説明することができる。すなわち、反応速度式から判断されるように、Pu(Ⅲ)→Pu(Ⅳ)の酸化反応は、光励起イオン種濃度、$[{}^*NO_3^-]$と水素イオン濃度、$[H^+]^c$に比例し、逆反応は$[H^+]^d$に反比例することがわかる。またPu(Ⅳ)→Pu(Ⅵ)への酸化反応は、$[{}^*NO_3^-]$に比例し、$[H^+]^e$には反比例して、逆反応は$[H^+]^f$に比例する。このようなことから、図3, 4中の結果では、反応の平衡状態でPu(Ⅲ)とPu(Ⅵ)存在していたが、図5で示すように3N HNO_3溶液での結果では、両原子価がほとんど平衡状態において存在しなかったことが説明できる。

6.　応用検討

現在のピューレックス法による再処理工程中のU, Pu及びNpの各原子価は、図9に示されるような状態で分配されていると解析される。この中でU, Pu分配工程のPuプロダクト工程液ではPu(Ⅲ)とNp(Ⅴ)に調整されている。

本実験研究では、この工程条件からの光酸化還元反応試験を実施し、PuとNpの溶媒抽出分離条件に必要な、Pu(Ⅳ)への再酸化及びNp(Ⅴ)の保持が可能であることが判明した。また水銀ランプ光でのPu(Ⅲ)→Pu(Ⅳ)への光酸化の量子収率は、約20％であることが実験結果から得られた。そこでこのような結果から、工程技術への適用を検討し、以前に報告されているような実験レベルの装置(6)とは異なり、実用化のための図10のような光照射装置を考えた。この装置は、液容量が約3Lのドーナツ状照射セルで5本の水銀ランプを図のように配し、照射効率を高めるために、内壁を鏡で囲ったものである。

この装置を一ユニットとし、図11のように再処理分配工程内で配置した場合、一時間内に光照射、約5分、および液移送を3回繰り返すことにより、現工程能力の約110L/hrの再酸化処理能力が可能であると解析された。このことから、現工程技術の亜硝酸ガスによる再酸化技術と比較すると、次のような利点が考えられる。

- 亜硝酸ソーダのような試薬を使用しない、光照射のみでのPu(Ⅲ)→Pu(Ⅳ)の再酸化ができる。
- 現工程技術ではできなかった、PuとNpの相互分離ができる。

- 亜硝酸ガス発生工程およびその追い出し工程等が不要となり、工程が縮小できる。
- 溶媒劣化の主要原因であった亜硝酸ガスを使用しない工程技術。
- 再酸化試薬を使用しないため、工程廃液が低減化される。

以上のような大きな利点があるが、工程技術化には今後更に詳細な検討が必要である。

7. 今後の研究

今後は現在おこなっているPu, UおよびNpの光反応挙動を更に熱力学的に検討すると共に、TRU元素の共抽出または相互分離に必要な選択的な光原子制御技術を研究する。そのためには、Np(V), Am(Ⅲ)及びCm(Ⅲ)等の光酸化の可能性を検討すると共に、これらの元素の高原子価状態の溶媒抽出特性を調べる必要がある。これらの研究成果は、現状では困難なTRUの共抽出、相互分離技術の確立に反映される。

8. 参考文献

(※) 和田幸男，森本恭一，他“硝酸溶液中のプルトニウムとネプツニウムの光化学的原子価調整に関する基礎研究”動燃技報No.88(1993).

(1) Gangwer,T.: BNL 50715(1977).

(2) Golgstein,M., Baker, .J.J., Gangwer,T. : Nuclear Engineering International, 22, 69－73(1977).

(3) Bell,J.T., Toth,L.M. : Radiochimica Acta, 225－230(1978).

(4) Dopoorter,G.L., Rofer－depoorter, C.K. : Actinide Separations, 267－276(1980).

(5) Ohno,S., Kobayashi,Y., Kimura,T. : J. of the atomic Energy Society of Japan, 28,933－937(1986).

(6) Enokida,Y., Suzuki,A. : NEUT Research Report 87－04(1987).

(7) Enokida,Y., Suzuki,A. : J. Nucl. Sci. Technol., 24, 859(1987).

(8) Boch,C.R., Whitten,D.G., Meyer,T.J. : J. Am. Che. Soc., 97, 2909(1975).

編集後記

核燃料技術開発部皆様の御協力を頂き、第３号を発刊することができました。編集委員一同厚く御礼申し上げます。また、編集に際しまして、不手際が多々ありましたこと、この場をお借りしてお詫び申し上げます。

今後とも、本誌の発展に御協力賜りますよう、お願い申し上げます。

編集委員一同

編集委員